Analysis of the Hole Shape Evolution
in Ultrashort Pulse Laser Drilling

von Dipl.–Phys. Sven Döring
geboren am 21. Januar 1983 in Zeitz

Contents

Introduction

The laser as a contact-free machining tool is continuously driving innovation to more efficient processes and new manufacturing possibilities in today's industrial production [1–3]. The growing demand of micron-sized features for the accelerating miniaturization in the sectors of electronics, optics, medical and automotive applications requires new machining processes. Ultrashort laser pulses with a pulse duration of typically less than 10 ps gained special interest as the short timescales of laser-matter interaction combined with extreme peak intensities enable new mechanisms for material modification and removal. Machining processes with ultrashort pulses are capable of generating micro structures with high quality and challenging precision in a large variety of materials [4–7]. Examples for up-to-date applications are cutting of ultrathin, hardened display glass [8] and the fabrication of drainage channels for diesel injector systems [9]. Furthermore, the manufacturing of cardiovascular stents [8] as well as selective thin film processing, e.g. electrode patterning in solar cell and display production [10, 11], is realized with ultrashort laser pulses. A further development of the processing capabilities, in particular three-dimensional structuring, is of highest relevance for future applications, especially with respect to the material classes of metals and semiconductors.

The ultrashort pulse material interaction has been subject to detailed experimental and theoretical investigations [1, 4, 12–18]. The physical mechanisms of absorption, energy redistribution, material decomposition and removal and their respective timescales are relatively well understood for ablation induced by a single pulse at a planar surface. In contrast, the laser ablation of structures with high aspect-ratio ($\geq 5:1$) at a micron size level (typically $< 100\,\mu m$ in diameter) is still a demanding task, in particular drilling of microholes. The ablation process at the hole bottom is influenced by the previously excavated hole capillary. This leads to a reduction of the drilling rate with increasing depth [19–22]. In addition, the shape formation of the hole is affected. Fig. 1 shows an example of an ultrashort pulse-drilled hole in Invar alloy with picosecond pulses.
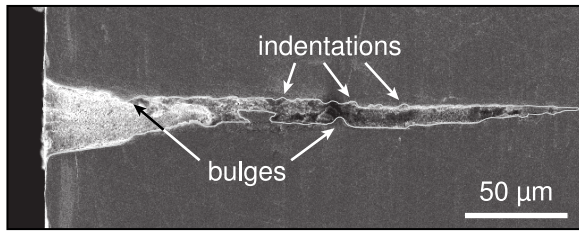
Fig. 1: Cross-section through a laser percussion-drilled microhole in Invar alloy after 50,000 laser pulses. Drilling was performed with ultrashort pulses of 8 ps duration (FWHM) at a wavelength of 1030 nm and a fluence of 10 J/cm^2.

In this cross-section, bulges and indentations cover the hole walls. Also, the hole is not straight but has a bending in the middle. The actual sizes and positions of the bulges, indentations and bendings are not reproducible even under identical drilling conditions. In some cases, the formation of multiple capillaries with different orientations can be observed in the lower part of the hole [23–25]. Although the hole entrance has a circular shape, a cross-section of the hole at a larger depth can have a nearly arbitrary shape [26, 27]. These hole shape features are typical for the laser drilling process and can be observed in different kinds of materials and under different processing conditions [21, 24, 28–30]. All in all, the benefits of ultrashort pulse ablation at the surface do not directly translate to deep microdrilling with high aspect-ratio. Therefore, profound investigations of the hole shape evolution and the mechanisms involved in the hole formation are essential for a fundamental understanding of the drilling process.

A detailed investigation of the drilling process in opaque materials, especially metals, is challenging, though. Cross-sections, as for example in fig. 1, only show the shape of a finished hole after a certain number of applied pulses. The formation of indentations, bulges and hole bendings, however, is subject to statistical variations. Hence, the specific hole shape evolution cannot be retraced by an analysis of many different holes with this technique. Direct observations of the hole formation during the drilling process have been realized with nanosecond pulses in ceramics [19, 24] and with femtosecond and sub-nanosecond pulses in diamond and polymers [21, 31]. Although these investigations currently provide the most comprehensive insights in the hole shape evolution, the involved interaction and ablation mechanisms as well as material properties differ significantly from the regime of ultrashort pulse laser drilling in metals and opaque materials. In recent years, new techniques for real-time depth monitoring in opaque materials have been developed [32, 33]. This shows the importance of detailed process investigations for the further enhancement of micro structuring with high aspect-ratio.

Several differing explanations for the peculiar evolution of the shape have been developed. This includes material inhomogeneities [21], the abrasive effect of the laser-generated plasma [19, 24], nonlinear interaction of the laser pulse with the ambient atmosphere [34–36], beam deflection by laser-induced plasma [25, 37], deposition of ablation particles inside the hole channel [26], polarization dependent reflection at the hole walls [21, 27, 38] and the influence of the hole geometry on the pulse propagation to the hole bottom [22, 39, 40]. However, the specific contribution of these possible influences on the hole shape formation are not fully understood yet.

Hence, a new approach for the analysis of the drilling process is required. In this work, an in-situ observation of drilling in an opaque material is realized for the first time. The principle is based on the use of crystalline silicon as the sample material. It is transparent for laser wavelengths above the band edge at ca. 1100 nm [41] and opaque for lower wavelengths, including the typical ultrashort pulse laser systems for material processing, i.e. wavelengths of 1030 nm, 800 nm and 515 nm. Furthermore, the ablation behavior of silicon is similar to a metal at these wavelengths in the ultrashort pulse regime [15, 42, 43] and drillings with high aspect-ratio are possible [22]. It is therefore used here as a model system for drilling of semiconductors as well as the industrially relevant material class of metals. During drilling, the sample is illuminated by a second laser with a wavelength of 1060 nm. At this wavelength, silicon is nearly transparent but a standard silicon-based camera sensor can still produce a high-contrast image of the hole silhouette.

This study concentrates on the technique of percussion drilling, where the position of the laser focus stays constant during the complete drilling procedure, usually at the sample surface [44]. In this case, the diameter of the resulting hole is similar to the size of the focal spot. Therefore, the most distinct influence of the hole capillary on the further hole formation and depth evolution can be expected.

The present work pursues a systematic investigation of the effect of the laser and process parameters on the hole shape evolution including the pulse energy, fluence, pulse duration, wavelength and focus position. Moreover, the role of particle debris inside the hole channel, the interaction of subsequent laser pulses with previously ablated material inside the hole, the expansion of the plasma plume and the light propagation inside the hole capillary are studied as possible reasons for the special hole shape formation.

Structure of this Thesis

This thesis is organized in five chapters.

Chapter 1 gives a short review of the fundamental physical processes of laser ablation with short and ultrashort laser pulses.

Chapter 2 then summarizes the state-of-the-art experimental techniques for the investigation of laser deep drilling and their specific advantages and limitations. This is followed by a review of the current state of knowledge on the laser drilling process.

Chapter 3 presents the experimental realization of the in-situ drilling observation with silicon as the sample material. This technique is then used in different configurations to investigate the influence of laser and processing conditions on the hole shape evolution.

Chapter 4 covers the results of hole shape evolution and depth development by in-situ imaging of the percussion drilling process. Different laser parameters, e.g. pulse energy, wavelength, pulse duration, as well as different processing conditions, e.g. applied fluence and focus position, are under investigation. A common, general description of the hole formation process is developed.

Chapter 5 focuses on the physical mechanisms of the hole shape formation, especially the reasons for the formation of special shape features, i.e. bending, bulges and indentations. The effect of the ablation particles, the interaction of consecutive pulses, the expansion of the laser-generated plasma and the pulse propagation through the hole capillary are studied in detail.

Finally, this thesis is completed with a conclusion conveying the essential findings and an outlook of possible methods to enhance the drilling precision and further investigations for an advanced understanding of the hole formation process in ultrashort pulse laser deep drilling.

1 Fundamentals of Short and Ultrashort Pulse Laser Ablation

The laser ablation process is characterized by the physical mechanisms of absorption, energy diffusion, material decomposition and expansion of the material vapor. This chapter gives a short review of the laser-matter interaction by short and ultrashort pulses and the respective timescales of the ablation mechanisms. The following discussion is mostly based on experimental and theoretical studies of the ablation behavior of metals and semiconductors.

1.1 Energy Absorption and Redistribution

The energy of the laser pulse is first absorbed by the electrons [45], e.g. by free-free transition of the electrons in the conduction band of a metal. The heavy ions of the lattice cannot follow the high-frequency oscillation of the incident electromagnetic field. Thermalization within the electron system takes place rapidly, typically on a femtosecond timescale [46], which leads to a thermal energy distribution. Therefore, it is usually assumed that the energy of the electron system can be characterized by a temperature [35, 47]. The energy transfer from the electrons to the lattice is mediated by electron-phonon coupling [48] which typically takes place on a timescale of 1 ps to 100 ps [14, 49, 50]. Consequently, the temperature of the lattice can be different from the electron temperature and needs to be characterized separately [47], especially for pulses with a duration equal to or even shorter than this coupling time. The evolution of the electron temperature T_{el} and the lattice temperature T_{lat} can be described by the

Two-Temperature-Model [47] according to

$$C_{el}\frac{\partial T_{el}}{\partial t} = \nabla \cdot \left(\kappa_{el}\nabla T_{el}\right) - G \cdot \left(T_{el} - T_{lat}\right) + Q,$$
$$C_{lat}\frac{\partial T_{lat}}{\partial t} = \nabla \cdot \left(\kappa_{lat}\nabla T_{lat}\right) + G \cdot \left(T_{el} - T_{lat}\right). \tag{1.1}$$

C_{el} and C_{lat} denote the electron and lattice heat capacities and κ_{el}, κ_{lat} the respective thermal conductivities. G is the electron-phonon coupling coefficient. In general, all these parameters are temperature dependent themselves. The heat source Q can be derived from the absorption of the laser pulse by the Bouguer-Lambert-Beer law [1]. For a laser pulse with intensity I and perpendicular incidence on the surface in z-direction, it is given by [4]

$$Q = \alpha\left(1 - R\right)I \cdot \exp\left[-\alpha z\right] \tag{1.2}$$

in which α is the absorption coefficient and R the surface reflectivity of the material. This means, the pulse energy is initially deposited in a layer with a characteristic thickness of $l_\alpha = \alpha^{-1}$ which is the so-called optical penetration depth. For metals, this is typically a thin surface layer with a few nanometer thickness [1, 51].

For pulses with high peak power, absorption can be induced in otherwise transparent media (e.g. dielectrics) due to the generation of free electrons from multiphoton absorption or field ionization [12, 14]. The trailing part of the pulse is then absorbed by these free electrons similar to the situation in a metal. The further process of energy transfer can be described with the Two-Temperature-Model. In this case, the effect of the changing free electron density on the thermal (C, κ, γ) and optical properties (R, α) has to be considered as well [52, 53].

To illustrate the typical evolution of the electron and lattice temperature, fig. 1.1 shows a numerical solution of the Two-Temperature-Model according to equation 1.1. In this example, a copper sample is irradiated by a pulse with a Gaussian temporal profile and a duration of 1 ps. The absorbed fluence, i.e. the pulse energy per irradiated area, is $F_{abs} = (1 - R) \cdot F = 0.2\,\text{J/cm}^2$. Temperature dependent values of the electron heat capacity and the electron thermal conductivity are considered in the model. A detailed description can be found in appendix A, p. 101. The simplified simulation here does not account for changes of the material phase, i.e. melting and evaporation, and removal of material. Nevertheless, the temperature represents the energy distribution within the system.
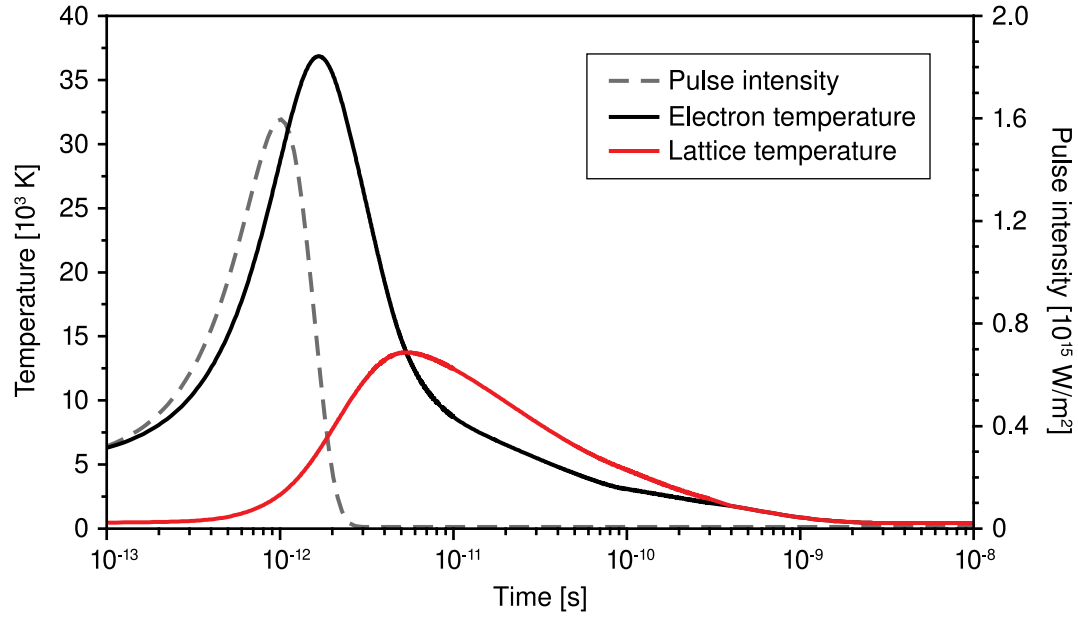
Fig. 1.1: Simulated electron and lattice temperature evolution in copper according to the Two-Temperature-Model. The temporal profile of the pulse intensity is given as a dashed line for reference. The pulse duration is 1 ps and the entire absorbed fluence adds up to $F_{abs} = (1-R) \cdot F = 0.2 \, J/cm^2$.

At the beginning of the laser pulse, the temperate of the electrons rises rapidly with the increasing pulse intensity, i.e. mainly in the first picosecond. The maximum electron temperature reaches several ten thousand Kelvin due to the low electron heat capacity. The energy transfer from the electrons to the lattice is delayed with a characteristic electron-phonon coupling time τ_{el-ph}. This coupling time can be defined from the time constants of electron cooling $\tau_{el} = C_{el}/G$ and lattice heating $\tau_{lat} = C_{lat}/G$ as [1]

$$\tau_{el\text{-}ph} = \left[\frac{1}{\tau_{el}} + \frac{1}{\tau_{lat}} \right]^{-1} = \frac{C_{el} \cdot C_{lat}}{G \cdot (C_{el} + C_{lat})}. \tag{1.3}$$

In the example in fig. 1.1, τ_{el-ph} is longer than the pulse duration and the maximum lattice temperature is reached only after several picoseconds, i.e. significantly after the end of the laser pulse. Typical values of the electron-phonon coupling coefficient, heat capacities and the resulting coupling time τ_{el-ph} for different metals are summarized in tab. 1.1. For metals, the characteristic coupling time τ_{el-ph} is generally in the order of several picoseconds. If the pulse duration is shorter than the electron-phonon coupling time, heating of the lattice as well as heat diffusion occurs after the irradiation and

Tab. 1.1: Electron-phonon coupling time for aluminum, copper, iron and gold at an assumed electron temperature of 10,000 K [54].

		Al	Cu	Fe	Au
G	$\left[10^{17}\,\text{W/m}^3\text{K}\right]$	5.7	1.0	2.4	0.2
C_{lat}	$\left[10^6\,\text{J/m}^3\text{K}\right]$	2.4	3.5	3.5	2.5
C_{el}	$\left[10^6\,\text{J/m}^3\text{K}\right]$	1.4	1.0	5.0	0.7
$\tau_{\text{el-ph}}$	$\left[\text{ps}\right]$	1.5	7.6	8.6	26.3

is therefore mainly determined by the material properties. Such a pulse duration is referred to as ultrashort, which typically means 10 ps or less. In this case, heat diffusion is limited to the lowest possible amount for the specific material and the energy stays confined within the irradiated area [15]. Equalization of electron and lattice temperature then occurs after several cycles of $\tau_{\text{el-ph}}$. Afterwards the electron and lattice subsystems can be described by one common temperature, see e.g. the time domain after 300 ps in fig. 1.1. The ablation depth can be calculated from the Two-Temperature-Model simulation either by considering phase transitions in the model or by comparison of the energy content within the electron and lattice systems to the necessary enthalpy for melting and evaporation. In the ultrashort pulse regime, the amount of removed material is in general independent of the actual pulse duration and primarily determined by the applied fluence [55].

For pulses with a duration longer than $\tau_{\text{el-ph}}$, especially longer than several hundred picoseconds, heating of the electron subsystem is comparably slow and the energy transfer to the lattice occurs almost instantaneously. Consequently, the complete energy distribution can be described by a One-Temperature-Model [4]. In this case, significant thermal diffusion already occurs during irradiation, especially for materials with high thermal conductivity like metals. The incident energy spreads into the surrounding material with a characteristic thermal diffusion length $l_{\text{th}} \approx \sqrt{\frac{\kappa}{C} \cdot \tau_{\text{pulse}}}$, which depends on the thermal conductivity κ and the heat capacity C. It increases with the pulse duration τ_{pulse} and can reach 1 µm to 10 µm for a 100 ns-pulse [17]. Therefore, the heat affected zone is larger than the irradiated area for long laser pulses and the ablation threshold as well as the ablation depth strongly depend on the actual pulse duration [4, 56].

In general, the Two-Temperature-Model has been successfully employed for the theoretical discussion and numerical calculation of the ablation threshold, the ablation depth, the melt layer thickness and the heat affected zone [2, 4, 35, 50, 52, 55, 57–62].

1.2 Material Removal Processes

For ultrashort laser pulses, the process of material removal takes place in two stages. In a first step, the high temperatures of the electrons and the lattice cause the thermionic emission of electrons in combination with sublimation and direct transition of the solid to the plasma state [17, 47, 63–65]. The ablation products are therefore electrons, ions and atoms or molecules, which are emitted from the surface on a nanosecond timescale or faster [13, 15, 66].

In a second step, the rapid isochore heating of the lattice results in a superheated layer which is subject to high thermoelastic pressure [1, 67, 68]. The relaxation of this stress leads to the amorphization of the surface layer and desorption from the surface. Simultaneously, nucleation of bubbles and larger voids takes place below the surface. The coalescence of these voids creates a foam-like structure with the amorphous layer on top, which separates from the solid [18, 67, 69–72]. This way of fracturing of the solid, also referred to as spallation, causes ablation in the form of clustered atoms as well as nanoparticles [73–77]. For higher absorbed energy densities, the spallation process turns into rapid melting and direct heating of the solid above a critical temperature for phase separation which is approximately 6000 K for metals like iron, aluminum and copper [1, 18, 65]. A decrease in pressure due to expansion initiates massive homogeneous nucleation followed by a breakdown of the liquid into a liquid-gas mixture with explosive expansion [70, 78]. This so-called phase explosion generates vapor and plasma as well as liquid droplets [40, 63]. This second step of ablation occurs after a delay of several tens of nanoseconds [65]. The fraction of material that is removed by spallation and phase explosion in comparison to the direct transition to plasma in the first step depends on the total absorbed fluence and pulse duration. It is lowest for a fluence close to the ablation threshold, whereas ablation at a high fluence occurs mainly via phase explosion [17, 65]. The material removal processes of ultrashort pulses are independent from the exact interatomic potential [71, 79–81] and therefore similar for different material classes, e.g. metals, semiconductors or dielectrics.

A part of the absorbed pulse energy does not contribute to ablation [35]. Hence, the solid surrounding the ablation region is heated and even melted without ablation. Nevertheless, for ultrashort pulses, the thickness of the melt layer is typically below 1 μm [35]. Its maximum thickness is reached after a few tens of nanoseconds and complete resolidification ends after several tens to hundreds of nanoseconds. The timescales of these thermal processes are determined mainly by the material properties in case of ultrashort pulses, when energy deposition is faster than the material response.

For long pulses with nanosecond duration or longer, the material reaches the critical temperature for phase explosion only at high incident energy densities [82, 83]. Otherwise, especially for pulses in the microsecond and millisecond regime, "normal" boiling with heterogeneous nucleation leads to gradual evaporation [1]. This process is accompanied by significant thermal diffusion and pronounced generation of melt, see also the thermal penetration depth l_{th} for long pulses as discussed above. The characteristic times for vaporization and resolidification increase with the pulse duration in combination with a significant increase of the melt layer thickness which can considerably exceed 1 μm [35]. In addition, the recoil pressure from the material vapor leads to the expulsion of melt at the rim of the ablation crater [2]. Melt deposition around and inside the ablation area distort the geometry and also create burr. For ultrashort laser pulses, low melt layer thickness and fast solidification substantially reduce the formation of burr [5].

1.3 Material Vapor and Plasma

The decomposition of the material during the ablation process generates a spherical shock wave in the atmosphere surrounding the laser spot [1, 2]. This shock wave is similar for short and ultrashort laser pulses. The material vapor cloud expands behind the shock wave. For pulses in the picosecond regime and longer, a symmetric shape of the vapor plume can be observed while sub-picosecond pulses create a turbulent vapor flow [84]. For a time span of several tens of microseconds, the vapor expands gradually and separates from the surface. Afterwards, typically on a timescale of 100 μs, a breakup of the plume is observed in combination with the formation of complex flow patterns including swirls [15, 84]. These patterns show large statistical variations, even if ablation is repeated under identical irradiation conditions.

In case of pulses with nanosecond duration or longer, plasma is already generated by the ablation process while the irradiation still continues. Therefore, screening of the laser pulse by the plasma reduces the pulse energy incident on the surface, also referred to as plasma shielding [1]. The energy of the plasma may still be transferred to the substrate and lead to target heating and potentially ablation, but the plasma expansion will affect the size and geometry of the energy deposition on the target surface [1, 85].

A significantly reduced transmission through the ablation plume can also be observed for ultrashort pulses. Here, it occurs on a timescale of several tens to hundreds of nanoseconds [65]. This effect is mainly caused by scattering due the particles emitted by spallation or phase explosion. Although, due to the delay to the incident pulse, there is no influence on the current ablation process, subsequent pulses may be affected by this particle shielding.

1.4 Summary Description of the Ablation Process

The relevant processes for ablation by an ultrashort pulse and their respective timescales are summarized in fig. 1.2 including absorption, energy redistribution, material removal and expansion of the ablation plume.
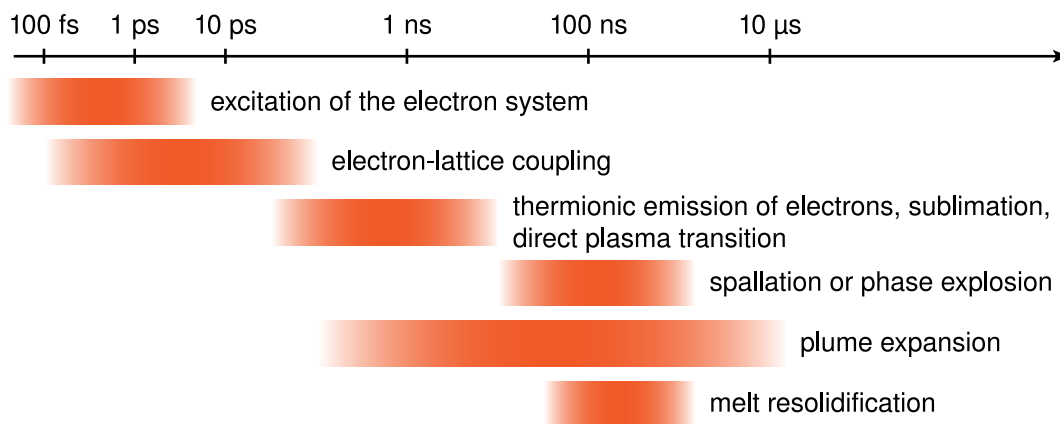

Fig. 1.2: Timescales of the ablation mechanisms for ultrashort pulse irradiation of a metallic target.

For an ultrashort pulse, the excitation of the electrons by the laser pulse is faster than the energy transfer to the lattice which is characterized by an electron-phonon coupling time of typically several picoseconds for metals. Hence, the irradiation on a picosecond

or sub-picosecond timescale is separated from heat diffusion and the actual ablation processes which occur on a nanosecond to microsecond timescale. The laser-material interaction is confined to the irradiated area with limited effect on the surrounding material. This enables well-defined ablation geometries with micrometer size. The achievable structure quality, especially the negligible burr formation, often renders additional finishing steps after processing obsolete. Nevertheless, nonlinear interaction of the laser pulse with the ambient atmosphere can occur due to the high peak power of ultrashort pulses, especially in case of fs-pulses [84]. This effect can cause a widening and distortion of the beam profile and therefore an increased and disturbed ablation area. However, the nonlinear interaction can be reduced by increasing the pulse duration. Therefore, highest precision can be achieved in most cases with a pulse duration of a few picoseconds [35].

Laser pulses longer than the electron-phonon coupling time, especially with nanosecond duration or longer, excite the electrons rather slowly. Therefore, heat transfer to the lattice occurs almost instantaneously. In this case, all thermalization and ablation processes in fig.1.2 occur simultaneously and already during irradiation. This includes significant heat diffusion to the surroundings of the irradiated area and considerable generation of melt due to the slow heating rate. Therefore, the achievable geometrical precision and ablation quality is substantially decreased, not confined to the focal spot and suffers from pronounced melt expulsion and burr formation.

2 Short and Ultrashort Pulse Laser Drilling

The ablation process of a single pulse is well understood due to extensive experimental and theoretical investigations. Geometries of larger depth and aspect ratio which are generated by multiple pulses change the ablation behavior. This affects especially the ablation rate per pulse and the shape of the ablated volume [15, 19, 21, 26, 86, 87]. The most significant effects occur for laser drilling due to the generation of holes with large depth and high aspect ratio, especially with the method of percussion drilling. In this case, the focus position of the laser remains constant during the drilling process. Therefore, the hole diameter is determined by the size of the focal spot, typically less than $100\,\mu\text{m}$. In consequence, the ablation behavior during drilling is most severely influenced by the previously excavated hole.

This chapter focuses on the percussion drilling process with short and especially ultrashort laser pulses. At first, the current experimental techniques to study the drilling process are summarized in combination with a short discussion of their specific benefits and limitations. From these investigations, a qualitative model of the laser drilling process has been derived, the so-called Hirschegg-model. The final section of this chapter addresses the influence of the processing conditions on the drilling behavior, i.e. in particular the ambient pressure and the pulse repetition rate.

2.1 Techniques for Drilling Process Investigation

A simple, direct observation of the drilling process inside the hole is only feasible for transparent materials. This is not the case for metals, the most relevant material class for micromachining applications. The sole directly available quantity in this case is the break-through time for drilling through a certain material thickness [88, 89]. The

measurement of the break-through time also offers a rough estimation of the average ablation rate. Detailed information about the hole shape and the instantaneous ablation rate, however, can only be obtained with specialized experimental techniques.

2.1.1 Post-Process Shape Survey

In most investigations, the hole shape is surveyed after the drilling process. The sample is usually cut in two and polished to reveal a cross-section of the hole, either transverse or parallel to the hole axis [25, 40, 87, 90–93]. Fig. 2.1 shows drillings in Invar alloy prepared by this cut-and-polish method. Each cross-section from left to right represents a hole after an increasing number of applied pulses. Together, these images provide a first overview of the hole shape formation during the drilling process.
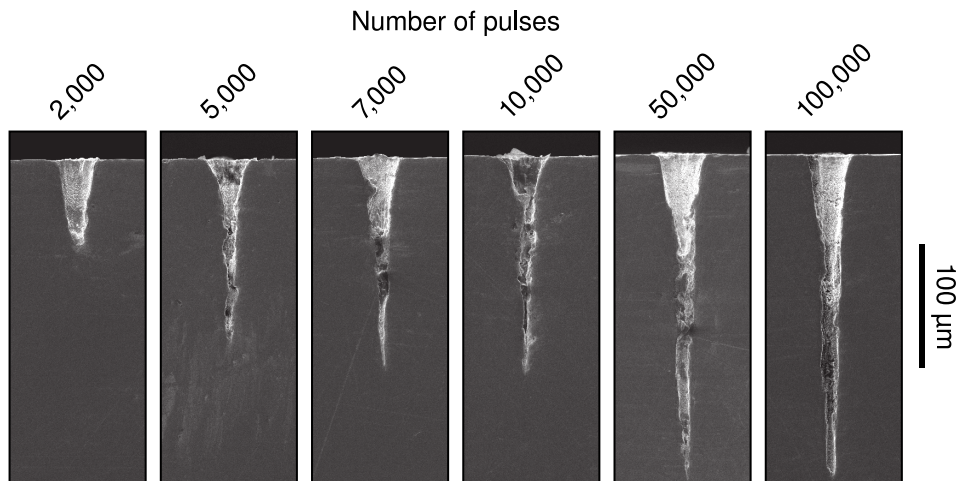
Fig. 2.1: Longitudinal sections of percussion-drilled holes in Invar alloy. Drilling was performed with ultrashort pulses of 8 ps duration at a fluence of 10 J/cm^2 with a focal spot diameter of ca. 28 µm.

This example illustrates the variation of the drilling progress and the hole formation with increasing depth and aspect ratio. Here, a significant decrease of the drilling rate can be observed after ca. 5,000 pulses. In addition a precise and accurate hole shape can only be found in the first cross-section after 2,000 pulses and in the upper part of the hole for a higher number of applied pulses. Bulges and indentations appear on the sidewalls in the lower part of the hole. There are also slight bendings and deviations from the straightness in the middle part of some holes, see e.g. the cross-section for

50,000 pulses in fig. 2.1. The position, size and direction of the bulges, indentations and bendings differs from hole to hole and the effects are not reproducible. Consequently, the actual evolution of these shape features cannot be reconstructed from a comparison of cross-sections from individual holes obtained by the cut-and-polish method. An advantage of this technique is the possibility to investigate the material composition and texture at the hole walls in addition to the shape, especially with respect to the heat-affected zone in the surrounding volume [26, 90].

Alternatively, the hole shape can be examined without complex sample preparation by confocal laser-scanning microscopy [94–96]. This technique can also provide a three-dimensional profile of the hole. However, the optical scanning in top view is only suitable for structures with low aspect ratio. Contours that are hidden from the top view, e.g. undercuts, cannot be revealed.

2.1.2 On-line Depth Measurement

The implementation of a confocal optical system in the drilling setup enables a tracking of the hole bottom [97]. Though, due to the necessary depth scanning, the repetition frequency of the measurement is limited to several tens of Hz. On-line depth profiling is possible by an optical cross-correlation technique that combines the reflection of the drilling pulse from the hole bottom and the hole walls with a gating pulse in a nonlinear crystal to analyze the runtime difference [98]. Here, a one-dimensional depth profile can be obtained in principle for every laser shot provided that a sufficient acquisition rate of the cross-correlation image is granted. The available spatial resolution depends on the pulse duration and is typically in the order of several microns for fs-pulses.

For ultrashort laser pulses, the velocity of the shock wave expansion above the workpiece depends on the hole depth, which also allows for a depth estimation with every laser pulse [99–103]. The radius of the shock wave can be identified from schlieren photography or shadowgraphy [101, 102]. Alternatively, the deflection of a probe laser [99, 100] or the size of the plasma region [103] can be analyzed. A well-defined correlation between the shock-wave/plasma and the hole depth is only valid within a certain range of depth and for specific applied fluence. In addition, the method also needs to be calibrated for every set of laser and material parameters.

Another fast option for on-line depth acquisition is inline coherent imaging [32]. Based on the principle of optical coherence tomography, it allows to follow the ablation front up to a depth of several hundred micrometers with micrometer resolution. On-line measurement of the hole depth and also on-line control of the drilling progress with this technique has been demonstrated at acquisition rates up to several tens of kHz [104]. Even higher spatial and temporal resolution is provided by self-mixing interferometry [33, 105]. Here, the light of an additional laser diode is coupled into the beam path of the drilling laser to the workpiece. The back reflection from the hole bottom causes interference within the laser diode and results in an amplitude modulation in dependence of the distance to the hole bottom. Due to the interferometric principle, the hole depth can be measured with a resolution of a few hundred nanometers. The available acquisition rate of the measurement is in the order of several hundred kHz.

All the above-mentioned methods mainly grant access to the hole depth only and do not provide information of the hole shape. Therefore, the formation of special hole shape features as for example undercuts, bendings and bulges cannot be revealed.

2.1.3 Direct Observation Techniques

A direct microscopic observation of the hole shape formation during laser drilling is possible for materials that are transparent for imaging with standard optical methods[1].

A suitable material is for example a polymer like polymethylmethacrylate (PMMA), which can be machined by UV-radiation [23]. Furthermore, certain kinds of ceramics are semi-transparent and can even obtain metal-like absorption properties under irradiation due to heating by the laser pulse [19, 24]. This applies in particular to laser drilling with ns-pulses in the near infrared spectral region, e.g. at 1064 nm. In both cases, however, the material properties differ significantly from those of metals. This applies especially to the heat conductivity, which determines the size of the heat-affected zone, see also chapter 1. In addition, the brittleness of ceramics can favor a decomposition along the grain boundaries [24].

---

[1]Alternatively, non-optical imaging diagnostics can be applied for investigations of laser materials processing, e.g. x-ray or ultrasonic imaging [2, 3, 106–108]. These techniques also have specific limitations with respect to material selection and available resolution, though, and are not within the scope of this work.

Ultrashort laser pulses with their extremely high peak intensities can also ablate materials that are intrinsically transparent for the laser radiation due to nonlinear interaction mechanisms like field ionization and multiphoton absorption. This enables drilling of holes with large depth and high aspect ratio in dielectrics like glass, quartz and diamond similar to drilling in metals, but in combination with a direct observation of the hole shape formation [21, 28, 29]. Nevertheless, the material properties as well as the ablation characteristics differ from intrinsically absorbing substrates like metals, see e.g. the significant difference of the ablation threshold which is in the order of $0.1\,\mathrm{J/cm^2}$ for metals [51, 109, 110], but approximately $1\,\mathrm{J/cm^2}$ for dielectrics in the ps-regime [12, 111].

The expansion of the ablation plume can also be directly observed for drilling in transparent materials by imaging the plasma luminescence in the visible spectral region [2, 37]. To observe the plasma from metal ablation, an artificial hole with transparent sidewalls can be created by integrating a thin metal foil with a prefabricated channel with open front and back between two glass plates [112]. However, this artificial environment is different from a real laser-drilled hole. Besides, it only allows for the observation of a few pulses until the walls become non-transparent due to debris.

In summary, up to now there exists no experimental technique for the direct observation of ultrashort pulse laser drilling in an opaque, metal-like material. Therefore, all existing descriptions of the drilling behavior and their explanations are based on laser parameters or material properties that differ from the typical conditions of metal ablation.

2.2 Model Description of the Drilling Process

From the experimental investigations described above, especially the in-situ observation of percussion drilling with ns-pulses in semitransparent ceramics, a qualitative model description of the drilling process has been developed [19, 24]. This model is referred to as the Hirschegg-model[2] in literature [24, 44, 113–115].

---

[2]This model was developed during two workshops on laser drilling, held in Hirschegg, Austria [113].

The development of the hole depth d in dependence of the number of laser pulses N is described as

$$d \propto N^\chi . \tag{2.1}$$

The parameter χ defines the characteristic of the depth increase. A value $\chi = 1$ refers to a linear increase of depth and accordingly a constant drilling rate. For $\chi < 1$ the depth increase is retarded with an increasing number of pulses and the drilling rate gradually decreases. On the other hand $\chi > 1$ denotes an increasing drilling rate. Fig. 2.2 presents a schematic illustration of the depth evolution during a drilling process according to the Hirschegg-model. The values for depth and the number of pulses indicate the typical dimensions for ns-pulse drilling of ceramics and are given for reference only [24]. The actual values for different drilling conditions depend on the material as well as processing parameters. According to the χ-parameter, four consecutive process stages can be distinguished in the development of the laser-drilled hole.
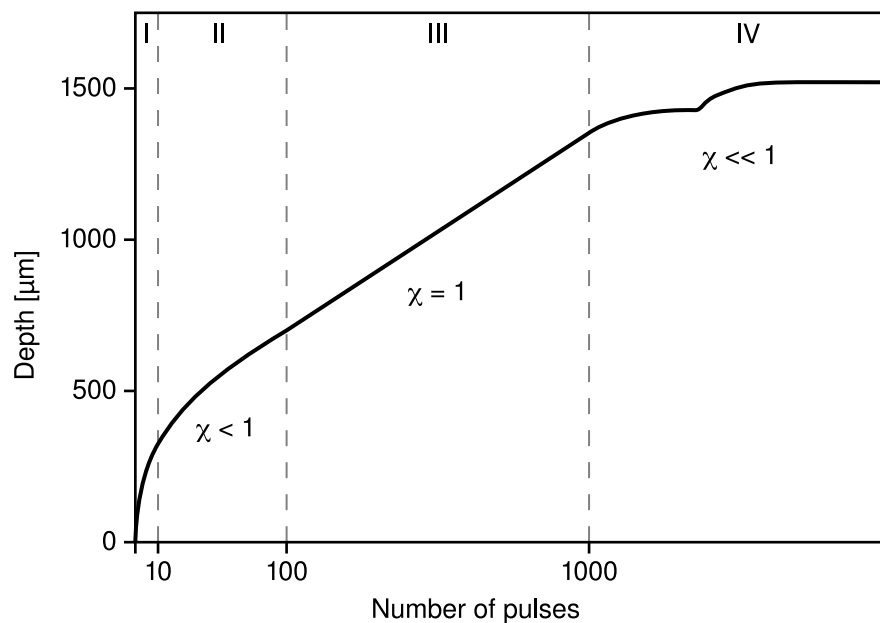

Fig. 2.2: Principal development of hole depth during percussion drilling according to the Hirschegg-model with four consecutive process stages. The values of the hole depth and the number of pulses indicate the typical dimension only and are not drawn to scale.

I The beginning of the drilling process, when ablation occurs at a nearly planar surface, shows the highest drilling rate. This is especially pronounced in case of ceramics due to the fracture of the grain structure. The first stage lasts only for the first few pulses until an ablation crater is formed.

II In the second stage, the hole capillary is formed. The aspect ratio can reach a final value of up to five. The ablation rate gradually decreases and this stage is thus characterized by a parameter $\chi < 1$. In total, the drilling rate may drop by a factor of ten. This effect can be caused by various factors and their mutual interactions [15]. The irradiated area is increased compared to the flat sample surface at the beginning of the drilling process and therefore reduces the effective fluence. Heat conduction occurs also along the sidewalls in addition to the hole bottom and leads to a faster decrease of the lattice temperature after irradiation. The material expulsion from the hole capillary is hindered compared to ablation at the surface. And the plasma shielding is increased due to the restricted expansion of the plasma plume inside the hole channel.

III In the ensuing third stage, the drilling rate stabilizes at a constant level. Therefore, the hole depth increases linearly with $\chi \approx 1$. This behavior can be attributed to a balance of increasing propagation losses at larger depth with a simultaneously decreasing plasma absorption for the corresponding lower intensities [24]. During this phase, a straight-lined, nearly cylindrical hole channel is formed.

IV In the final fourth stage, the drilling rate decreases significantly with $\chi \ll 1$ until the drilling process stops completely. The end of the drilling process either occurs abruptly or by a gradual decrease of the ablation rate. In some cases, an unstable drilling progress has been observed during this fourth stage with a variation of the ablation rate over two orders of magnitude [24]. In particular, there can be short periods of time with a fast increase in depth similar to stage three followed by longer periods with only minor growth of the hole. During this final process stage, the direction of drilling can deviate from the center axis defined by the incident beam direction. This can result in a bending of the hole as well as the formation of multiple additional capillaries with different orientation.

The depth development described by the Hirschegg-model is also in good agreement with in-situ observations of the drilling process under different conditions and for other materials, for instance fs-pulse and ps-pulse drilling of PMMA and diamond [21, 31].

Beyond that, the special shape formation during the fourth process stage, including bending of the hole and formation of additional hole channels, is also characteristic for different materials and processing conditions, e.g. drilling of PMMA and diamond [21, 31], fs-pulse drilling of metals [25] as well as silicate glasses [29, 37] and even continuous wave irradiation of PMMA [23].

The evaluation of drilling in metals by the cut-and-polish method shows in principle a similar development of the drilling rate as the Hirschegg-model [19, 31]. However, the limitations of this method does not allow for a detailed assessment of the process stages. Besides, there are studies of fs-pulse drilling in stainless steel and aluminum that show a continuous decrease of the drilling rate throughout the entire drilling process [20]. In this case, no well-defined third process stage can be observed. More recent investigations of ps-pulse drilling in stainless steel by on-line depth measurements show also a continuously decreasing drilling rate [32, 104]. Moreover, an unstable process behavior with a variation of the drilling rate is observed already at an early process stage [32]. The presence of hole shape deviations, i.e. bulges, indentations and bending of the hole, can also be observed at comparably low hole depths for ultrashort pulse drilling in metals, see for example fig. 2.1 on p. 14. These effects are therefore not necessarily limited to the fourth process stage or the end of the drilling process, respectively. After the end of the initial drilling process, a restart of ablation from the top of the existing hole has been observed in certain investigations of fs-pulse drilling in stainless steel [116, 117]. This effect can result in a significant widening of the hole if irradiation is not stopped at the right time.

Several explanations based on different approaches have been put forward for the deviation of the drilling direction from the incident laser beam during the last process stage. The bending of the hole might be induced by a material inhomogeneity located at a certain depth which facilitates ablation in transverse direction [21]. The effect can also be caused by Fresnel reflection at the walls of the hole channel [21, 24]. For linearly polarized light, reflection is stronger for light polarized perpendicularly to the plane of incidence on the sidewall compared to parallel polarization. Hence, bending always occurs perpendicular to the polarization of the laser. The necessary initial asymmetry might be induced by fluctuations of the pulse intensity distribution, material defects, deposition of ablation particles or asymmetric material removal. The polarization dependence of reflection is also known to cause deviations from a circular

hole cross-section in large depths [27, 118]. This effect can be suppressed by rotating the polarization during drilling or applying circularly polarized light [2, 119]. Beside the polarization, a modified intensity distribution at the hole bottom can also be explained by the waveguide character of the hole capillary [120]. Nevertheless, a significant effect occurs only for very small hole diameters, i.e. a hole aperture in the range of the wavelength of the incident light. Such holes of micrometer or even sub-micron size shall not be discussed here, though.

In the framework of the Hirschegg-model, the laser-induced plasma plays an important role to explain the characteristic evolution of the drilling rate with increasing depth [24]. In contrast, this behavior can also be attributed to damping losses of the pulse propagation inside the hole channel in combination with different domains of ablation rate in dependence of the locally incident fluence, which is in in good agreement with the observations [22]. The plasma and the laser-ablated particles inside the hole can also act as a secondary source of ablation according to the Hirschegg-model [19, 24, 121]. In particular, the transverse widening of the hole can be attributed to the abrasive effect of the plasma while the incident laser pulse mainly causes ablation in forward direction. The abrasion of the sidewalls can be induced by an abrasive effect of the ablation particles during their ascent from the hole bottom as well as the energy transfer from the hot plasma to the sidewalls, which heats them to the point of evaporation [2, 34, 91]. In addition to the plasma generated by ablation at the hole bottom, the high peak-intensities of ultrashort pulses can induce plasma formation in the atmosphere within the hole channel [35, 36]. This effect is enhanced by residual material vapor inside the hole [122]. Therefore material removal from the sidewalls is possible even far away from the hole bottom due to these secondary sources of ablation.

On the other hand, the plasma formation inside the hole channel can also cause a deflection of the laser beam. Observations of the plasma during drilling in silicate glass showed a nonuniform plasma distribution and a fluctuation of the plasma position from pulse to pulse [37]. Deflection at the plasma filament may therefore randomly change the beam pointing and hence shift the ablation spot for every pulse. This explanation is also applied to drilling in metallic samples [25, 26]. However, it is not fully understood how a randomly changing position of ablation from pulse to pulse can finally result in the formation of well-defined capillaries rather than a general widening of the cavity at the bottom of the hole.

For drilling with long laser pulses, especially in the nanosecond and microsecond regime, the expulsion of the generated melt plays an important role in the hole shape formation as well [123]. The recoil pressure from the laser pulse causes a melt flow to the hole walls and towards the hole entrance, which enlarges the hole at the bottom. The formation of recast narrows the hole in the upper part, though.

2.3 Influence of the Processing Conditions on the Drilling Behavior

A change of the processing conditions can significantly affect the drilling behavior. This concerns in particular the ambient pressure and the time delay between subsequent pulses. The ambient pressure influences the material vapor flow and the density of particles within the ablation plume. Eventually, a reduced ambient pressure decreases the possible abrasive effect of the material vapor as well as the laser ignition of plasma within the capillary. The time delay between consecutive pulses, respectively the pulse repetition rate, has a decisive influence on the interaction of the subsequent pulse with the previously generated ablation products.

2.3.1 Drilling under Reduced Ambient Pressure

In general, a reduction of the ambient pressure leads to an increase of the ablation rate [51]. For a pressure reduction from 1 bar (atmospheric pressure) to 100 mbar, the average drilling rate of stainless steel and aluminum in the ultrashort pulse regime shows an increase of ca. 30% to 50% at a fluence of ca. $10\,\mathrm{J/cm^2}$ [20, 124, 125]. A similar increase is observed for drilling with ns-pulses [126]. The achievable drilling rate normally increases with applied fluence but saturates under atmospheric pressure for high fluences $\gg 10\,\mathrm{J/cm^2}$. At reduced ambient pressure, a continuous increase of the achievable drilling rate can be observed even for high fluences. Therefore, compared to atmospheric pressure, an enhancement of the drilling rate up to a factor of ten can be achieved at a fluence of $190\,\mathrm{J/cm^2}$ and pressure reduction to 100 mbar [34, 118]. However, the positive effect of pressure reduction on the drilling rate is only effective for lowering the ambient pressure down to ca. 100 mbar. Further pressure reduction does not lead to a further enhancement of the ablation rate [34, 118, 125].

In addition, the hole shape formation is also influenced by the ambient pressure. Holes drilled at atmospheric pressure show a widening of the hole during the drilling process once the hole exceeds a certain depth [36, 91]. This is attributed to the generation of a laser-induced plasma inside the hole as a secondary source of ablation, see also section 2.2. Under vacuum conditions, this effect does not occur due to the lack of ambient gas and the faster expansion of the material vapor, which prevents the plasma ignition and abrasion of the hole walls. As a consequence, more pulse energy is available for ablation at the hole bottom and hence an increased drilling rate is observed. In addition, a smaller hole diameter is achieved compared to atmospheric pressure, especially for large drilling depths [124]. As a consequence of this interpretation, the influence on the hole shape due to the plasma generated in the ablation process at the hole bottom is negligible compared to the effect of the laser-induced plasma within the hole channel. However, it is not fully understood why the widening of the hole under atmospheric pressure conditions usually starts at the top of the hole [21, 116, 121]. In addition, the enhancement of the drilling rate at the beginning of the process before the formation of the hole capillary cannot be explained with this model. The distortion of the laser pulse in front of the sample surface due to nonlinear effects in the atmosphere could also explain the widening of the hole [35].

The pressure effect on the ablation rate can also be explained quantitatively with a purely thermodynamic model [125]. Here, the ablation rate is derived from the evaporation flux given by the Hertz-Knudsen equation, which is linked to the ambient pressure [1]. This model is able to describe the increase of the drilling rate under reduced pressure and especially the saturation of the effect for pressure reduction below 100 mbar in good agreement with the experimental observations.

2.3.2 Drilling at High Repetition Rates

The available pulse repetition rate is a key parameter to optimize the processing time for fixed laser parameters like pulse energy or fluence. With increasing repetition rate, the delay between consecutive pulses will decrease to the range of characteristic timescales of the ablation process, especially with respect to the particle emission from the surface and the vapor flow of ablated material, see also sections 1.2 and 1.3. For ultrashort pulses, the transmission through the ablation plume is reduced in a range of several hundred nanoseconds to one microsecond after irradiation [65]. The expansion of the

ablation plume even lasts for several hundred microseconds [84] and an influence of the laser-generated particles on the ionization threshold of the ambient atmosphere can still be observed on a timescale of seconds [15].

In experimental investigations of the drilling efficiency, i.e. the number of pulses to drill through a certain material thickness, the expected interaction has been found for a real drilling process [88, 127, 128]. The results for drilling through 0.5 mm thick stainless steel with pulses of 800 fs duration (FWHM) are shown in fig. 2.3.
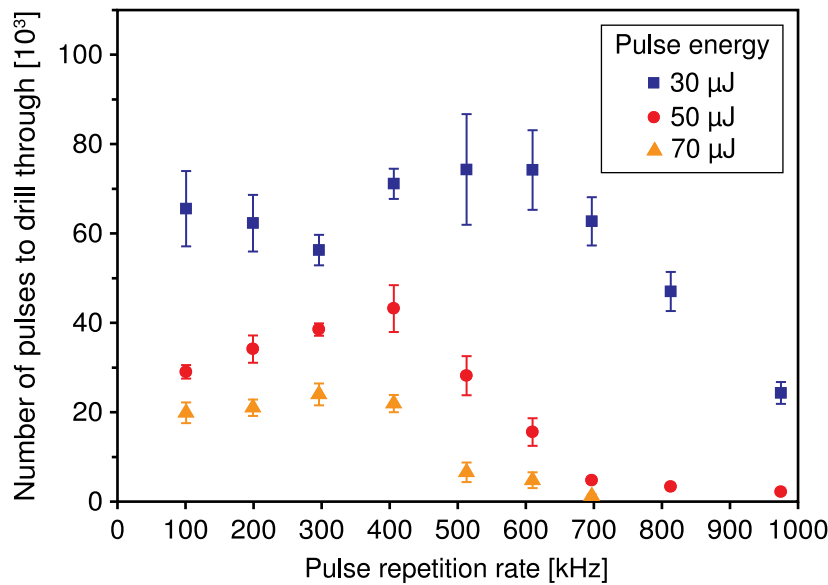

Fig. 2.3: Number of pulses to drill through 0.5 mm of stainless steel in dependence of the repetition rate for pulses of ca. 800 fs duration (FWHM) at a wavelength of 1030 nm [127]. For repetition rates of ca. 400 kHz to 600 kHz, the pulse number reaches a maximum due to particle shielding. Repetition rates > 600 kHz show a significant decrease of the required number of pulses to drill through due to the heat accumulation effect.

The necessary number of pulses to drill through increases when the pulse repetition rate is increased to a few hundred kHz due to shielding of the sample by the ablation products from the previous pulse, see fig. 2.3 from 300 kHz to 500 kHz at a pulse energy of 30 µJ. However, further increase of the repetition rate to several hundred kHz shows an enhancement of the drilling efficiency and reduces the number of pulses required for perforation. Eventually, this enhancement can outperform the particle shielding effect, see fig. 2.3 for repetition rates > 600 kHz, and may lead to a drilling efficiency even higher than for low repetition rates, compare ca. 1 MHz to 100 kHz. This behavior is caused by the part of the absorbed pulse energy that is not transformed into energy

of the ablation products, but remains as heat within the bulk material. If the temporal separation of subsequent pulses is lower than the characteristic time of heat diffusion, typically on a microsecond timescale, a significant heat accumulation and therefore rise of the temperature occurs at the irradiated spot. Since less pulse energy is required for material heating and ablation, this heat accumulation effect increases the drilling rate. The amount of residual heat increases for higher incident fluence [35]. Therefore, the onset of heat accumulation is shifted to lower repetition rates for higher pulse energies, see the different pulse energies in fig 2.3. A longer pulse duration has a similar effect [127]. Naturally, the heat accumulation also depends on the material's thermal characteristics, but these properties also influence the particle shielding effect. For materials with a high thermal conductivity, e.g. copper and tungsten, a nearly constant drilling efficiency is observed for repetition rates up to 1 MHz [127, 128].

2.4 Current State of Knowledge

The Hirschegg-model is the state-of-the-art description of the drilling process with short and ultrashort laser pulses. It allows an estimation of the depth evolution during drilling of metals and metal-like materials. However, the Hirschegg-model is not directly applicable to this specific process since it is based on experimental studies that use different laser parameters, e.g. ns-pulses, or materials with different properties and ablation characteristics, e.g. polymers, ceramics, quartz, diamond, glass. On-line measurements of the depth evolution for drilling of stainless steel show considerable fluctuations of the drilling rate throughout the complete drilling process. Intermediate periods of constant depth are a pronounced feature of the drilling behavior. They occur already at an early stage and are not limited to the end of the process. The formation of peculiar shapes in the lower part of the hole, especially hole bends and additional capillaries, can be explained by several, partially contradictory theories. Up to now, there exists no detailed investigations of the hole shape evolution during ultrashort pulse drilling of metals. Current experimental methods are mainly limited to depth measurement and a post-process survey of the hole shape when dealing with opaque materials. To clarify the process behavior and the mechanisms involved in the shape development, an in-situ observation of the shape formation during the drilling in a metal, or at least a metal-like model material, is necessary.

3 In-situ Imaging of the Drilling Process

Within the scope of this study, a semiconductor is used as the sample material for laser drilling. In general, a semiconductor is transparent for photons with an energy below the band gap and at the same time opaque for photons with higher energy. The ablation behavior of a semiconductor for ultrashort laser pulses with photon energy above the band gap is similar to a metal [15]. The results of the in-situ imaging experiments presented in chapter 4 and 5 are therefore representative for both material classes.

3.1 Model System for Drilling in Opaque Materials

With respect to the typical wavelengths of ultrashort pulse lasers used for micromachining, i.e. in particular 1030 nm but also 800 nm and 515 nm, silicon is selected as the sample material. With a band gap energy of ca. 1.17 eV at 300 K [41], this semiconductor is transparent for light with a wavelength larger than $\lambda_{\text{band-gap}} \approx 1100$ nm and opaque in the region of shorter wavelength. Nevertheless, silicon shows a gradual transition from the transparent to the absorbing region. The linear absorption coefficient at 515 nm is $\alpha_{515\text{nm}} \approx 1.46 \cdot 10^6 \, \text{m}^{-1}$ [129] which corresponds to an optical penetration depth in the submicron regime of $l_{\alpha,515\text{nm}} = \alpha_{515\text{nm}}^{-1} \approx 680$ nm while the absorption at a wavelength of 1030 nm is significantly lower, $\alpha_{1030\text{nm}} \approx 2.41 \cdot 10^3 \, \text{m}^{-1}$ [129] and accordingly $l_{\alpha,1030\text{nm}} \approx 415 \, \mu\text{m}$. On the other hand, the additional, strong nonlinear absorption in silicon reduces the effective absorption length to a few hundred nanometers. Fig. 3.1 shows a simulation of the intensity distribution of an ultrashort laser pulse at 1030 nm inside a silicon sample (I_{sample}) and the resulting lattice temperature T_{lat}, which is calculated from the Two-Temperature-Model according to equation 1.1 on p. 6.

The simulation accounts for two-photon absorption and the change of the optical parameters due to the generation of free carriers by the laser pulse, based on models commonly used in literature [52, 59, 64, 130]. A detailed description of the simulation can be found in appendix B, p. 103.
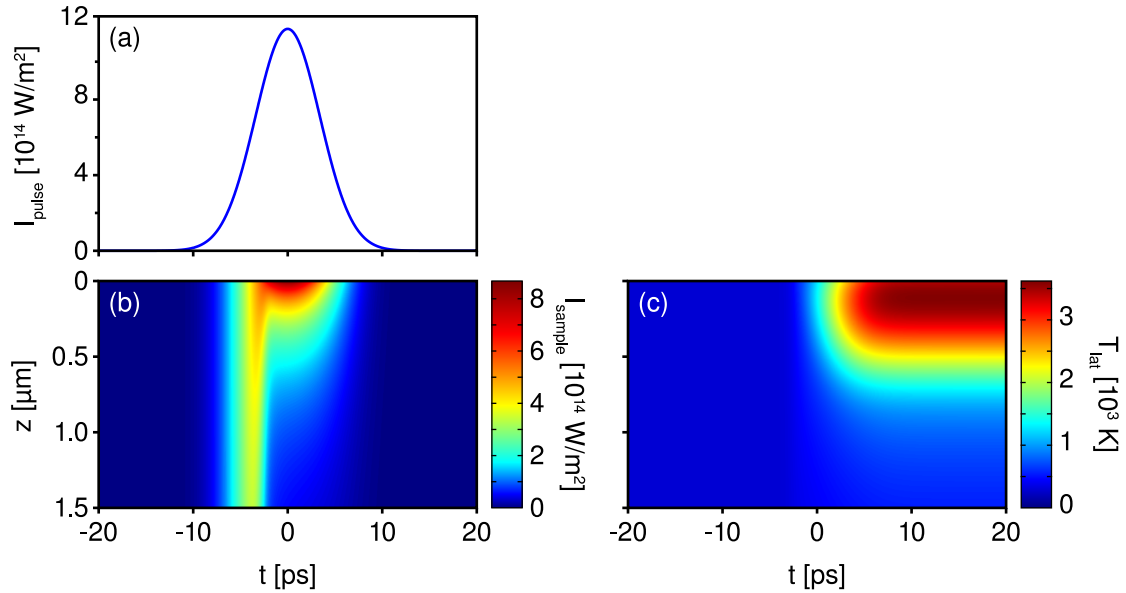

Fig. 3.1: Simulation of the ultrashort pulse absorption in silicon at a wavelength of 1030 nm. The intensity of the pulse (a) with a fluence of $F = 1\,\text{J/cm}^2$ and a duration of 8 ps (FWHM) is mainly absorbed close to surface (b) and leads to a corresponding increase of the lattice temperature (c) according to the Two-Temperature-Model.

At the beginning of the pulse, the light is transmitted deep into the sample. At this time, both nonlinear and linear absorption lead to a rapid increase of the free electron density. Consequently, the linear absorption is significantly increased and the main part of the pulse is absorbed close to the surface, see fig. 3.1 (b). At the pulse maximum ($t = 0\,\text{ps}$), the effective absorption length is reduced to approximately 300 nm. The rise of the lattice temperature also occurs only within a thin surface layer with less than 1 μm thickness, see fig. 3.1 (c). For a higher incident fluence or shorter pulse duration, the absorption would increase even faster and lead to a more confined energy deposition at the surface. Therefore, the energy distribution within silicon is comparable to the irradiation of metals and results in a similar ablation behavior, i.e. especially a comparable ablation threshold and similar dependence of the ablation depth on the incident fluence. This similarity has been shown in previous experimental investigations

of ultrashort pulse surface ablation of silicon [43, 131]. A comparison of the ablation threshold for different metals and silicon in the ps-regime is given in tab. 3.1. With a threshold fluence for ablation of ca. $0.26\,\text{J/cm}^2$ at 1030 nm there is a good agreement with the typical range for metals between ca. $0.05\,\text{J/cm}^2$ and $0.5\,\text{J/cm}^2$. In comparison, for a photon energy below the band gap and absorption through nonlinear processes, as for example in dielectrics, the ablation threshold increases to values $> 1\,\text{J/cm}^2$ [132].

Tab. 3.1: Threshold fluence for ablation F_{th} of different metals and crystalline silicon, including stainless steel of grade 1.4401. The values are measured with the method of Liu [133] for irradiation by 100 pulses with a pulse duration of 8 ps (FWHM) at a wavelength of 1030 nm.

	Al	W	Cu	Steel	Si
F_{th} [J/cm^2]	0.12	0.08	0.48	0.15	0.26

The gradual decrease of linear absorption in silicon with increasing wavelength is also a benefit for the in-situ observation. For a wavelength just below the band edge, e.g. 1060 nm, the transmission through a thin sample (thickness typically < 1 mm) is already high enough to produce a high-contrast image on a standard camera with a silicon-based sensor. Special optics or sensor devices as used for imaging in the infrared spectral region at wavelengths > 1100 nm are not required.

Furthermore, silicon offers additional advantages for the investigation of laser drilling:

- The heat conductivity, a key parameter for the heat diffusion, is ca. 156 W/m·K for silicon [134], which is within the typical range for metals with ca. 40 W/m·K for steel to 400 W/m·K for copper [135]. This is not the case for dielectrics with a typical heat conductivity of < 1 W/m·K [135].

- Wafer-grade silicon is available with high purity and uniformity. Therefore, material inhomogeneities can be excluded as a major influence on the drilling process.

- From previous studies of ultrashort pulse drilling in silicon, a hole depth in the range of a few hundred to several hundred micrometers for a hole entrance diameter of a few tens of micrometers can be expected [22]. These hole dimensions offer an adequate drilling depth and aspect ratio (typically $< 100:1$). On the other hand, the hole size is not too large, thus even small-sized shape features, e.g. the bulges and indents on the sidewalls with typical dimensions of only a few micrometers, can be observed.

- Ultrashort pulse ablation of silicon shows a large amount of particle agglomerations and debris in the vicinity of the ablation structures [136]. This allows for a detailed investigation of the influence of those particle depositions on the drilling behavior.
- Silicon is a brittle material, which enables the preparation of cross-sections by cleaving. In contrast to grinding and polishing, the hole interior remains unchanged during the preparation process, which is essential for the characterization of particle depositions inside the hole in addition to the shape information.

Therefore, crystalline silicon is deliberately selected as the sample material for the investigation of the laser drilling process. Due to its characteristic ablation behavior, it is used here as a model system for ultrashort pulse laser drilling of semiconductors and metals.

In general, other semiconductors could also be used as the sample material, e.g. germanium or III-V semiconductor compounds. However, in case of germanium with $\lambda_{\text{band-gap}} \approx 1900\,\text{nm}$ at $300\,\text{K}$ [41] this would require special light sources and image capturing equipment. On the other hand, III-V semiconductors like indium-phosphide (InP) or gallium-arsenide (GaAs) offer high linear absorption with absorption coefficients up to $10^7\,\text{m}^{-1}$ due to their direct band gap [137]. However, the large band gap energies of these compounds narrows down laser wavelengths for irradiation, e.g. to $\lambda < 970\,\text{nm}$ in case of InP [41], which excludes laser systems at $1030\,\text{nm}$. In addition, the ablation products of these compounds are toxic and therefore significantly complicate the handling of these substances.

3.2 In-situ Imaging System

Figure 3.2 shows the basic setup and general instrumentation for the in-situ imaging of the drilling process. The samples are made of prime grade crystalline silicon wafers (provided by Siegert Wafer, Aachen) with n-type or p-type doping at a resistivity of $1\,\Omega\text{·cm}$ to $20\,\Omega\text{·cm}$, which corresponds to a low dopant concentration of approximately $10^{14}\,\text{cm}^{-3}$ to $10^{16}\,\text{cm}^{-3}$ [138].

In general, the sample is irradiated by an ultrashort laser pulse with a duration of ca. $8\,\text{ps}$ (FWHM) at a center-wavelength of $1030\,\text{nm}$. A pulse duration in the range of a few picoseconds is typically used in ultrashort pulse laser processing of opaque materials,
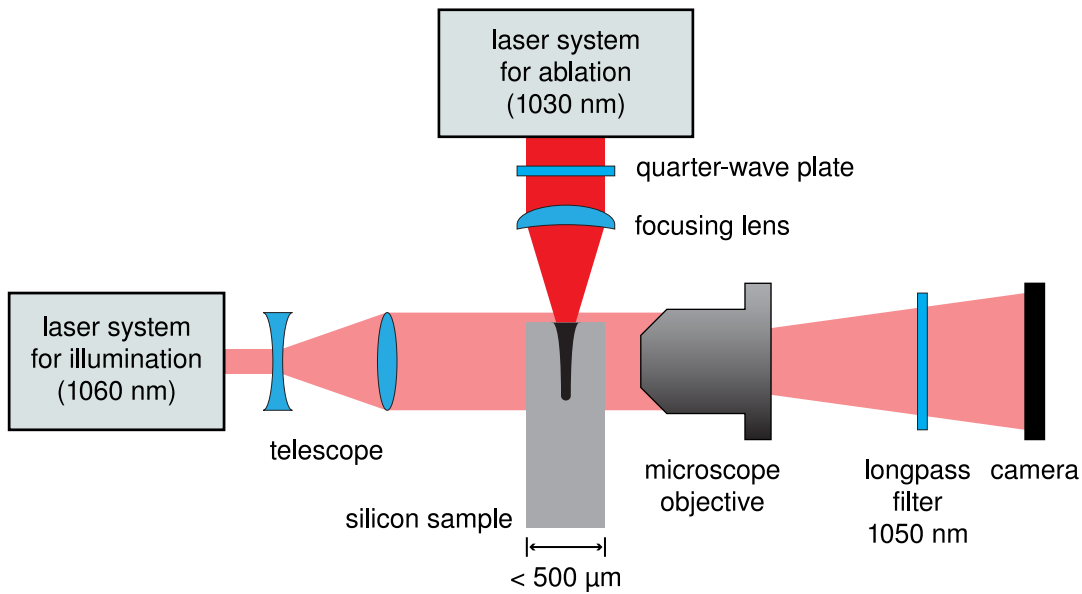
Fig. 3.2: Basic setup for in-situ imaging of percussion drilling in a silicon sample.

especially metals and semiconductors [35, 44]. The laser system (Trumpf TruMicro 5050) delivers a maximum pulse energy of 125 μJ at repetition rates up to 400 kHz. A quarter-wave plate ensures a circular polarization which prevents polarization-dependent effects [2, 119]. The laser is focused on the top surface of the sample with a meniscus or plano-convex lens. In most experiments, a focal length of 100 mm is used, resulting in a focal spot size of about 25 μm, which is typical for most micromachining applications today. The focal position remains fixed during the complete duration of irradiation. This procedure is generally referred to as percussion drilling and generates the smallest feature size with respect to the laser focus in combination with a large depth. The diameter of the resulting hole is in the order of the focal spot diameter. Therefore, a considerable effect of the hole capillary on the ablation behavior can be expected. The crystalline samples are positioned with <100> orientation perpendicular to the drilling direction[1].

During drilling the sample is simultaneously illuminated by a second laser at a wavelength of 1060 nm perpendicular to the drilling laser beam. A telescope setup in front of

---

[1]Preliminary experiments with samples of different crystal orientation showed no influence of the actual orientation on the ablation process and the drilling behavior. Similar observations were made in previous studies on silicon ablation [131]. The effect of the crystal orientation is therefore not subject to further investigations within the scope of this work.

the sample provides a homogeneous illumination of the region of interest. A microscope objective (with numerical aperture of 0.1 or less) projects the image onto a standard camera (Photonfocus DS1-D1312-160-CL-10 or Basler scA1000-20fm). The desired magnification and according resolution can be adjusted by changing the distance between sample, objective and camera. An additional longpass filter (Thorlabs FEL1050) suppresses scattered radiation of the drilling laser to avoid glare in the image. The walls of the laser-generated hole cause high scattering losses for the transillumination and the silhouette of the hole is visible as a dark region in the image. The hole silhouette always shows the complete outline of the hole shape, i.e. a superposition of all branches, bendings and indents within the line of sight. In contrast, a section prepared by the cut-and-polish method only shows the shape within the particular section plane, i.e. branches and other shape features that are not located within this plane are hidden from view. Nevertheless, the in-situ imaging technique does not reveal the interior of the hole. Structures that extend to the inside of the hole are not observable with this imaging method.

For the experiments, the drilling laser is typically operated at a pulse repetition rate of 200 Hz while the camera captures fifty images per second, which means one image of the hole for every four pulses. The basic imaging setup has been adapted with different laser systems, focusing lenses and positions and additional imaging equipment as well as a vacuum chamber to change the ambient pressure in order to investigate different drilling conditions. A detailed description of the respective configuration of the setup can be found in the context of the individual parameter studies in the following chapters.

4 Hole Shape Formation

This chapter covers the shape evolution and depth development during laser percussion drilling for different laser parameters, e.g. pulse energy, laser wavelength, pulse duration as well as different processing conditions, e.g. applied fluence and focus position. All investigations were carried out in air and under atmospheric pressure. Characteristic process phases are identified. A general description of the hole formation process is developed from the experimental results and discussed with special regard to previous studies of the hole formation.

4.1 Hole Shape Evolution

The typical evolution of percussion drilling in silicon, recorded with the in-situ imaging system, is shown in fig. 4.1. The images display the unedited raw material of the camera in pseudo-color. The dark blue area in the images represents the longitudinal section of the hole. In this example, a pulse energy of $25\,\mu$J, corresponding to a fluence of $8\,\text{J/cm}^2$, is used for drilling at a pulse repetition rate of $100\,\text{Hz}$. Only timesteps with a significant change in the hole geometry are shown in the figure to illustrate the main features of the hole shape evolution.

In the first few hundred pulses, approximately up to $N = 200$, the hole capillary is excavated with tapered sidewalls and a funnel-shaped entrance due to the Gaussian intensity profile of the drilling laser beam. The bottom of the hole resembles a hemispherical dome. During this time, directly at the beginning of the process, the average drilling rate has the highest value with about $500\,\text{nm/pulse}$. Afterwards, the drilling efficiency significantly decreases to ca. $120\,\text{nm/pulse}$ for the period from 200 to 500 pulses. The hole maintains its principal shape while it further expands into depth. The entrance diameter is ca. $25\,\mu$m, which correlates to the spot size at the surface for focusing with a lens of $100\,\text{mm}$ focal length, see also tab. 4.1 on page 43.
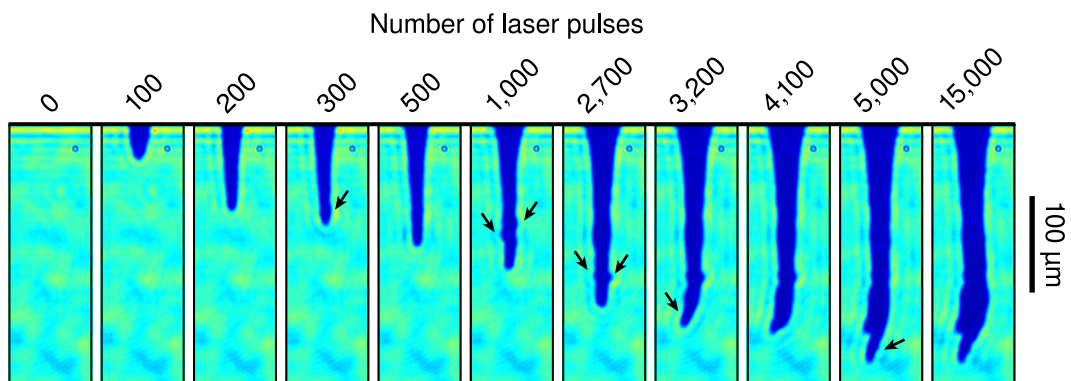
Number of laser pulses

Fig. 4.1: Trans-illumination images of a typical percussion-drilled hole in silicon with ps-pulses at 1030 nm using a fluence of 8 J/cm^2. The sample surface is located at the top of the images. Arrows indicate the formation of special hole shape features, e.g. indentations or hole bends.

After 500 pulses, the hole depth is ca. 125 µm and the corresponding aspect ratio approximately 5 with respect to the entrance diameter.

Drilling then continues with a further decrease in the drilling rate to ca. 50 nm/pulse at 1,000 pulses and ca. 30 nm/pulse at 3,000 pulses. In addition, ablation now also occurs in transverse direction along the sidewalls of the hole several micrometer above the hole bottom. This leads to the formation of indentations and bulges on the sidewalls and hence an increased diameter in a certain depth, see the arrow in fig. 4.1 at 1,000 pulses. The initial bulges may increase in size by subsequent pulses and also new ones may be formed, see the situation after 2,700 pulses for example.

At this depth (ca. 200 µm), the hole reaches a state in which the drilling direction is no longer determined by the incident beam and a bending of the capillary occurs, clearly visible after 3,200 pulses in this example. Drilling in forward direction then stops and the depth does not increase till 4,100 pulses. Nevertheless, ablation still takes place at the outside of the bend and flattens its curvature. In the following, drilling can resume in forward direction and lead to the formation of a new borehole front, as indicated by the arrow at 5,000 pulses. This behavior may lead to the formation of multiple branches, which can grow in any random direction, as observed in further studies.

The continued observation of the drilling process from 5,000 up to 15,000 pulses showed no further increase in hole depth. The sidewalls of the hole still get ablated at a very low rate by the side wings of the Gaussian beam profile, which leads to a slight increase of the

hole diameter. The middle part of the hole becomes more cylindrical compared to the tapered shape before and the bulges are reduced in their extent due to this effect. Finally, for the given process parameters in this example, a hole with a depth of ca. 250 μm at an entrance diameter of ca. 35 μm is drilled. While the upper part shows the typical funnel shaped entrance and tapered geometry of a percussion drilled hole, the lower part consists of multiple branches that deviate from the drilling direction determined by the incident laser beam.

For comparison, fig. 4.2 shows hole sections that have been prepared by the cut-and-polish method. These sections show the typical shape features of the hole, especially the bending and formation of bulges and multiple branches, in good agreement with the observations by in-situ imaging in fig 4.1. However, each image in fig. 4.2 is obtained for a different hole and the evolution of individual features is not traceable with this technique.
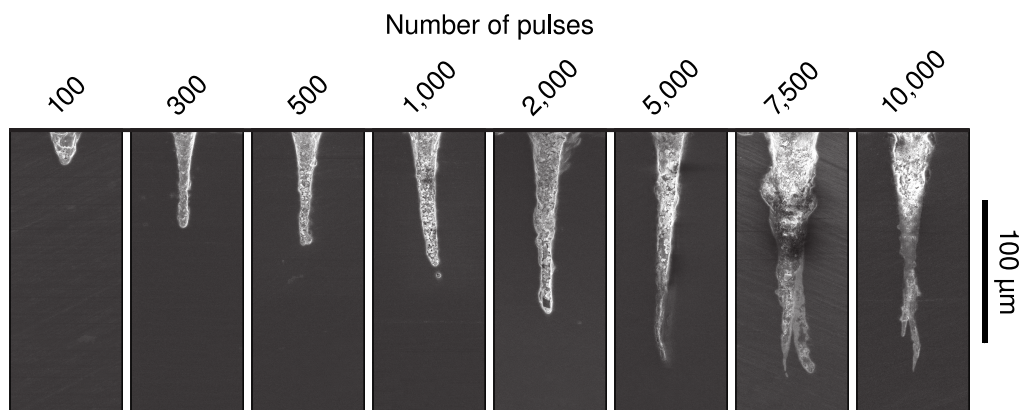
Fig. 4.2: Polished sections of percussion-drilled holes in silicon with ps-pulses at 1030 nm using a fluence of 8 J/cm^2. Compare to the hole silhouette observed by in-situ imaging in fig. 4.1.

4.1.1 Phases of the Drilling Process

A quantitative analysis of the depth development reveals three distinct process phases. Fig. 4.3 shows the representative depth evolution at a fluence of $F = 10\,\mathrm{J/cm^2}$ in comparison to the development of the area of the silhouette, which can be considered as an approximation for the hole volume. For better visualization, the abscissa in fig. 4.3 has a nonlinear scale.

Fig. 4.3: Typical evolution of hole depth (red) and area of the hole silhouette (blue) for percussion drilling in silicon (8 ps pulse duration at a fluence of 10 J/cm^2). Arrows indicate intermediate periods of constant hole depth. The abscissa is scaled non-linearly for better visualization.
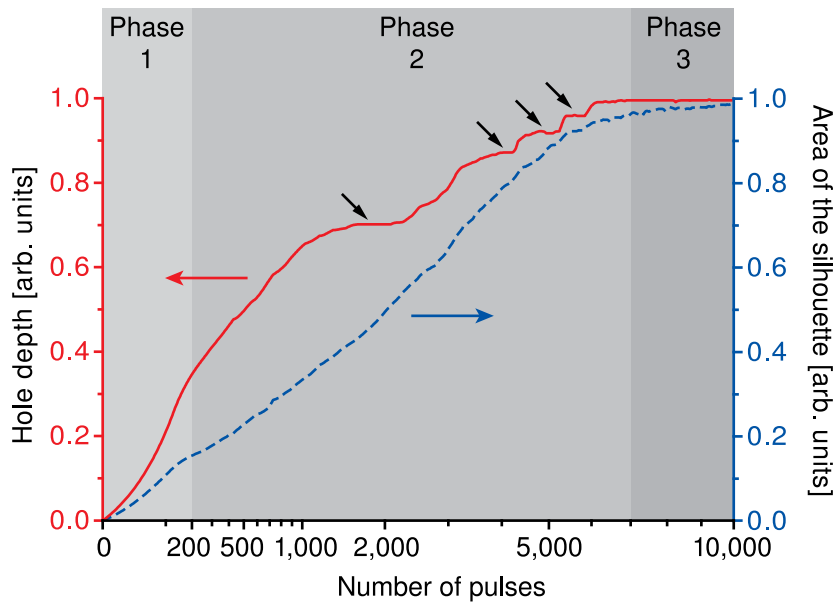
In the first phase, which covers the first 200 pulses, the depth of the hole increases with the highest ablation rate. An evaluation of the hole depth d in dependence of the number of applied pulses N according to the Hirschegg-model with $d \propto N^{\chi}$ (see equation 2.1 in section 2.2) gives a parameter $\chi \approx 1.1$, which means even a slight increase of the ablation rate in this first phase. On-line depth measurements for drilling of stainless steel with hole depths up to 50 μm show a similar increase of the drilling rate [139]. This behavior can be attributed to the so-called incubation effect, which significantly reduces the ablation threshold for irradiation with multiple pulses [95, 110, 140] and accordingly increases the ablation rate. The incubation effect shows a saturation and nearly constant values for the threshold fluence after approximately 100 pulses, which is also in good agreement with the observation here. However, this result differs from in-situ observations of drilling in ceramics with a significant decrease of the ablation rate directly from the beginning of the process [24]. The transition to the next process phase is marked by a significant drop in the ablation rate and therefore a reduced increase in hole depth. At the end of the initial phase, the hole has already reached approximately 30% of its final depth.

In the following second phase, beginning at ca. 200 pulses, the ablation rate gradually reduces, which results in $\chi < 1$ for the period up to 1,000 pulses. For more than 1,000 pulses, plateaus of constant depth can be observed, marked by arrows in fig. 4.3. Simultaneously, the section area increases continuously, nearly without fluctuations. This indicates a predominant transverse growth of the hole capillary, e.g. by the formation of indentations on the sidewalls. After such a stop of depth increase, drilling can resume in forward direction with nearly the same ablation rate as before. Here, a classification according to a χ-value is no longer appropriate due to the fluctuations of the depth development. Intermediate periods without forward drilling have also been observed by inline coherent imaging of drilling in stainless steel [32] and in some cases also for in-situ imaging of ceramics [19, 24].

When the hole reaches its final, maximum depth, the second process phase ends. In the example here, this is the case after approximately 7,000 pulses. In the following third process phase, there is still an increase of the section area by approximately 5%, although the depth remains constant, as shown in fig. 4.3. This increase is mainly induced by a widening of the hole due to sidewall ablation by the wings of the Gaussian beam profile, see also the last step in fig. 4.1. Nevertheless, the formation of additional branches is possible, leading to multiple hole ends, but these branches end above the original tip of the hole.

The behavior described here is characteristic for a deep drilling process and has been observed for all process parameters under investigation in this study. Nevertheless, the absolute values of depth, silhouette size and the number of pulses required to reach a certain process state change according to the laser and processing parameters and moreover, they are subject to statistical variations as described in the following section.

4.1.2 Statistical Variations of the Drilling Process

If laser drilling is repeated under identical conditions, it goes through the characteristic process phases described above. However, the result can differ with respect to the process duration as well as the achieved shape of the hole. Fig. 4.4 shows the depth development of ten holes, all drilled at a fluence of $10\,\mathrm{J/cm^2}$. Examples of the hole shape at the end of the initial process phase, i.e. after ca. 150 pulses, and the final hole shape, after ca. 5,000 pulses, are shown in fig. 4.5.

The initial phase shows nearly the same increase in depth for all holes with a transition to the second process phase at approximately 150 pulses, see inset in fig. 4.4. Also, the hole shape at the end of the first process phase in fig. 4.5 (a) is similar for all examples.
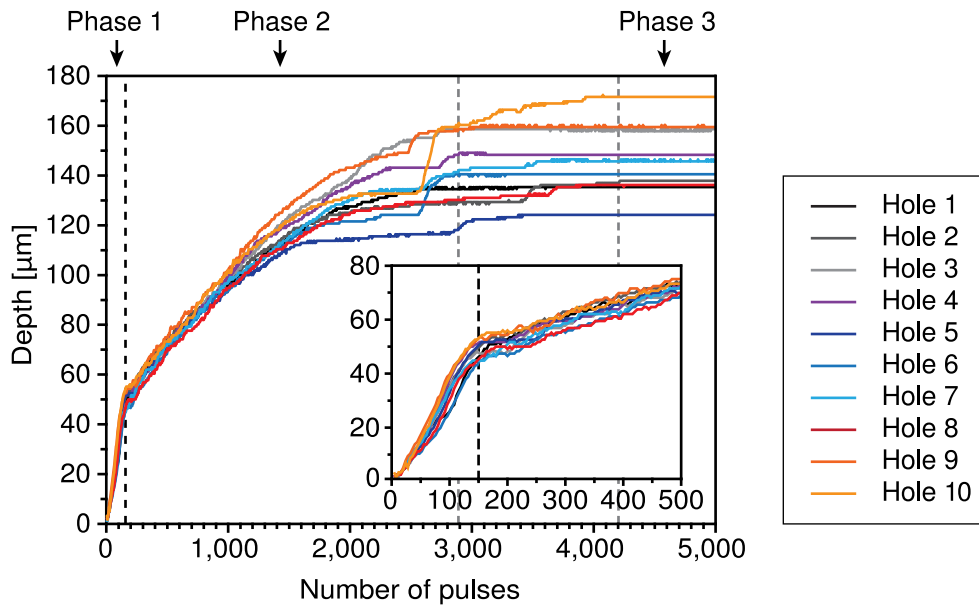
Fig. 4.4: The evolution of the laser drilling is subject to statistical variations, especially in the second process phase. The depth development is plotted for ten repetitions under identical processing conditions, at a pulse duration of 8 ps and a fluence of 10 J/cm^2.

The standard deviation of the hole depth at this instant is ca. 5 µm, which is approximately 10% of the hole depth. The relative standard deviation of the silhouette area is ca. 7%.

Fig. 4.5: Different holes drilled under the same conditions at a fluence of 10 J/cm^2 show a similar shape after 150 pulses (a) but differ significantly at the end of the drilling process after 5,000 pulses (b), especially in their lower parts.

In the second process phase, the general depth development is similar for all holes. They all show a decreasing average drilling rate in combination with intermediate periods of constant depth. These periods can already occur at the beginning of phase 2 with short intervals of several tens of pulses and t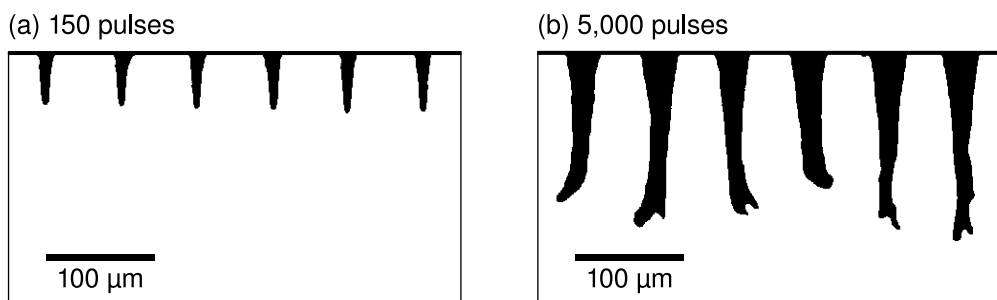hen become more pronounced in the further progress with a possible duration up to several hundred pulses. The actual occurrence and duration of the intermediate stops of forward drilling is different for each individual hole. Therefore, holes which first exhibited a lower depth than others may outperform them during the drilling process if a sufficient depth increase occurs at the right moment. There are several examples of such events visible in fig. 4.4. Regarding the shape evolution, a stop of forward drilling is always connected with predominant ablation in transverse direction which results in the formation of bulges, cavities and occasionally additional branches and capillaries. The absolute size of the silhouette area is not directly correlated with the hole depth, since holes with numerous bulges and branches may have a larger section although they exhibit a lower depth. Nevertheless, ablation in transverse direction is not restricted to periods of constant depth and takes place throughout the complete second drilling phase. Most prominently, this results in a deviation of the drilling direction away from the incident laser and hence a bending of the hole, see also fig. 4.1. Furthermore, the duration of the second process phase also varies statistically. The final depth can be reached already after ca. 2,900 pulses or it can take up to ca. 4,200 pulses.

According to the different development of the holes in the second process phase, there are remarkable differences in the final shape as shown in fig. 4.5 (b). While the upper parts of the holes exhibit a similar taper, the bending in the lower part may occur in every possible direction and with different size. Due to the circular polarization of the drilling laser, no preferred direction of bending is induced, nevertheless it cannot be suppressed. Note, if bending occurs in the line of sight of the imaging system, it is less or even not visible in the silhouette captured by the in-situ imaging technique, see for example the last two specimen in fig. 4.5 (b). Minor changes to the hole shape are also possible in the third process phase which involve an increase in the diameter of the hole, especially in the upper part and occasionally the formation of additional branches or the enlargement of existing cavities. The standard deviation of the depth at the end of the drilling process is ca. 15 µm, a relative value of 10%. The silhouette area also shows a relative standard deviation of 10% for the final hole shape. Although these quantities are

comparable to the first process phase, the process duration and final shape of the hole are significantly affected by the statistical variations of the drilling process in the second process phase. In contrast, the first phase of the drilling process shows a deterministic duration and highly reproducible hole shape which is largely predefined by the incident laser beam profile. This general behavior has to be considered when designing a process strategy for applications. In this regard, the shape formation in the second process phase, in particular the deviations from the ideal hole, is of special interest. Different ways of shape evolution have been observed. The most prominent ones are arranged in fig. 4.6 for comparison. Each case shows an enlarged region of interest for different holes, all drilled under identical conditions, here at a fluence of $10\,\mathrm{J/cm^2}$ and a pulse duration of 8 ps (FWHM).

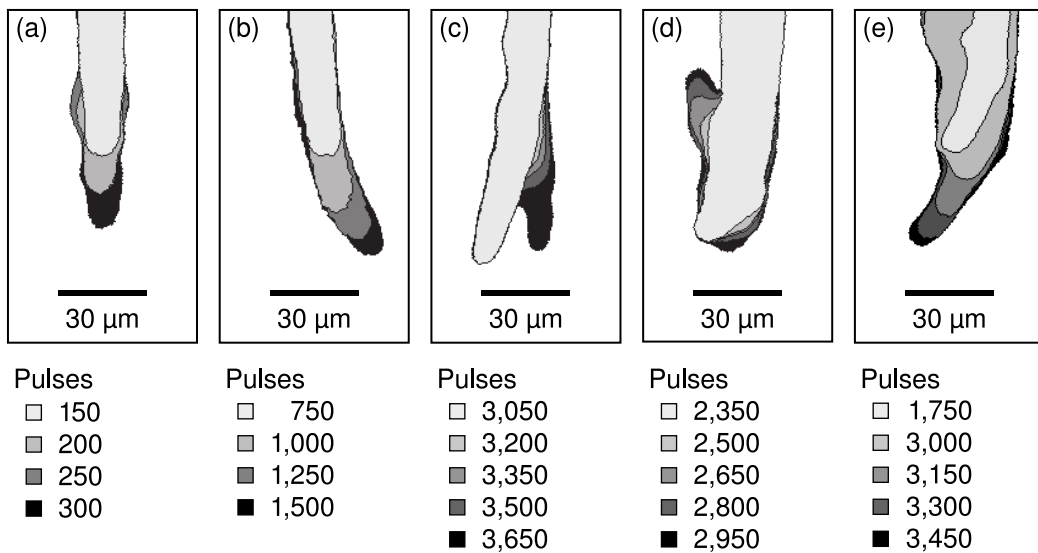| (a)	(b)	(c)	(d)	(e)
30 μm	30 μm	30 μm	30 μm	30 μm
Pulses	Pulses	Pulses	Pulses	Pulses
☐ 150	☐ 750	☐ 3,050	☐ 2,350	☐ 1,750
☐ 200	☐ 1,000	☐ 3,200	☐ 2,500	☐ 3,000
☐ 250	☐ 1,250	☐ 3,350	☐ 2,650	☐ 3,150
■ 300	■ 1,500	☐ 3,500	☐ 2,800	☐ 3,300
		■ 3,650	■ 2,950	■ 3,450

Fig. 4.6: Different developments of the hole shape in the second drilling phase. These examples show details of the most prominent phenomena like bulging (a), bending (b), formation of an additional branch (c), ablation in upward direction (d) and resume of forward drilling (e).

Fig. 4.6 (a) shows the formation of a bulge at the beginning of the second process phase. From 150 to 200 pulses, the tip of the hole penetrates further into the depth and in addition bulging occurs on the left side of the hole approximately 15 μm above the hole tip. During the next 50 pulses, the size of the bulge increases significantly. In addition bulging also occurs in the opposite direction. Meanwhile, there is a complete stop of forward drilling and also the shape of the hole tip stays the same. The period of predominant transverse ablation is limited to 50 pulses. Between 250 and 300 pulses,

drilling resumes in forward direction and no further enlargement of the bulge can be observed. Remarkably, the formation of the bulge does not occur directly at the deepest point of the hole together with the advance of the hole tip, but along the sidewalls in a region above the main ablation front.

The evolution of the hole bending is also a gradual process as shown in fig. 4.6 (b). Starting from a marginal inclination at 750 pulses, the change of the drilling direction increases from pulse to pulse which leads to a growing displacement of the hole tip with respect to the main axis of the capillary. This behavior indicates a self-enhancing process, the existing displacement changes the position of the ablation front in a way that further increases the inclination or displacement for the next pulse. Along with the increasing displacement, the ablation rate decreases and eventually drilling stops completely after approximately 1,500 pulses. The final displacement reaches ca. 15 µm which is comparable to the diameter of the capillary in the lower part of the hole.

After the formation of a hole bend, there is typically a period without further ablation in forward direction. During this period, ablation still takes place along the sidewalls and reshapes the hole until drilling can resume in the same or even a different direction. This situation is shown in fig. 4.6 (c). A hole bend to the left is completely formed after 3,050 pulses. During the next 500 pulses, no further forward drilling occurs at the tip of the hole. In contrast, the right sidewall of the bend is continuously reshaped. This takes place in the upper region of the bend where the reshaped part of the sidewall is directly below the main axis of the hole capillary. Therefore, it can be assumed that a large part of the pulse propagating through the hole capillary is incident on this part of the sidewall. The sidewall is straightened and a flat bottom is formed in this region. From 3,500 to 3,650 pulses, drilling resumes in the direction of the hole axis with a significantly increased ablation rate. A second hole end with a depth of approximately 10 µm is formed during 150 pulses. Meanwhile, no ablation takes place at the previously excavated hole tip.

In combination with the reshaping of the hole after the bending, ablation may also occur in upward direction, opposing the incident beam, as shown in fig. 4.6 (d). In this case a hole bending to the left was formed and reshaping already partially took place after 2,350 pulses. After 2,500 pulses a bulge is formed on the left side of the hole. In the following, ablation predominantly occurs at the top of this bulge which consequently grows in upward direction. In addition, straightening of the sidewall on

the right continues during this time and the bottom of the hole is flattened which may lead to a resume of forward drilling.

A situation when forward drilling is resumed and results in an increase of the achieved depth is shown in fig. 4.6 (e). Here, a bending of the hole occurred at 1,750 pulses. From this point to approximately 3,000 pulses, a longer period of constant depth can be observed, typical for the later part of the second process phase when the hole is already approaching its maximum depth. Nevertheless, the hole shape changes completely during this period. The sidewalls are straightened in combination with a significant increase of the hole diameter. In the following, ablation occurs again at the bottom of the hole. A new tip is formed and advances further into the depth while ablation only marginally takes places at the rest of the hole. During 450 pulses, the hole depth is increased by ca. 20 μm. The deepening directly forms another bending in the same manner as shown in fig. 4.6 (b) with a gradual increase of the inclination and misplacement together with a reduction of the drilling rate until forward drilling stops again after ca. 3,450 pulses. At this point, the final hole depth may be reached or the process of reshaping the hole may be repeated until drilling can resume again.

The examples in fig. 4.6 (c)-(d) illustrate how ablation takes place during periods without forward drilling. Ablation of the sidewalls can reshape the hole capillary due to the formation of bulges, a general increase of the hole diameter and straightening of the hole walls in combination with the formation of a flat hole bottom. Eventually, this can result in a higher amount of pulse energy on the hole bottom and better energy coupling to the material, e.g. by a reduced irradiated area on a flat bottom and a consequently higher local fluence. Then, ablation can resume in this direction at a high rate. Although there is a continuous increase of the hole silhouette due to this reshaping of the hole, see also fig. 4.3, the evolution of the hole silhouette can also show significant fluctuations, though. The reshaping process is usually connected to low ablation on the sidewalls and therefore only a slight increase of the hole silhouette. However, the resume of drilling can lead to a considerable growth of the hole, especially during the formation of additional branches, see for example fig. 4.6 (c).

4.2 Influence of the Process Parameters

The study of the drilling behavior shows in general the same principal characteristics and process phases for all conditions that are under investigation here. However, the processing parameters can significantly influence the actual outcome of the drilling, especially in terms of process duration, achievable depth and shape of the hole. The following sections cover a systematic investigation of the effect of processing parameters like applied fluence and focus position, as well as laser parameters like pulse energy, pulse duration and wavelength on the hole shape evolution.

4.2.1 Fluence and Pulse Energy

For laser ablation, the applied fluence is a fundamental process parameter, which specifies the actual ablation mechanisms together with the pulse duration, see chapter 1. Especially important from an application oriented point of view, it defines the ablation rate and hence the processing speed [5, 15, 55]. In the following, the term fluence is consistently used for the incident pulse energy per laser spot area in the focus. Therefore, the fluence can be adapted either by a variation of the pulse energy or by changing the focal spot size, e.g. with lenses of different focal length. The range of fluence investigated in this study covers the typical range for ultrashort pulse machining from $1\,\text{J/cm}^2$ to $150\,\text{J/cm}^2$. Table 4.1 summarizes the lens parameters used in the experiments, the corresponding spot diameter in the focus d_{focus} and the maximum achievable fluence F_{max}. The spot size was measured with the method of Liu [133].

Tab. 4.1: Measured spot size and maximum achievable fluence for a maximum pulse energy of 125 µJ at 1030 nm for the lens configurations used in the experiments of this study.

Lens	d_{focus} [µm]	F_{max} [J/cm^2]
f = 25 mm	10.4 ± 0.5	294 ± 26
f = 50 mm	15.6 ± 0.3	130 ± 6
f = 75 mm	20.4 ± 0.7	76 ± 5
f = 100 mm	27.8 ± 0.3	41 ± 1
f = 150 mm	37.8 ± 0.6	22 ± 1

First, the influence of the fluence on the final hole is under investigation. Fig. 4.7 (a) shows a quantitative analysis of the final hole depth for different lens configurations.
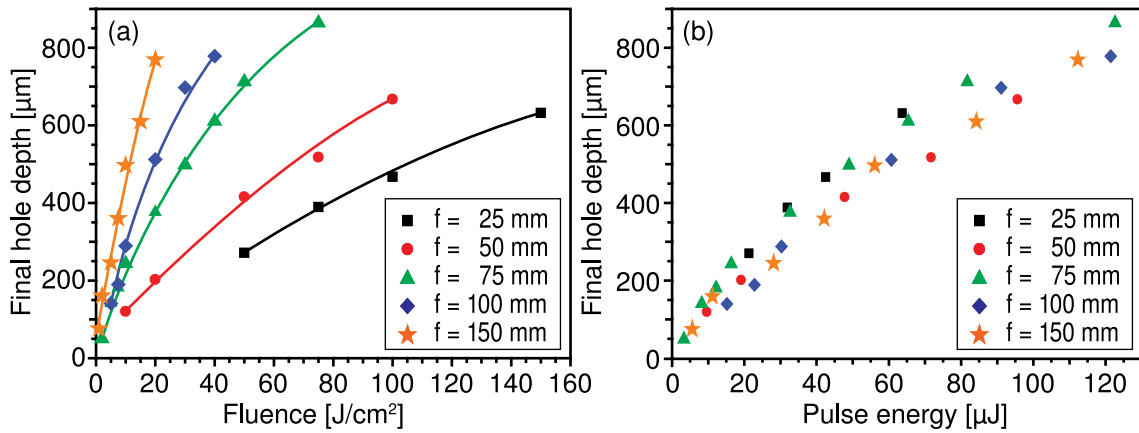

Fig. 4.7: The final depth of the hole increases with the applied fluence, in strong dependence on the focal length in use (a). The lines are a guide to the eye, only. In dependence on the pulse energy, the final hole depth increases largely independent of the focusing conditions (b).

For each lens configuration, the final hole depth increases with increasing fluence, as expected. Remarkably, this increase depends on the actual focal length f, with the steepest slope for the largest focal length. For example, a comparison of the maximum achievable hole depth at a fluence of $20 \, \text{J/cm}^2$ shows ca. $200 \, \mu\text{m}$ at $f = 50 \, \text{mm}$ and approximately a four times increase to ca. $780 \, \mu\text{m}$ at $f = 150 \, \text{mm}$. In contrast, the final hole depth in dependence of the pulse energy is largely independent of the lens and corresponding spot size, as shown in fig. 4.7 (b). Therefore, the pulse energy is the fundamental parameter with respect to the final hole depth. This means, the hole depth is also independent of the actual Rayleigh-length z_R. For the lens with $f = 25 \, \text{mm}$, the Rayleigh-length is ca. $80 \, \mu\text{m}$ and clearly exceeded by hole depths up to $600 \, \mu\text{m}$. On the other hand, $z_R \approx 1{,}100 \, \mu\text{m}$ in case of $f = 150 \, \text{mm}$ but the final hole depth only reaches ca. $800 \, \mu\text{m}$ for the available maximum pulse energy. The large range of the final depths for a certain pulse energy can be attributed to the statistics of the drilling process and according variation of the depth evolution, especially in the second process phase, as discussed in section 4.1.2. In addition, a saturation of the increase of the final depth with respect to the pulse energy can be observed in fig. 4.7 (b). This is an indication that for holes with very large depth a lower amount of the incident pulse energy can effectively contribute to ablation at the hole bottom. The reasons for this behavior are studied in chapter 5, p. 67ff.

In the following, the influence of the pulse energy on the hole shape evolution is investigated for one specific focusing condition. Here, a focal spot size of ca. 28 μm is realized with a lens of 100 mm focal length. In this case, the applied fluence is directly dependent on the pulse energy. Fig. 4.8 shows different stages of the hole shape evolution from 200 pulses to 15,000 pulses at different pulse energies but for identical focusing conditions.
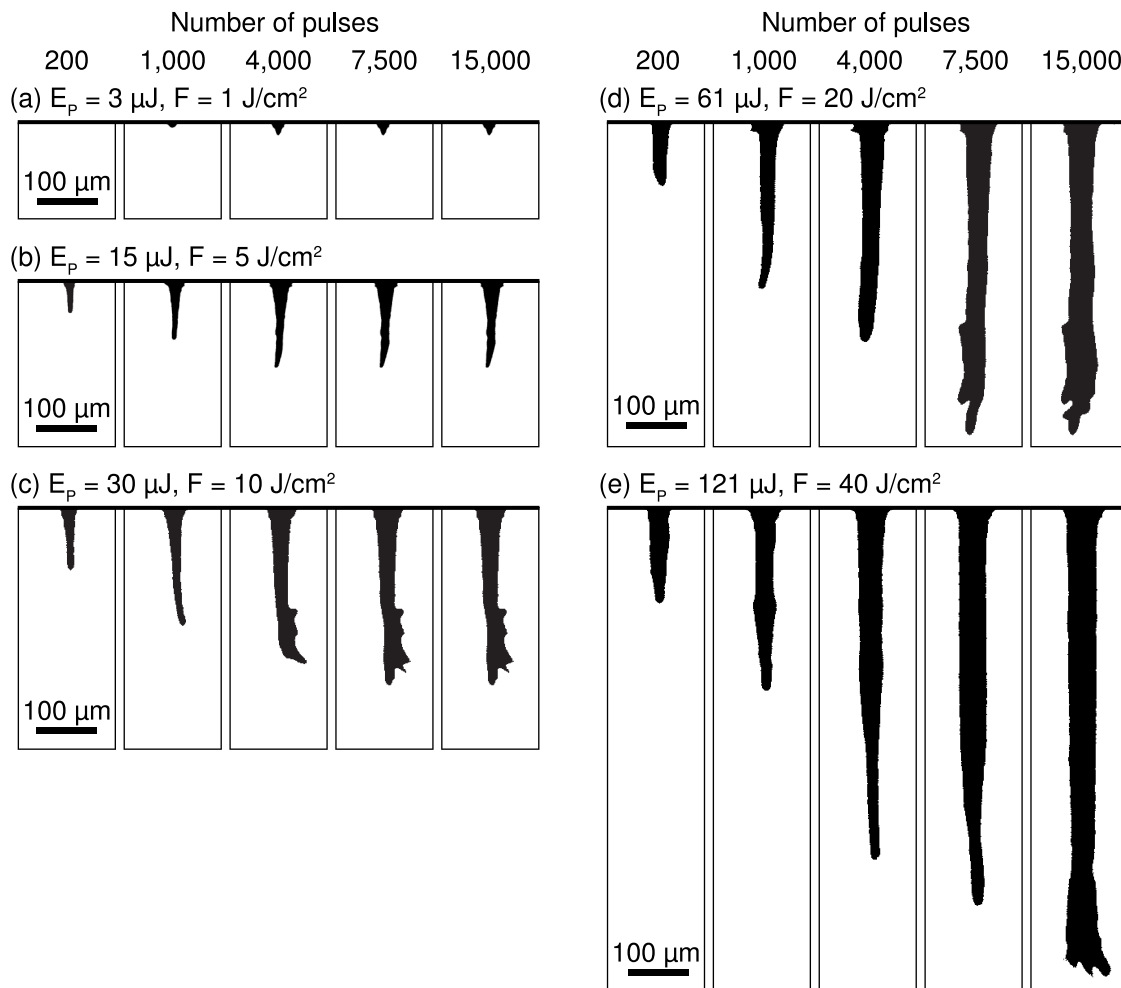
Fig. 4.8: The applied pulse energy influences the hole shape formation, e.g. with less characteristic hole taper, indentations and branching for higher pulse energies.

The first case in fig. 4.8 (a) shows ablation with a low pulse energy of 3 μJ. The corresponding fluence of $1\,\mathrm{J/cm^2}$ is approximately four times higher than the ablation threshold. Ablation takes place in the low fluence regime and only a low ablation rate, in the order of 10 nm/pulse, is achieved. No hole capillary is formed, since excavation already stops after the formation of a conical crater on the surface with a depth of

ca. 20 μm. The stop of ablation can be attributed to the increase in effective surface area, which eventually reduces the effective fluence down to the ablation threshold. In this case, there is no deep drilling and the characteristic process phases cannot be distinguished. This example is shown for completeness only, while in the following deep drilling with significant depth and aspect ratio is under investigation.

For a pulse energy of 15 μJ and corresponding fluence of 5 J/cm^2, shown in fig. 4.8 (b), the typical behavior of depth evolution can be recognized. During the first process phase, the initial hole capillary with a tapered geometry due to the Gaussian beam profile is formed. A similarity to the conical cavity at the surface for a low pulse energy is still present in form of the funnel shaped entrance. After 1,000 pulses, already a slight deviation in the drilling direction can be observed. This bending grows till the stop of forward drilling at ca. 4,000 pulses. Afterwards, only a minor increase of the hole diameter and ablation at the bending can be observed.

For the example with a pulse energy of 30 μJ (fluence of 10 J/cm^2) in fig. 4.8 (c), the first phase is equivalent to a pulse energy of 15 μJ with a similar shape of the initial capillary, nevertheless with increased size and depth. Bending of the hole also begins after ca. 1,000 pulses. Ablation in transverse direction during the period of 1,000 to 4,000 pulses leads to the formation of additional branches or large indentations in the lower part of the hole. Here, ablation is also not limited to the hole bottom, but also takes place in the region above. Due to the higher pulse energy in comparison to fig. 4.8 (b), the reshaping of the hole after the formation of the bending results in further forward drilling, see the period of 4,000 to 7,500 pulses. After 7,500 pulses, no significant change in the hole shape can be observed. At the end, the complete lower half of the hole is affected by branches and indentations, which is not the case for a lower pulse energy and accordingly lower hole depth.

The principal drilling behavior at a pulse energy of 60 μJ (fluence of 20 J/cm^2), see fig. 4.8 (d), again shows the typical characteristics of deep drilling. The excavation of the initial capillary also occurs in the first 200 pulses. In the following second process phase, bending of the hole is observable after 1,000 pulses. Additional branches and large indentations occur in the period of 4,000 to 7,500 pulses. Forward drilling finally stops at ca. 7,500 pulses. The hole shape still undergoes changes in the third process phase, especially in the lower part of the hole. At this pulse energy, only the lower third of the hole is affected by imperfections, while the upper part looks almost cylindrical.

Finally, drilling at a pulse energy of 121 μJ (fluence of 40 J/cm^2) shows the lowest variation of the hole shape and hole diameter, see fig. 4.8 (e). The bending of the hole is least distinct and only observable after 4,000 pulses. The second phase of the drilling process now extends to 15,000 pulses and leads to the formation of multiple ends, which have nearly the same maximum depth. Only the lowest part of the final hole (20% of the depth) is affected by imperfections, while the upper part is almost cylindrical and shows only a low taper. This can be attributed to the erosion of the sidewalls, especially in the later drilling process, which transforms former imperfections, like the indentations in the middle of the hole after 1,000 pulses, until a constant hole diameter is achieved. This process also reduces the hole taper and the funnel shape at the entrance and leads to a nearly cylindrical hole shape. However, the hole diameter is significantly increased in comparison to drilling at lower pulse energies, e.g. 30 μJ.

4.2.2 Focus Position

The position of the laser focus with respect to the sample surface is a critical process parameter that directly influences the irradiated area due to the change of the spot size according to the beam caustic. This affects the entrance diameter of the hole [2] as well as the hole taper [26]. In the following experiments, drilling is performed with a lens of 100 mm focal length at different focus positions above and below the surface in the range ± 3 times the Rayleigh length z_R (with $z_R \approx 600$ μm here). Nevertheless, the focus position is kept constant during the entire drilling duration. Fig. 4.9 shows the shape of the initial hole and the final hole shape for a low pulse energy ($E_P = 30$ μJ) and a high pulse energy ($E_P = 125$ μJ) in comparison.

The alignment of the focus has an immediate effect on the drilling depth. Already at the end of the first drilling phase a significant difference of the drilling depth can be observed, see top row of fig. 4.9. For strong defocusing, for example $z \geq +2z_R$, only a shallow structure of a few tens of microns or even less is ablated due to the decrease in fluence at the sample surface. On the other hand, focusing to the surface ($z = 0$) or below ($z = -z_R$) generates holes with depths up to 150 μm (at 125 μJ) and a corresponding aspect ratio up to 5:1. Remarkably, for both pulse energies, the optimum position for the focus to realize the largest depth after the initial process phase is approximately one Rayleigh-length below the surface at $z = -z_R$. In comparison to a focus position at $z = 0$, an 80% larger depth can be achieved at a pulse energy of 30 μJ and still a 40% increase
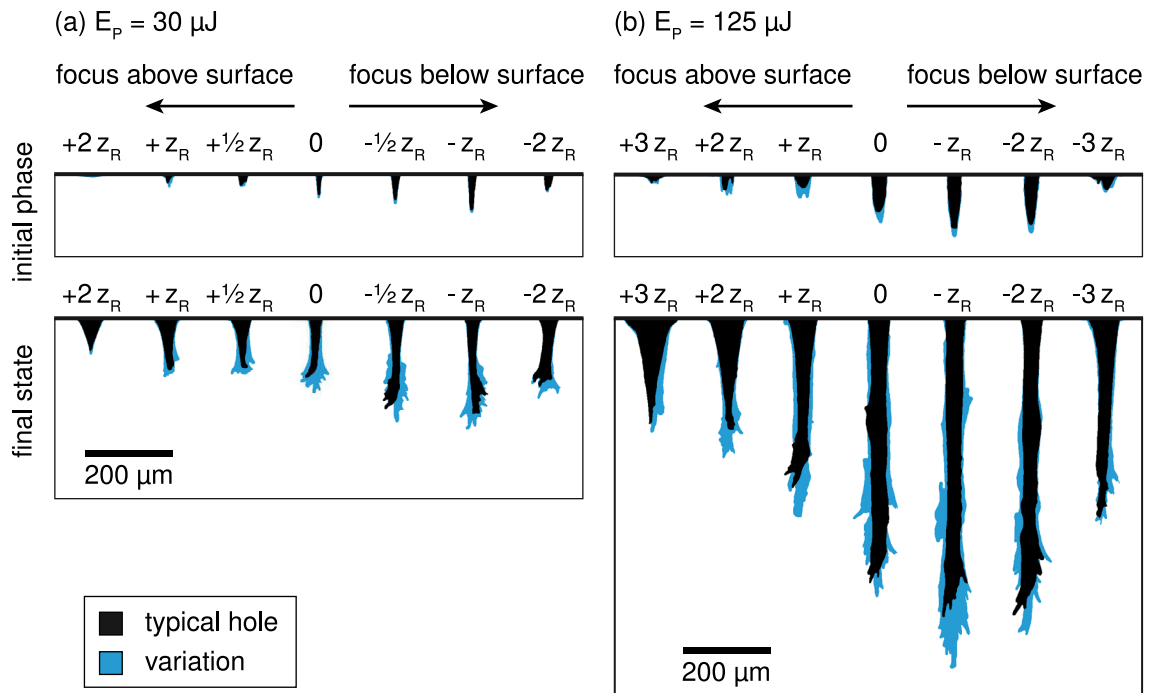
Fig. 4.9: The hole shape of percussion drilling varies according to the focus position z with respect to the sample surface at $z = 0$. For a pulse energy of 30 µJ (a) and 125 µJ (b), the top row shows the shape after the initial phase (ca. 150 pulses) and the bottom row the final state in each case. A typical hole is shown in black and variations of the shape for ten different holes are shown in blue in the background. The Rayleigh length in this example is $z_R \approx 600$ µm.

at 125 µJ is obtained for focusing at $z = -z_R$. This is in agreement with the observed increase of the ablation rate for an optimized focus position below the surface in drilling of stainless steel with microsecond pulses [2].

A minor shift of the focus above the surface to $z = +z_R$ decreases the obtained hole depth by ca. 50%. The variation of the hole shape (blue shapes in fig. 4.9) after the first process phase is comparably low near the optimum focus position. For stronger defocusing, those variations become more significant, see for example $z = +2z_R$ at $E_P = 125$ µJ. The duration of the first process phase is only marginally affected by the focus position and takes approximately 150 pulses in all cases. However, for strong defocusing, the individual process phases cannot be distinguished. In this case, only a gradual decrease of the ablation rate can be observed without the aforementioned features of deep drilling.

The final hole shape also differs significantly according to the focus position, as shown in the bottom row of fig. 4.9. Here, the largest depth is reached for an optimum focus position at $z = -z_R$ below the surface in case of both pulse energies, similar to the initial process phase. Compared to the focus at $z = 0$, a 60% increase of the hole depth is observed for $E_P = 30\,\mu J$ and a 30% increase for $E_P = 125\,\mu J$, which is a significant effect, although less pronounced than for the initial drilling phase. Defocusing above the surface to $z = +z_R$ reaches only 80% of the hole depth compared to $z = 0$. Recent investigations of ultrashort pulse drilling with fs-pulses under focusing with high numerical aperture also observed a maximum drilling rate and final depth for convergent defocusing, i.e. a focus position below the sample surface [141].

In addition, the reproducibility of the hole depth improves at the optimized focus position to a standard deviation of 6% or less in the final state and only 3% after the first drilling phase in comparison to about 10% for focusing at the surface. However, the shape of the holes for all focus positions in the range of $z = +z_R$ to $z = -2z_R$ is dominated by the formation of indentations and additional branches, especially in the lower part of the hole. These branches can occur randomly in every direction and their formation is different for each individual hole, as illustrated by the variation of the hole shape in fig. 4.9. For larger shifts of the focus position away from the optimum, e.g. to $z = +2z_R$ or $z = +3z_R$, the extent of the shape deviations in the final state is diminished, nevertheless in combination with a significantly reduced depth and increased entrance diameter and hole taper. As an extreme example, only a conical cavity is formed for a focus at $z = +2z_R$ and a pulse energy of $30\,\mu J$, but no deep drilling with high aspect ratio is achieved. The same applies to $E_P = 125\,\mu J$ although at a larger focus shift due to the higher pulse energy, see $z = +3z_R$ in this case.

The enhancement effect of the focus position to the drilling efficiency and achievable maximum depth can be attributed to an adaption of the pulse propagation to the hole shape, especially in the upper part of the hole. This is illustrated in fig. 4.10 by the superposition of the beam geometry with the final hole shape for different focus positions at a pulse energy of $E_P = 125\,\mu J$. The red area encloses the $1/e^2$-diameter of an ideal Gaussian beam, which contains about 86% of the total intensity. The beam parameters are adapted to the experimental focusing conditions. In case of focusing at the optimum position at $z = -z_R$, the convergent beam matches the hole geometry with decreasing diameter in the funnel shaped entrance and adjacent taper of the hole.
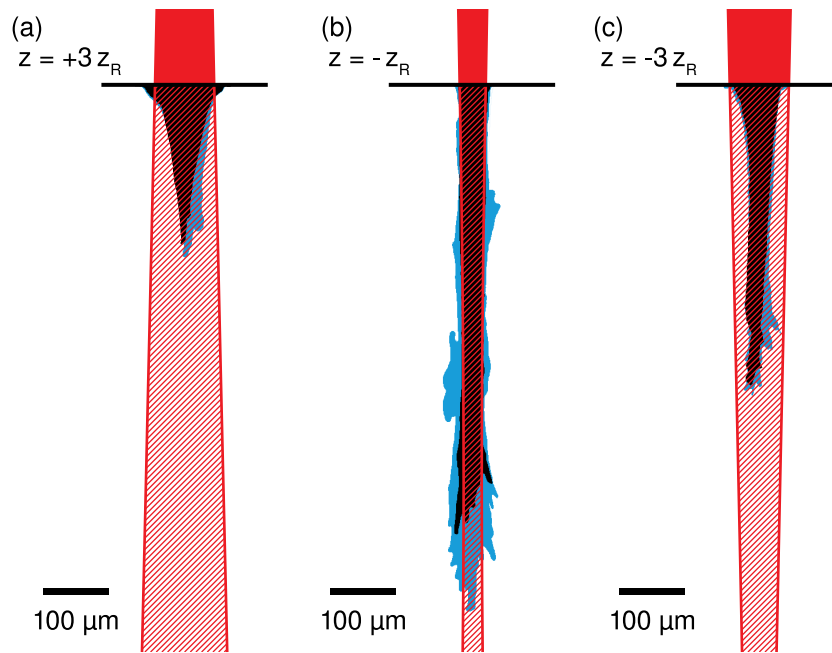
Fig. 4.10: The propagation of incident laser pulses can be approximated by the caustic of a Gaussian beam, shown in red, for different focus positions - above the surface (a), the optimum position for drilling (b) and below the optimum position (c). In case of the optimum position at $z = -z_R$, the beam caustic is adapted to the final shape of the hole, illustrated by the silhouette of a typical hole in black and the variation of 10 equal holes in blue in the background, here for a pulse energy of 125 μJ. The Rayleigh length in this example is $z_R \approx 600$ μm.

Nevertheless, focusing too far below the surface overcompensates this positive effect. Due to the lower fluence on the surface at the beginning of the drilling process, the hole shape does not reach a sufficient entrance diameter and taper to benefit from the strongly convergent beam, see fig. 4.10 (c). Focusing above the surface, is not adapted at all to the evolving hole shape, since the beam is divergent inside the capillary. Consequently, such an arrangement only leads to a significant increase of the entrance diameter connected with a steep taper, which results in a stop of ablation already at a shallow depth, see for example $z = +3z_R$ in fig. 4.10 (a). This approach has been developed into a quantitative model of the drilling rate for tight focusing conditions, recently [141], however, with no regard to the actual hole shape.

In summary, an optimum position of the focus can significantly enhance the achievable hole depth and drilling efficiency, especially in the initial process phase. Therefore, this processing parameter has to be carefully optimized in application.

4.2.3 Wavelength

The wavelength of the drilling laser affects the drilling process in two ways. On the one hand, it directly influences the absorption of the laser pulse and on the other hand changes the focusing properties. In the following, the frequency-doubled radiation of the laser is used at a wavelength of 515 nm. The wavelength conversion of the drilling laser is realized by an additional setup for second harmonic generation in a β-barium borate crystal due to its high effective conversion coefficient and damage threshold. At a pulse duration of 8 ps a conversion efficiency of ca. 50% is achieved, which results in a maximum pulse energy of approximately 60 μJ at 515 nm. At this wavelength, the linear absorption coefficient of silicon is three orders of magnitude larger than at the fundamental wavelength of 1030 nm [129]. Hence, the optical penetration depth due to linear absorption is already in the submicron range. Fig. 4.11 shows a simulation of the intensity distribution within the sample I_{sample} and the corresponding lattice temperature T_{lat} according to the Two-Temperature-Model, see equation 1.1. For a detailed description see appendix B, p. 103ff.

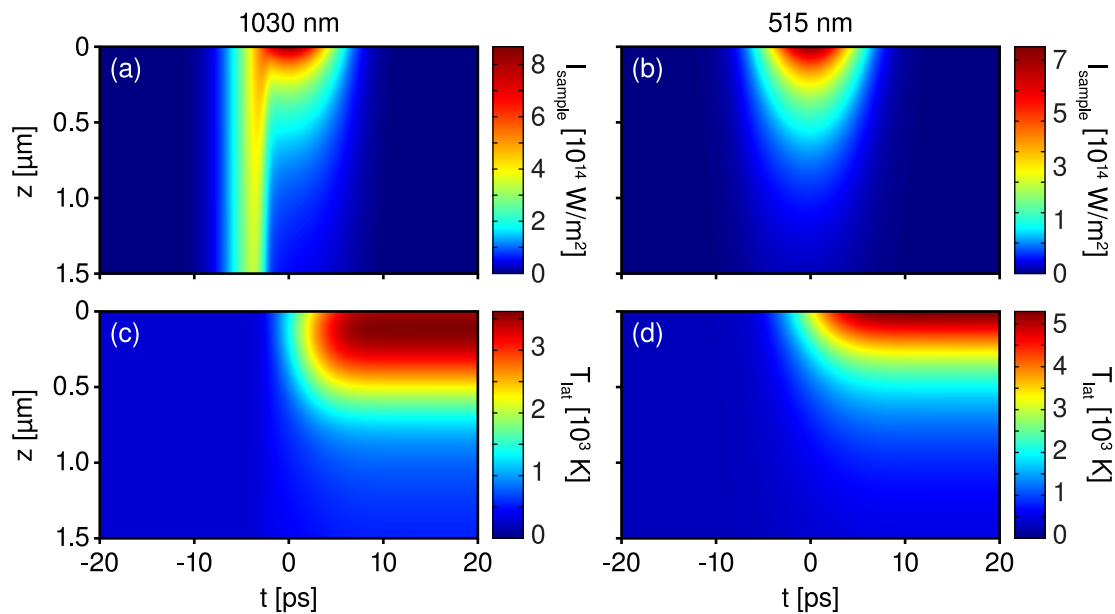**Fig. 4.11:** Simulation of the ultrashort pulse absorption in silicon at 1030 nm and 515 nm for a pulse with a fluence of F = 1 J/cm^2 and 8 ps duration (FWHM). The intensity distribution inside the sample leads to a corresponding increase of the lattice temperature according to the Two-Temperature-Model.

In contrast to 1030 nm, where the pulse initially penetrates deep into the material until the generation of free electrons significantly increases absorption, high absorption takes place from the beginning of the pulse at 515 nm. The increase of the lattice temperature at 515 nm is therefore confined within a thinner surface layer compared to 1030 nm and also reaches a higher maximum value. Consequently, ablation is enhanced at 515 nm and further approaches a metal-like behavior. In the experiment, this results in a decrease of the ablation threshold from $F_{th} = (0.26 \pm 0.06)\,\mathrm{J/cm^2}$ at 1030 nm to $F_{th} = (0.10 \pm 0.02)\,\mathrm{J/cm^2}$ at 515 nm.

In addition, the focusing properties change according to the wavelength. For focusing with low numerical aperture as typical for most micromachining applications, the focal spot size d_{focus} can by estimated by [2]

$$d_{focus} = 4\frac{\lambda}{\pi}\frac{f}{d_{beam}}M^2, \tag{4.1}$$

where λ denotes the laser wavelength, d_{beam} the beam diameter in front of the lens with focal length f, and M^2 denotes the beam quality parameter. In the experiment here, the beam diameter is unchanged after frequency conversion. The beam quality changes from $M^2 \approx 1.1$ at 1030 nm to $M^2 \approx 1.4$ at 515 nm. Nevertheless, the frequency-doubled radiation allows for tighter focusing while still using the same lens and hence the same working distance, which can be an important consideration for applications.

Fig. 4.12 shows a comparison of the shape evolution of two typical holes at 515 nm and 1030 nm, respectively, using the same fluence of $10\,\mathrm{J/cm^2}$ in each case. The focus is situated at the sample surface and a lens with a focal length of 100 mm is used at both wavelengths. The spot size in the focus is reduced from ca. 27 µm at 1030 nm to ca. 19 µm at 515 nm. Consequently, a pulse energy of 14 µJ is sufficient to reach the fluence of $10\,\mathrm{J/cm^2}$ at 515 nm while ca. 30 µJ are required at 1030 nm. The general evolution of the hole shape as depicted in fig. 4.12 is comparable for both wavelengths. During the first 200 pulses, a straight growth of the hole can be observed at a high ablation rate of ca. 0.5 µm per pulse. At the end of this initial phase, approximately 30% of the final depth are reached in both cases. Afterwards, in the second process phase, the drilling rate drops significantly and the hole after 300 pulses is only marginally deeper compared to the situation after 200 pulses. In case of 1030 nm, forward drilling even stopped completely in this period. The further evolution of the hole shape shows the
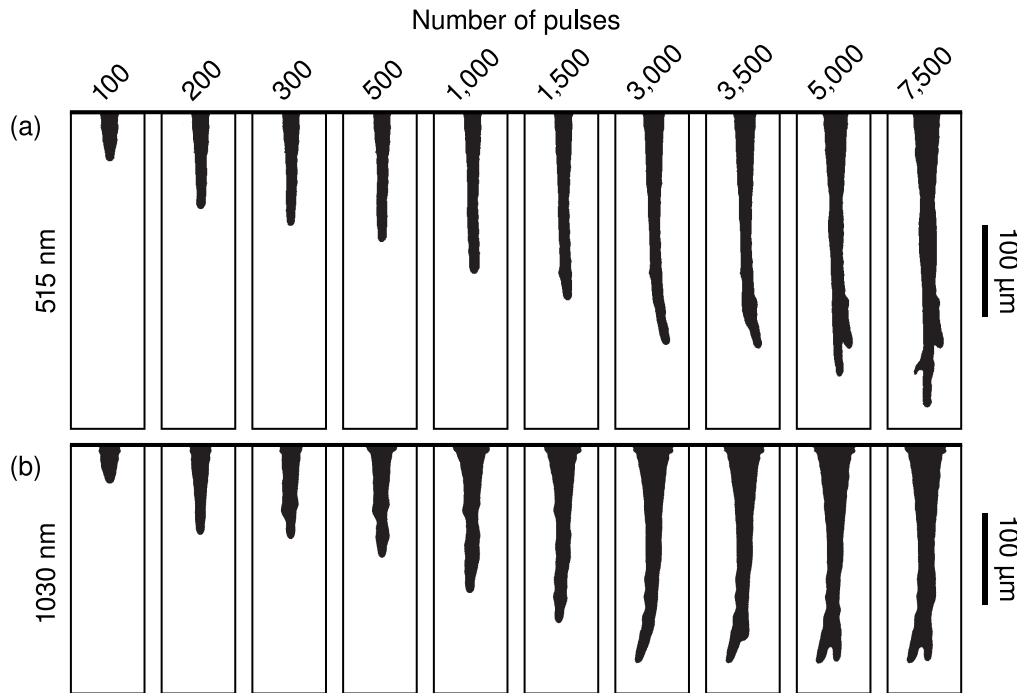
Fig. 4.12: The general hole shape evolution is similar at a wavelength of 515 nm (a) and 1030 nm (b) for holes drilled at the same fluence of 10 J/cm². However, there are significant differences in the details, especially the formation of bulges, hole taper and achievable depth.

formation of indentations and cavities along the sidewalls and bending of the hole. The hole bending gradually develops between 1,500 and 3,000 pulses for both wavelengths. Forward drilling then stops in both cases for about 500 pulses. Meanwhile, the region at the bend is reshaped in both cases similar to the case studies in fig. 4.6 (c)–(e). Eventually, forward drilling resumes and leads to the formation of multiple branches. Also similar for both wavelengths, forward drilling finally stops between 5,000 and 7,500 pulses.

Despite the general similarities, distinct differences can be observed in the details of the shape evolution. Bulges and indentations on the sidewalls occur less often for 515 nm compared to 1030 nm. Especially after 1,000 pulses, the hole drilled at 515 nm shows nearly no deviations from the expected shape, while large indentations and cavities are visible at 1030 nm. The entrance diameter as well as the taper of the hole is significantly reduced at 515 nm, especially after more than 300 pulses. This can be attributed to the tighter focusing and less beam divergence for the lower wavelength. The maximum achieved depth is comparable for both wavelengths, although a considerably lower pulse energy is used at 515 nm.

A quantitative analysis of the depth evolution at a wavelength of 515 nm is shown in fig. 4.13 for ten holes drilled under identical conditions. In this investigation, a pulse energy of 25 μJ is focused on the sample surface with a lens of 100 mm focal length, comparable to the investigation at 1030 nm as shown in fig. 4.4 on p. 38. The smaller focal spot size at 515 nm increases the fluence at the sample surface from ca. $10 \, \mathrm{J/cm^2}$ at 1030 nm to ca. $18 \, \mathrm{J/cm^2}$ at 515 nm.
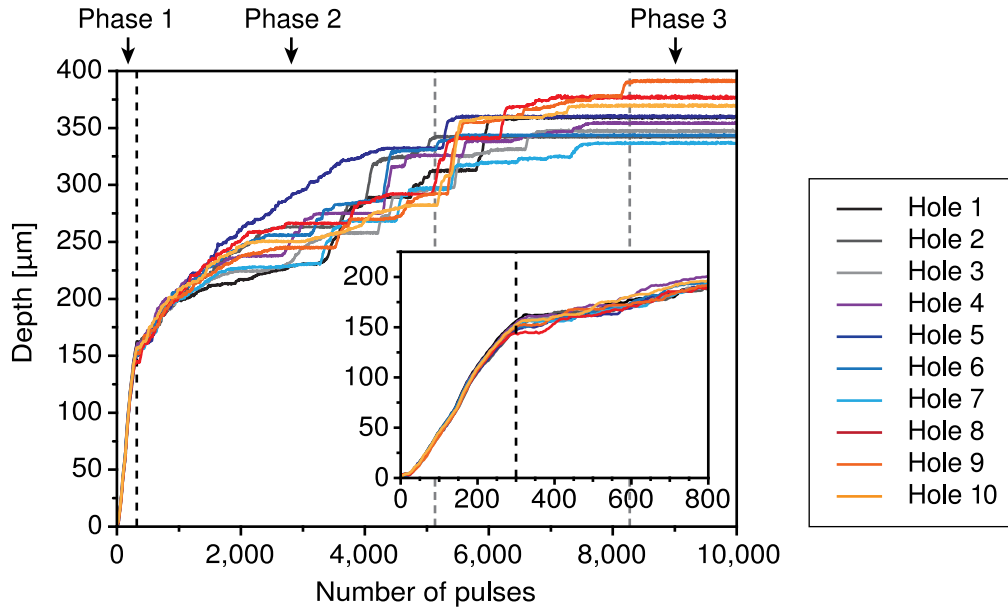

Fig. 4.13: Hole depth evolution for ten holes drilled under identical conditions at a wavelength of 515 nm with a pulse energy of 25 μJ. The increase of the hole depth is continuous and reproducible in phase 1 but is subject to fluctuations which vary for every hole in phase 2.

The three charactersitic process phases can be clearly distinguished in exactly the same manner as for 1030 nm. The first process phase lasts for ca. 300 pulses and ends with an abrupt decrease in the drilling rate, see insert in fig. 4.13. An increase of the ablation rate during the initial phase similar to the situation at 1030 nm can be observed for all drilling runs. The depth development is very reproducible during the initial phase with an average value of ca. 150 μm and a relative standard deviation of only 2.4% after 300 pulses.

During the following second process phase, the average drilling rate continuously decreases and the typical stepwise increase of the hole depth with intermediate periods of constant depth can be observed. The variation of the depth development is similar to the situation at 1030 nm. The transition to the third process phase and the final

stop of drilling can vary between ca. 5,000 and 8,000 pulses. According to the different shape evolution for each hole, the final depth ranges between 340 μm and 390 μm with a relative standard deviation of ca. 5%. A comparably low value to drilling at 1030 nm under similar parameters, which typically yields ca. 10%, see section 4.1.2.

The final hole depth at 515 nm is primarily dependent on the pulse energy and largely independent of the focusing conditions and actual applied fluence, similar to the situation at 1030 nm. Fig. 4.14 shows the increase of the maximum achievable depth with the pulse energy for different focusing conditions at both wavelengths. Drilling with the frequency doubled radiation reaches a larger final depth at the same pulse energy compared to 1030 nm. For example at a pulse energy of 15 μJ, there is an average increase of ca. 100% from 150 μm at 1030 nm to 300 μm at 515 nm. The enhancement decreases for higher pulse energies, but still reaches ca. 20% for a pulse energy of 50 μJ.
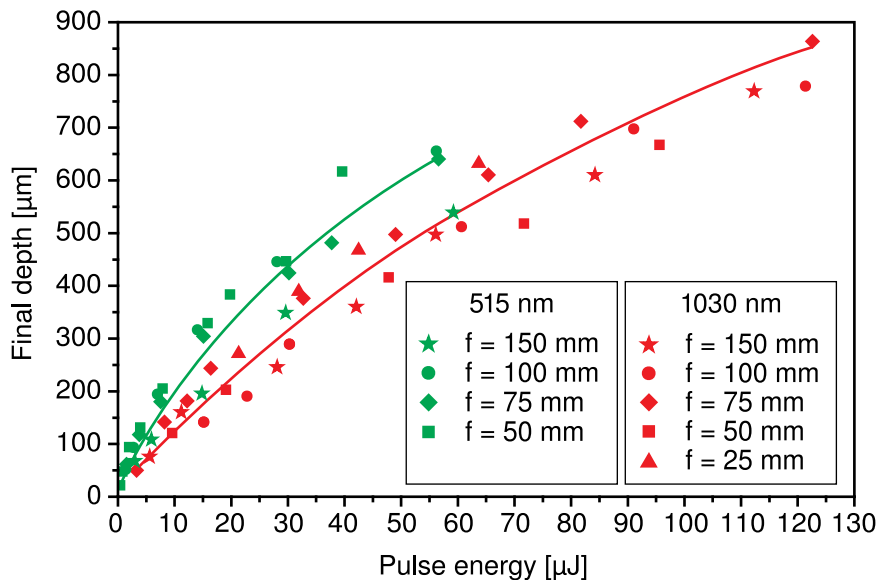
Fig. 4.14: The final hole depth is primarily dependent on the applied pulse energy and largely independent of the focusing conditions. For the same pulse energy, drilling at 515 nm achieves a larger depth than 1030 nm. The lines are a guide to the eye, only.

Fig. 4.15 shows a comparison of drilling at 1030 nm and 515 nm under tight focusing with a focus diameter of ca. 10 μm at the sample surface for both wavelengths. This is realized by using different lenses, $f = 25$ mm at 1030 nm and $f = 50$ mm at 515 nm[1].

---

[1]Due to the tight focusing at 1030 nm (numerical aperture > 0.1), the measured spot size is larger than the estimation according to equation 4.1.

Drilling is performed under otherwise identical conditions, i.e. at a pulse energy of $30\,\mu J$, which corresponds to a fluence of $75\,J/cm^2$.

Fig. 4.15: For drilling under tight focusing conditions ($10\,\mu m$ focal diameter), deviations of the hole shape, e.g. enlarged diameter, indentations, hole taper and bending, are significantly more pronounced at $1030\,nm$ (a) than at $515\,nm$ (b).
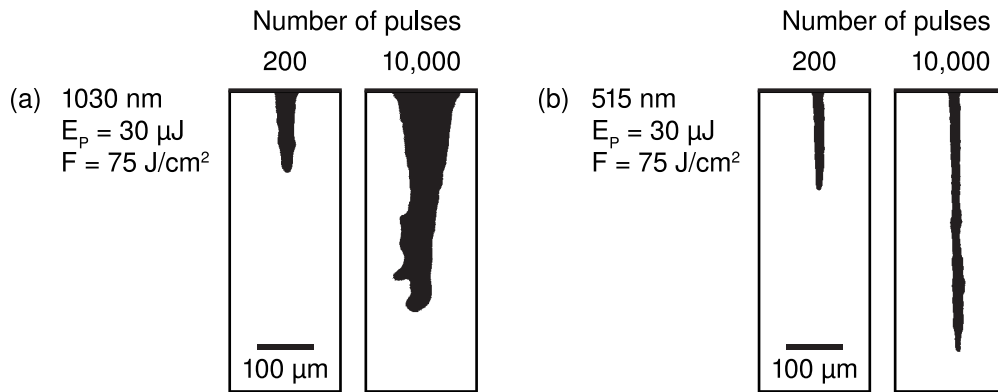
After 200 pulses, both holes show the typical shape of the initial hole. However, at $1030\,nm$, the hole diameter is approximately twice as large as for drilling at $515\,nm$. In addition, the first indentations that occur on the sidewalls are larger for $1030\,nm$ compared to $515\,nm$. The shape of the final hole then shows a significant difference, see fig. 4.15 at 10,000 pulses. The hole at $1030\,nm$ now features a dominant taper. The size of the entrance diameter is ca. $100\,\mu m$ and exceeds the spot size on the surface by far. The generation of this pronounced taper and the large hole diameter can be attributed to the excessive beam divergence or low Rayleigh-length, respectively. The focal diameter of $10\,\mu m$ results in a Rayleigh-length of ca. $80\,\mu m$ at $1030\,nm$, which has to be compared to the final hole depth of nearly $400\,\mu m$. The progressive widening from the initial to the final state is due to redirection of pulse energy to the sidewalls. In contrast, at $515\,nm$, the Rayleigh-length is doubled to ca. $160\,\mu m$ which contributes to a significantly reduced widening. In fact, the upper part of the hole keeps its diameter till the final state and the hole reaches an aspect ratio of approximately 20:1. This difference in hole formation, especially regarding the taper, can already be observed for the hole shape evolution shown in fig. 4.12, but is more distinct in case of the smaller focal spot here. The lower part of the hole at $1030\,nm$ features the typical bending as well as multiple branches and large cavities. At $515\,nm$, bending as well as the formation of multiple hole ends and large indentations is substantially reduced. Nevertheless, indentations occur

frequently along the sidewalls. This example demonstrates the benefit of frequency-doubled radiation in the generation of deep holes under the demand of a minimized diameter and therefore tight focusing conditions.

In summary, the general characteristics of the drilling behavior and shape formation are similar for 515 nm and 1030 nm despite the difference in intrinsic absorption. There is also a similar dependence of the final hole depth on the pulse energy for both wavelengths, although a larger maximum depth can be achieved for 515 nm in comparison to 1030 nm. The formation of indentations, cavities and the hole bending is reduced to smaller size at the lower wavelength. Drilling with the frequency-doubled radiation benefits from the improved focusability. On the one hand, this enables a smaller focal spot size with the same focal length and on the other hand decreases the beam divergence for an equal spot size in comparison to the fundamental wavelength. For drilling of holes with small entrance diameter, e.g. $\leq 10\,\mu m$, and therefore required tight focusing conditions, a wavelength of 515 nm results in significantly reduced deviations of the hole shape, especially indentations, hole taper and bending as well as the average hole diameter, in comparison to 1030 nm.

4.2.4 Pulse Duration

Beside pulse energy and wavelength, the pulse duration is another key parameter of the drilling process, which also affects the ablation mechanisms, see chapter 1. The following comparative study concentrates on three fundamental domains of pulse duration: femtosecond pulses, here at 50 fs, picosecond pulses at 1 ps and nanosecond pulses at 10 ns. Hence, the pulse duration is varied over five orders of magnitude. A Ti:Sa-CPA-laser system (Spectra-Physics Tsunami/Spitfire) allows to address these pulse duration domains at a wavelength of 800 nm. The Chirped Pulse Amplification technology (CPA) enables a variation of the pulse duration under nearly identical beam parameters [142, 143]. Detuning the pulse compressor covers a range from approximately 50 fs to 10 ps. A pulse duration of ca. 10 ns is realized in unseeded operation of the amplifier. The pulse duration is measured and controlled by an autocorrelator in the ultrashort pulse regime and a fast photodiode in the ns-regime. In this experiment the drilling laser is focused to the sample surface with a plano-convex lens of 100 mm focal length resulting in a focal spot size of ca. 35 μm. The pulse energy is varied in the range of 25 μJ to 600 μJ.

The characteristic behavior of the drilling process and typical evolution of the hole shape as described in section 4.1 can be observed for all pulse durations under investigation. Especially the three process phases are clearly distinguishable for every parameter combination. However, the specific development of a hole depends on the actual parameter set of pulse duration and energy. The experiments reveal two different regimes of hole shape evolution. One occurs for low pulse energies in the range of 75 μJ or below and another one for high pulse energies above 75 μJ. In the following, these regimes are discussed on the basis of particular examples which are nevertheless typical and represent the characteristic relations between the different pulse duration regimes.

The hole shape evolution at a pulse energy of 50 μJ, representing the low pulse energy regime, is shown in fig. 4.16. In the example here, the pulse energy of 50 μJ corresponds to a fluence of ca. 10 J/cm^2. The quantitative development of the hole depth can be found in fig. 4.17.
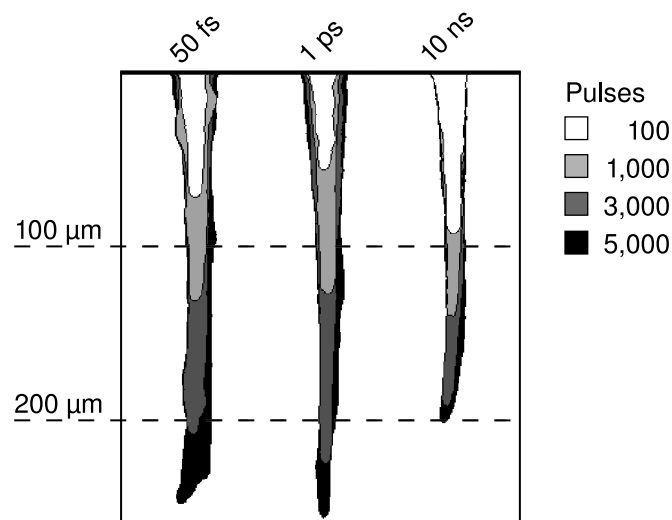
Fig. 4.16: The hole shape evolution in the low pulse energy regime is similar for fs-, ps- and ns-pulses, here for a pulse energy of 50 μJ (fluence of 10 J/cm^2).

After the first drilling phase, see for example the hole shape after 100 pulses, all three pulse duration regimes show the characteristic shape of the initial hole with the typical taper. The hole depth for ns-pulses is larger than for ultrashort pulses. This behavior can be expected due to the higher ablation rate for ns-pulses in comparison to ultrashort pulses for fluences ≥ 10 J/cm^2 [35]. Due to significant heat diffusion during the ablation process for ns-pulses, they can heat and evaporate a larger material volume than the

Fig. 4.17: The quantitative evolution of the hole depth in the low pulse energy regime shows a similar behavior with the three characteristic process phases for fs-, ps- and ns-pulses, here for a pulse energy of 50 μJ.

ultrashort pulse regime. However, this effect only occurs for holes with low aspect ratio and is even reversed for further drilling. Here, the effectively irradiated area increases and the fluence at the hole bottom decreases below $10\,\text{J/cm}^2$, wher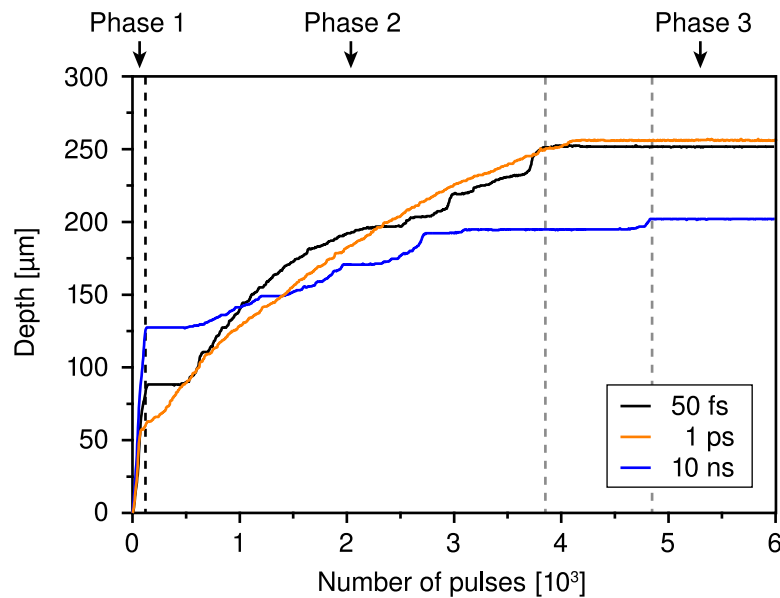e ultrashort pulses show a higher ablation rate. In addition, heat diffusion occurs also along the sidewalls for irradiation inside the hole and leads to a faster temperature relaxation [15]. This affects in particular the thermally driven ablation by ns-pulses and can result in a significant reduction of the ablation rate.

All pulse duration regimes show the characteristic, stepwise increase in depth during the second process phase, see fig. 4.17. The actual depth evolution differs for each hole due to the statistical variations of the process, see also section 4.1.2 on this topic. In the example here, a stop of forward drilling and a period of constant depth occurs even directly at the beginning of the second process phase for ns- and also fs-pulses. The final hole depth is reached after ca. 4,000 pulses for the ultrashort pulse regime and ca. 5,000 pulses in case of ns-pulses. Such a duration of the drilling process is within the typical variation limit. Compared to the depth of the initial hole after 100 pulses, the final depth is a factor of two to four larger, which is also in agreement with previous results in section 4.2.1. The final depth for ns-pulses is lower compared to fs- and ps-pulses due

to the lower ablation rate inside deep hole capillaries. Nevertheless, similar basic hole shape features can be observed for all pulse durations, especially the hole taper and the bending in the lower part of the hole.

The relations in the high pulse energy regime are represented in the following for a pulse energy of 500 µJ, and corresponding fluence of ca. 100 J/cm², which is ten times higher than in the example of the low pulse energy regime. The shape evolution is shown in fig. 4.18 and the corresponding quantitative depth development in fig. 4.19.
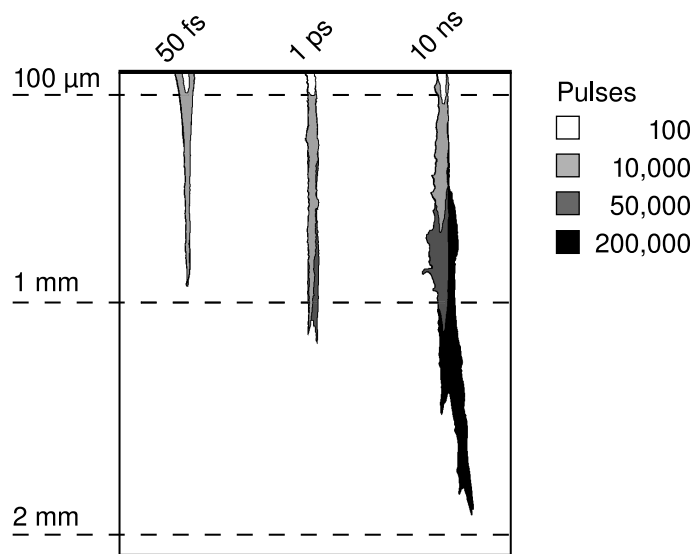
Fig. 4.18: Hole shape formation in the high pulse energy regime for fs-, ps- and ns-pulses, here for a pulse energy of 500 µJ (corresponding fluence of 100 J/cm²).

The shape of the initial hole, after 100 pulses, is again similar for all pulse durations. The depth reached for ns-pulses is again larger compared to fs- or ps-pulses due to the higher ablation rate at this high fluence. Up to this point, the behavior is still comparable to the low pulse energy regime.

The second process phase is also characterized by a gradually decreasing drilling rate and strong variations in the depth development for all pulse duration regimes. At this pulse energy, there are significant differences in process duration and shape evolution. For ultrashort pulses, an increase of the depth to approximately 1 mm and an aspect ratio of ca. 10:1 occurs within less than 10,000 pulses. Nanosecond pulses, on the other hand, show a lower drilling rate in deep hole capillaries and hence have a lower depth after 10,000 pulses. In this case, ca. 50,000 pulses are required to reach a similar depth.

Fig. 4.19: The duration of the drilling process in the high pulse energy regime increases with the pulse duration, especially for ns-pulses, and features more pronounced intermediate periods of constant depth, here for a pulse energy of 500 μJ.

The final hole depth is obtained by fs-pulses after ca. 10,000 pulses. The hole shape is dominated by an accentuated taper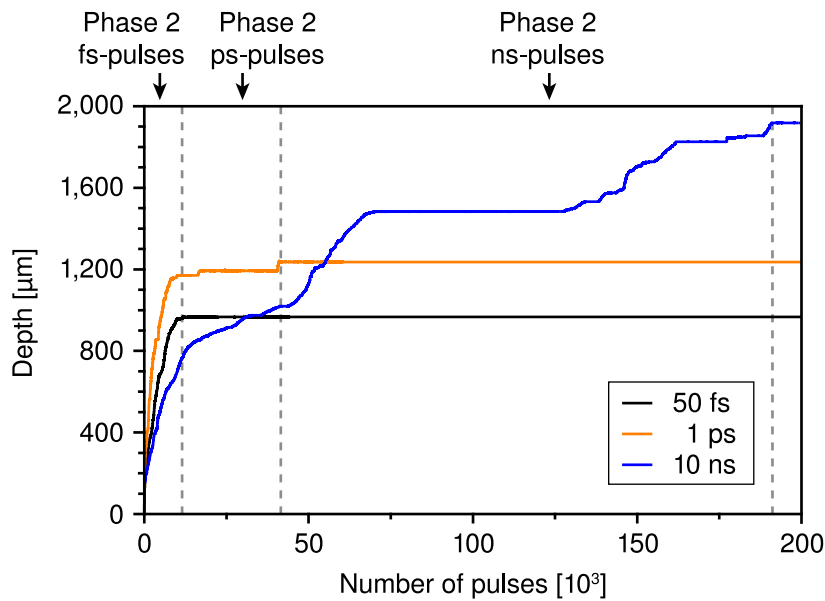 with a large entrance diameter and a sharp tip at the hole bottom. Notably, the entrance diameter for this pulse duration regime is about three times larger than for ps- and ns-pulses. This can be attributed to a beam broadening by nonlinear interaction of the highly intense laser pulses with the ambient air and the ablation plume [35].

For ps-pulses, forward drilling continues up to ca. 40,000 pulses, but only with a marginal increase in depth compared to the situation after 10,000 pulses. The hole is reshaped until a second branch is formed. The final hole shows a minimal taper and almost cylindrical shape. This is in agreement with previous observations of the influence of a high pulse energy on the shape formation, see section 4.2.1. Nevertheless, small imperfections like bulges occur frequently along the sidewalls of the hole.

For ns-pulses, a far longer continuation of the drilling process can be observed. In this experiment, it was followed for up to 200,000 pulses but a further continuation might be possible after a longer period of constant depth. The second drilling phase in this case is accompanied by a pronounced formation of large, internal cavities, domains with extended diameter and a multitude of branches. The reshaping process

can substantially change the hole shape, increase the average diameter of the capillary, and lead to further forward drilling even at a large hole depth. The periods of constant depth can last for several ten thousand pulses, though. The final depth of the hole reaches ca. 2 mm. However, the drilling process requires significantly more pulses than for fs- or ps-pulses.

A quantitative comparison of the final hole depth for the different pulse duration regimes in dependence of the applied pulse energy is shown in fig. 4.20.
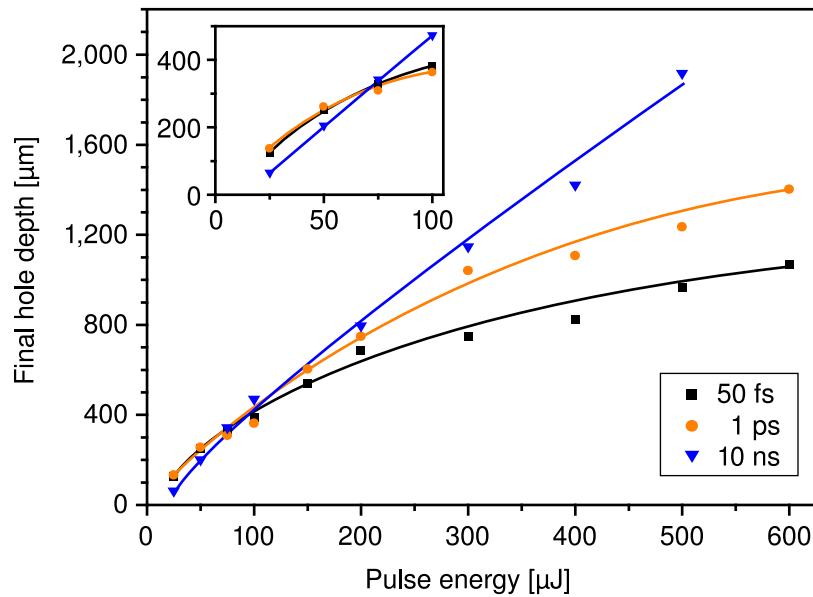
Fig. 4.20: In the low pulse energy regime ($<75\,\mu$J), fs- and ps-pulses reach a larger final depth than ns-pulses. The high pulse energy regime ($>75\,\mu$J) shows an increasing depth with prolonged pulse duration. The lines are a guide to the eye, only.

For pulse energies lower than $75\,\mu$J, fs- and ps-pulses reach approximately the same depth and also show a similar increase with increasing pulse energy. Nanosecond pulses only achieve a lower hole depth. Nevertheless, the final depth for ns-pulses grows substantially with increasing pulse energy. Hence, at $75\,\mu$J all pulse duration domains reach nearly the same final depth. For higher pulse energies, the achieved final depth increases linearly with the applied pulse energy for ns-pulses. In contrast, ultrashort pulses show a saturation of the depth increase which is most distinct for fs-pulses. On the one hand, this can be attributed to nonlinear interaction of ultrashort pulses with the ambient atmosphere in front of the focus, which can reduce the energy that reaches the sample surface [15, 35]. On the other hand, ns-pulses show a widening of the hole,

especially in the middle part, which is not the case for ultrashort pulses, see fig. 4.18. The increased average diameter for ns-drilled holes might reduce the propagation losses within the hole and therefore sustain a longer continuation of forward drilling. Hence, the final hole depth increases with the pulse duration in the high pulse energy regime, though, in connection with a longer process duration to reach this final depth.

A further quantitative evaluation of the hole quality takes the variation of the hole diameter into account. The standard deviation of the final hole diameter in dependence on the applied pulse energy is shown in fig. 4.21. For fs- as well as ns-pulses a
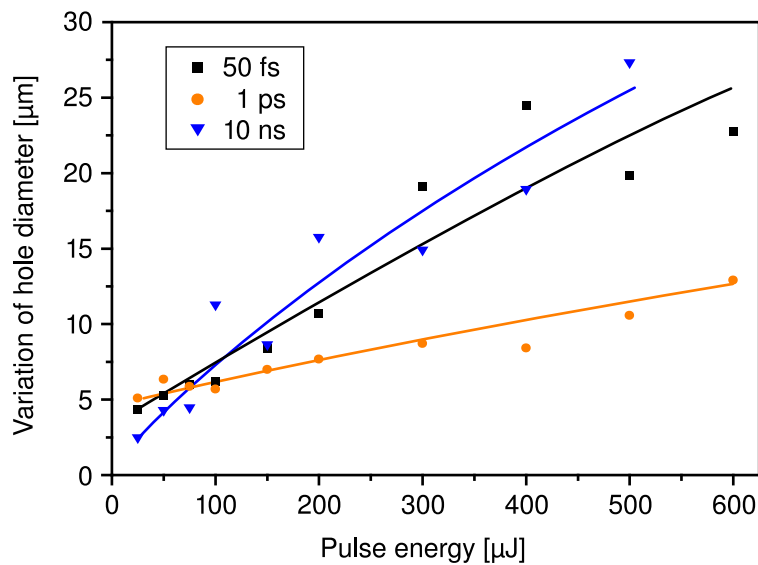
Fig. 4.21: The variation of the hole diameter increases significantly with the applied pulse energy for fs- and ns-pulses while ps-pulses show a only a slight increase. The lines are a guide to the eye, only.

strong increase with increasing pulse energy can be observed reaching up to 25 µm for the highest pulse energies. In case of ns-pulses, the strong variation results from the formation of large bulges, cavities and the branching of the capillary during the hole shape formation. In contrast, the hole shape for fs-pulses features a gradual reduction of the diameter along the depth due to the distinct taper while there are only minor imperfections along the sidewalls. The ps-pulse regime shows only a low variation, even for the highest pulse energies still below 10 µm, and also only a slight increase with increasing pulse energy due to to the almost straight hole shape with nearly constant diameter. Although the holes also feature frequent bulges and indentations on the sidewalls, they are nevertheless small and do no cause a strong variation.

In summary, the typical drilling process with three characteristic phases can be observed for femtosecond, picosecond as well as nanosecond pulses. For low pulse energy (≤ 75 µJ here), the actual development of the hole during these phases is also similar for the various pulse durations. For high pulse energy (> 75 µJ), a different evolution can be observed especially in the second drilling phase, which results in different final hole shapes. For ps-pulses, straight holes with a low variation in diameter are formed. Femtosecond pulses show a most distinct taper due to a nonlinear broadening of the beam at the high peak intensity of these pulses. Nanosecond pulses support the longest drilling duration and reach a significantly larger final depth compared to ultrashort laser pulses. This can be attributed to an enhanced reshaping and widening of the capillary which eventually allows for a continuation of forward drilling even at large depths, but also causes large hole wall indentations and a pronounced branching.

4.3 Three Phase Model of the Deep Drilling Process

The investigations of deep drilling in silicon revealed a process behavior consisting of three main phases, which can be distinguished from the depth development and the shape evolution. The segmentation of the process into these phases is characteristic under all processing conditions such as different pulse energies, wavelengths and pulse durations. The actual shape evolution and process duration, however, differs in dependence of the processing parameters. In addition, this typical behavior has been observed exclusively for deep drilling and does not occur for shallow structures, for example at insufficient pulse energy or inappropriate focusing.

Despite the parameter-specific dependencies, the characteristic phases of the drilling process can be described as follows:

1. The first, initial process phase shows the excavation of a tapered hole with a funnel shaped entrance and a rounded tip at the end during the first few hundred pulses. The shape evolution is a direct result of the Gaussian intensity distribution of the incident laser beam. The drilling rate is constant or even increases slightly with ongoing irradiation, especially during the first few pulses, which can be attributed to an incubation effect increasing the energy coupling to the material [95, 110, 140]. A similar development of the depth in particular the increase of the ablation rate has also been observed for drilling in stainless steel [139]. The drilling rate in this

phase is the highest of the whole process. The depth of the initial hole ranges from approximately 50 μm to 250 μm for the processing parameters under investigation here. In contrast to these observations, the Hirschegg-model specifies a constant ablation rate for the first few pulses only and a gradual decrease afterwards.

2. The second process phase is characterized by a significant decrease of the drilling rate. In addition to forward drilling, ablation now also acts on the sidewalls in transverse direction and leads to the formation of indentations and cavities along the hole walls. The direction of forward drilling can also differ from the direction of the incident beam and result in a bending of the hole capillary. The formation of these hole shape features always occurs for several consecutive pulses. Due to the periods of predominant transverse ablation, there is no continuous increase of the hole depth, but a fluctuation of the drilling rate. The depth evolution even shows intermediate periods without forward drilling. During these periods, ablation continues and reshapes the hole channel, especially by widening of the capillary and flattening of the hole bottom. This reshaping process is important for a further continuation of drilling in forward direction. The duration of such intermediate periods of constant depth increases with increasing hole depth. The average drilling rate, therefore, decreases with an increasing number of applied pulses. The actual depth evolution and shape formation is subject to statistical variations and differs for every drilling process.

A very similar depth evolution, including the fluctuations of the drilling rate during the process, has been observed in on-line depth measurements for drilling stainless steel with ps-pulses [32]. These investigations also observe a backscattering from the hole walls at certain depths [32], which can be attributed to the formation of indentations and bulges as observed in the present work.

The phenomenon of bending in the lower part of the hole as well as local widening, has also been observed for drilling in diamond [21]. This phenomenon has been attributed to a structural anisotropy of the sample. However, material inhomogeneities are unlikely for the crystalline silicon used in this study. Alternatively, the branching and bending of the hole might be induced by a random change of the beam pointing due to interaction with the plasma filament inside a deep hole, which was observed as a randomly changing plasma position when drilling silicate glasses with fs-pulses [37]. The in-situ imaging of the drilling process,

though, shows a consecutive growth of individual branches and indentations for a multitude of consecutive pulses in contrast to a random change of the ablation site from pulse to pulse.

The decrease of the drilling rate after the formation of an initial hole is also described in the Hirschegg-model, see section 2.2. However, a long process phase with a constant drilling rate as in the Hirschegg-model is not observed in the present work. A general description of the depth evolution with a χ-parameter according to the Hirschegg-model is also inappropriate for the drilling in silicon due to the fluctuations of the drilling rate in the main part of the process.

3. The third and final process phase shows no further drilling in forward direction. Consequently, the final hole depth is reached and remains constant. However, the hole shape still undergoes changes, which may lead to additional branches or hole ends but the reshaping is not sufficient to enable a further increase in depth. Additional widening of the capillary, especially in the upper part of the hole can be attributed to slow ablation of the sidewalls by the low-intensity flanks of the beam. Such erosion of the sidewalls after the channel formation has also been reported for fs-drilling of stainless steel [116].

In conclusion, the drilling process observed in silicon is in agreement with recent on-line measurements of the depth development for drilling of metals [32, 139]. This shows, that the drilling behavior in silicon is also representative for other opaque materials, especially metals. Similar to the Hirschegg-model, the drilling process can also be described by distinct process phases. The phases observed here, however, show different characteristics compared to the established model. This might be attributed to the fact that the Hirschegg-model is essentially based on drilling investigations of ceramics with ns-pulses [19, 24] and therefore different material and absorption properties compared to this study.

5 Hole Shape Formation Processes

The shape evolution of deep holes is characterized by ablation in transverse direction to the incident laser beam and the formation of indentations, local widening and bending of the hole. Several different mechanisms can be possible causes of this shape formation as illustrated in fig. 5.1.
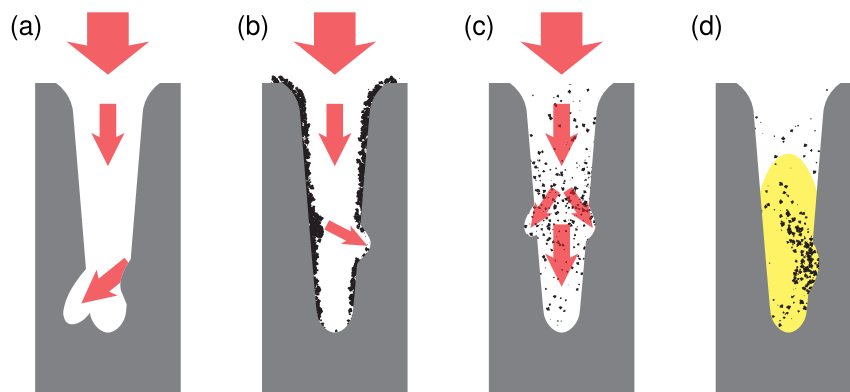
Fig. 5.1: Different mechanisms may cause the characteristic deviation of the ablation direction from the incident beam, e.g. deflection of the incident beam at the hole walls (a), influence of debris on the pulse propagation (b), interaction of subsequent pulses with ablation particles (c) and the abrasive effect of plasma and ablation particles (d).

(a) For deep holes with high aspect ratio, the pulse propagation inside the hole channel may be influenced by the hole capillary and thus change the intensity distribution at the hole bottom. The process of the reshaping of the hole during intermediate periods without forward drilling, as shown in section 4.1.2, and the influence of the focus position on the achievable depth, see section 4.2.2, are indications of this effect. Previous investigations also showed how polarization-dependent reflection on the hole walls can influence the cross-section of the hole [27]. In addition, the formation of a distinct tip at the hole bottom is attributed to multiple reflections on the sidewalls [40].

(b) Deflection or scattering of the incoming pulse might be induced in the same way by particle depositions on the hole walls.

(c) The expanding vapor plume may cause scattering or deflection of subsequent pulses [144]. This effect is especially pronounced at short pulse intervals, i.e. at high pulse repetition rates, and has been observed as particle shielding in previous investigations [65, 88]. In addition, ablation particles within the hole channel can lead to plasma ignition by subsequent pulses [35]. This plasma may then cause a deflection or scattering of the incident pulse [25, 37].

(d) The laser-induced plasma as well as the ablation particles may also transfer energy to the sidewalls and cause ablation in addition to the direct effect of the laser pulse. Therefore, they represent a second source of material removal [19, 24, 36, 91].

This chapter presents a systematic study of the aforementioned mechanisms based on experimental investigations in combination with a simulation of the pulse propagation inside the hole capillary.

5.1 Influence of the Ambient Pressure

The redeposition of ablation products in the vicinity of the ablation site is a common effect in ultrashort pulse processing caused by the generation of nanoparticles and atomic clusters during material removal [74, 76, 145]. In case of silicon, this effect is especially pronounced and the formation of large cotton-like particle aggregations can be observed on the surface [136]. Nevertheless, the aggregation and deposition can be reduced by increasing the mean free path of the ablation particles under reduced ambient pressure. At 10^{-1} mbar, only a low density of debris and nearly no particle deposition is observed [136, 146]. Moreover, a reduced ambient pressure also reduces the nonlinear interaction of the laser pulse with the atmosphere [15, 92]. In addition, ignition of plasma on the ablation particles is diminished, resulting in a significantly reduced erosive effect as well as minimized beam deflection [15, 36]. Hence, widening of the hole and distortion of the hole shape can be suppressed for drilling under vacuum conditions compared to atmospheric pressure [34, 124]. Therefore, a reduction of the ambient pressure and thereby decrease of the density of the ablation particles can be expected to have a significant influence on the hole formation process.

To investigate the influence of the ambient pressure, the sample is embedded in a vacuum chamber that enables a pressure reduction from atmospheric conditions (1,000 mbar) to medium vacuum ($2 \cdot 10^{-3}$ mbar). With this decrease of pressure, the mean free path of the ablation particles is enhanced. In addition, the expansion velocity of the ablation plume increases [147]. In a first approximation, the mean free path of molecules in a gas is inversely proportional to the pressure and typically ranges from a few tens of nanometers at 1,000 mbar to several hundred micrometers at 10^{-2} mbar [106]. Compared to the gas molecules, the actual ablation particles have a different size and temperature and also show a directed movement. Nevertheless, this basic approach can still provide a rough estimation of the movability of the ablation products, since the ambient gas will offer a certain mechanical resistance against their expansion. For the lowest pressure setting in this experiment, a mean free path of the ablation particles that matches or even exceeds the hole depth can be expected and therefore a significantly reduced particle deposition.

5.1.1 Drilling Behavior under Different Ambient Pressure Conditions

In general, the typical process phases of percussion drilling can be identified for all pressure conditions investigated here. The characteristics of these phases, however, differ with respect to the actual process parameters. In the following, the hole shape evolution is discussed for a pulse energy of 125 μJ at 1030 nm and a pulse duration of 8 ps (FWHM). The laser beam is focused to the sample surface with a lens of 100 mm focal length, resulting in a focal spot size of ca. 28 μm. At this pulse energy, this leads to a fluence of ca. 40 J/cm^2.

The development of the hole depth in the first 800 pulses is shown in fig. 5.2 (a). For each pressure setting, the depth evolution is represented by a typical example. The initial phase enfolds within the first few hundred pulses and shows the highest ablation rate of the drilling process. The transition to the second process phase is then marked by a significant drop in drilling efficiency. Here, the almost linear depth increase of the first drilling phase is observed up to approximately 250 pulses at every pressure, marked by a dashed line in fig. 5.2 (a). The average ablation rate in this initial phase is ca. 0.6 μm per pulse at 1,000 mbar. An enhancement by approximately 40% to 0.8 μm is observed when reducing the pressure to 100 mbar. For further pressure reduction, the drilling rate maintains this level and does not exceed 0.8 μm per pulse. This increase of the drilling

rate can be observed for all pulse energies under investigation here, i.e. from 25 μJ to 125 μJ. However, it is less distinct for lower pulse energies. For example, at a pulse energy of 50 μJ, the drilling rate increases by ca. 25% from 0.30 μm per pulse at 1000 mbar to 0.38 μm per pulse for 100 mbar and lower pressure. These observations are in agreement with drilling rates measured in stainless steel [124, 125] and aluminum [20]. They show a similar increase of the ablation rate for pressure reduction to 100 mbar and beyond that a constant level. In addition, a similar influence of the pulse energy was observed. The higher drilling rate can be attributed to a lower mechanical confinement of the ablation products and plume due to the surrounding gas envelope [147–149] as well as less cooling when the ambient pressure is reduced [148]. The pressure dependence can also be predicted by a thermal evaporation model developed by Mezzapesa et al. [125].

(a) Depth evolution   (b) Hole shape after 200 pulses
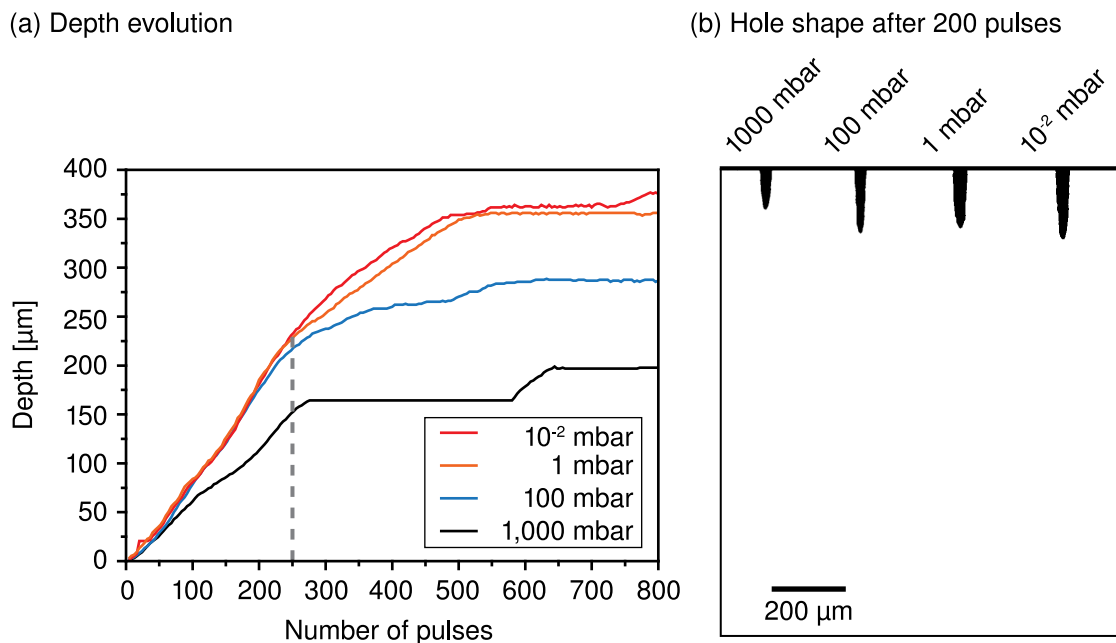
Fig. 5.2: Initial evolution of the hole depth (a) and the hole shape after 200 pulses (b) at different ambient pressures for a pulse energy of 125 μJ. A pressure reduction increases the drilling rate but otherwise the hole shape is similar under all pressure conditions.

A comparison of the hole shape after 200 pulses, i.e. approximately the end of the initial phase, is shown in fig. 5.2 (b) for different pressure conditions. Apart from the larger depth of the holes drilled under reduced pressure, all holes have a similar shape including a comparable width, taper and shape of the tip, which is typical for drilling with a Gaussian shaped beam.

Fig. 5.3 (a) shows the further development of the hole depth covering the second process phase up to 30,000 pulses. For every pressure setting, the average drilling rate gradually decreases. In addition, the characteristic periods with constant hole depth occur for every pressure condition.
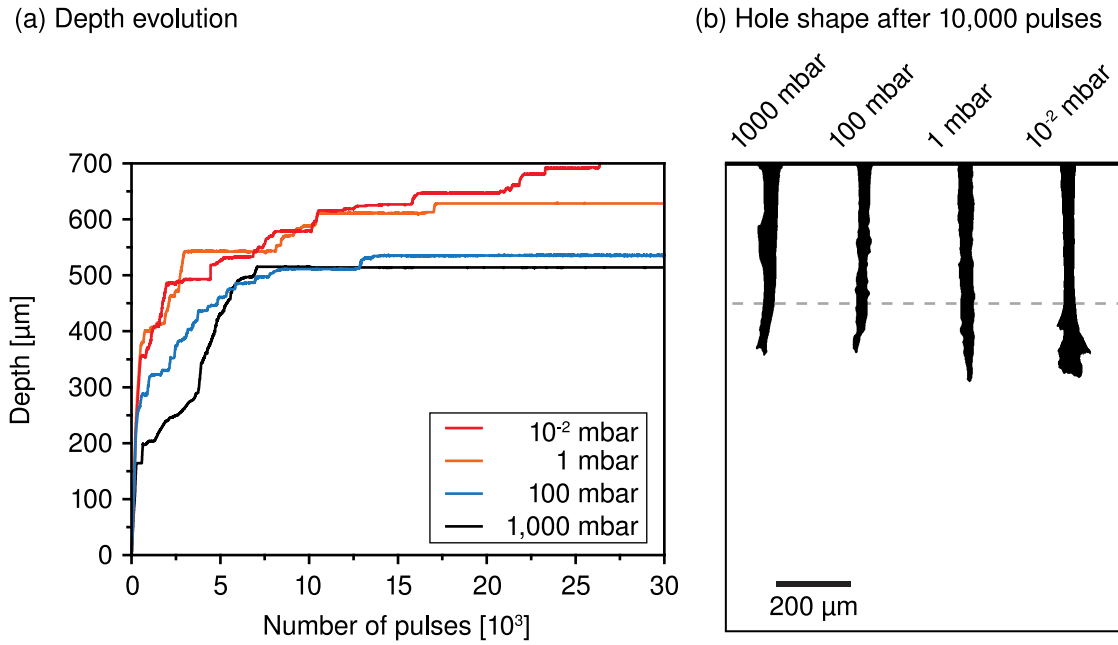
Fig. 5.3: Depth evolution in the second drilling phase (a) and the hole shape after 10,000 pulses (b) at different ambient pressures for a pulse energy of 125 µJ. The general behavior is similar for all pressure conditions and the typical hole bending occurs approximately at the same depth, marked by a dashed line here.

Due to the strong variations of the depth increase, the hole depth after a certain number of incident pulses cannot be predicted in this phase. There is no longer a clear correlation between the hole depth and the ambient pressure as in the initial process phase. In some situations, the hole depth still increases with decreasing pressure, e.g. in the range of 2,000 to 3,000 pulses, but for ca. 5,000 to 10,000 pulses drilling at 1,000 mbar results in a larger depth than at 100 mbar and likewise for 1 mbar compared to 10^{-2} mbar. Note, the examples in fig. 5.3 (a) show a typical development, but the actual depth evolution is different for every repetition of the experiment. Nevertheless, the final hole depth is larger for decreasing pressure, which is already indicated after 20,000 pulses in fig. 5.3 (a) and becomes even more distinct for a higher number of pulses, see below.

Fig. 5.3 (b) shows the hole shape in the second process phase after 10,000 pulses. For every pressure condition, the typical shape features can be observed, in particular bulges and indentations along the sidewalls, bending of the hole and possibly also the formation of multiple branches. These deviations in shape are most distinct for an ambient pressure of 1,000 mbar. This might be attributed to the abrasive effect of the laser-induced plasma, which predominantly occurs at high ambient pressure [34, 124]. For lower ambient pressure, the imperfections become smaller and more frequent. Notably, bending of the hole is present under all pressure conditions and occurs approximately at the same depth, marked by a dashed line in fig. 5.3 (b). For the lowest pressure of 10^{-2} mbar, several bendings occurred consecutively in different directions, which results in a dominant branching of the lower part of the hole. Under vacuum conditions, the hole entrance shows no funnel shape and a smaller diameter compared to atmospheric pressure. This can be attributed to reduced nonlinear interaction of the laser pulse with the ambient gas and correspondingly reduced beam broadening at low ambient pressure [35, 146]. However, the expected major influence of the ambient pressure on the hole geometry, which is attributed to the plasma as a second source of ablation [34, 124], cannot be observed for the experimental conditions in this study.

The most significant difference in the drilling behavior occurs for a high number of incident pulses (> 10,000). Fig. 5.4 (a) shows the depth evolution over a range of 800,000 pulses for a pulse energy of 125 μJ. Typically, the final depth and therefore the end of the second process phase is reached after some thousand pulses. When the ambient pressure is reduced, however, forward drilling can continue for a significantly longer time. This behavior is most distinct for the lowest pressure of 10^{-2} mbar. In this case, drilling continues for the complete time under investigation here, i.e. ca. 800,000 pulses, which is about two orders of magnitude more than for atmospheric pressure with ca. 7,000 pulses[1]. The intermediate periods of constant depth are also most distinct for the lowest pressure. These can last for more than 100,000 pulses and alternate with comparably short periods of depth increase of only a few hundred to a few thousand pulses. As a general trend, the average drilling rate during the periods of growing depth decreases from step to step. At an early stage of the second process phase, i.e. after a few thousand pulses, the average drilling rate is ca. 0.3 μm per pulse at 10^{-2} mbar and comparable to the rate observed for higher pressure up to 1,000 mbar

---

[1]Note that the observation of the drilling process was stopped after 800,000 pulses, a further continuation in case of 10^{-2} mbar might still be possible after a long period of constant depth.

(a) Depth evolution

(b) Hole shape after 800,000 pulses
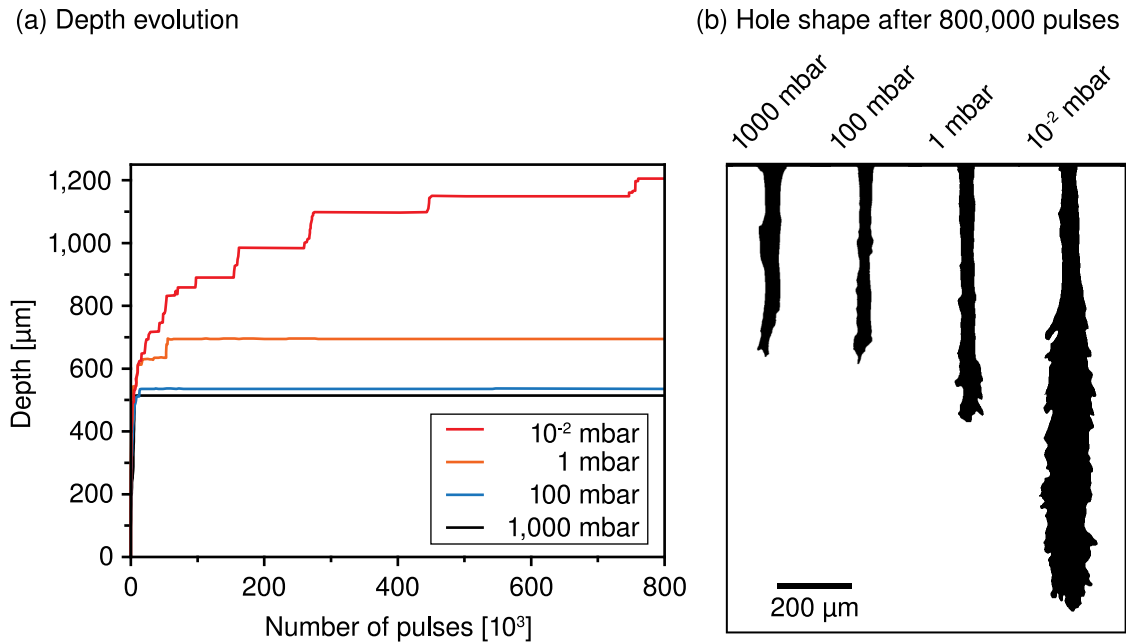
Fig. 5.4: Depth evolution up to 800,000 pulses (a) and final hole shape (b) under different pressure conditions for a pulse energy of 125 μJ. Especially for 10^{-2} mbar, forward drilling continues longer and reaches a larger depth in combination with the formation of a multitude of branches in the lower part during the pronounced periods of stepwise growth.

after the same number of incident pulses. At a later stage of the process and for a deeper hole, the average drilling rate is significantly reduced, e.g. to ca. 0.1 μm per pulse after approximately 16,000 pulses and merely 0.02 μm per pulse after ca. 450,000 pulses. In the last case, the low ablation rate indicates a fluence at the hole bottom that is close to the ablation threshold. Nevertheless, associated with the extended processing time, a hole depth of more than 1 mm is finally obtained at 10^{-2} mbar for a pulse energy of 125 μJ which is more than 100% larger compared to atmospheric pressure. Again, this effect is less pronounced for lower pulse energies but still significant. At a pulse energy of 50 μJ, the final depth increases by ca. 60% for 10^{-2} mbar compared to 1,000 mbar in combination with an increase in the number of pulses to reach the final state by one order of magnitude from 4,500 to ca. 45,000. A summary of the finally achieved depth d_{final} and the maximum number of pulses, which contribute to forward drilling N_{final} is given in table 5.1 for pulse energies of 50 μJ and 125 μJ.

Tab. 5.1: The final hole depth d_{final} and the number of pulses to reach this depth N_{final} significantly increase with reduced ambient pressure.

p	50 µJ		125 µJ	
	d_{final}	N_{final}	d_{final}	N_{final}
1000 mbar	318 µm	4,500	515 µm	7,000
100 mbar	330 µm	5,500	535 µm	14,000
1 mbar	362 µm	7,500	685 µm	55,000
10^{-2} mbar	507 µm	45,000	> 1200 µm	> 800,000

The final hole shape, as shown in fig. 5.4 (b), is very similar at 1,000 mbar and 100 mbar and mainly shows only one bending of the hole. For a pressure of 1 mbar, bending of the hole occurred several times resulting in a branching of the lower part of the hole with a crown-like structure. Notably, this is comparable to the shape at 10^{-2} mbar after 10,000 pulses, see fig. 5.3 (b). In the final state at 10^{-2} mbar, the complete lower half of the hole consists of a multitude of branches and resembles a narrow tree[2]. An individual and consecutive formation of these branches can be observed during the drilling process. This means, ablation is limited to one spot or one direction at a time, which is in agreement with the detailed observations at atmospheric pressure in section 4.1. Nevertheless, during intermediate periods of constant depth, additional branches are also formed in the middle section of the hole, i.e. in a part of the hole that already bears sidewards directed channels. Remarkably, the distance of the outermost tips of these branches from the center axis of the hole capillary is approximately the same in the complete lower section of the hole where branching occurs.

5.1.2 Hole Interior and Particle Debris Distribution

To evaluate the difference in particle deposition inside the hole, which is expected for different ambient pressure conditions, longitudinal sections of the holes have been prepared after a specified number of incident pulses by cleaving the samples. Enabled by the brittleness of the silicon, this preparation technique does not alter the interior of the hole in contrast to conventional cut-and-polish methods. Fig. 5.5 presents a comparison

---

[2]The lower part of the hole may seem to consist of a large internal cavity, which is not necessarily the case since the three-dimensional character of the hole shape and the individual branches are not visualized correctly in the hole silhouette captured by the in-situ observation method.

of two holes after 10,000 pulses drilled at a pulse energy of 125 µJ at 1,000 mbar and 10^{-2} mbar respectively. In this advanced state of the drilling process, both holes already developed the specific shape features like bulges and bending which are clearly revealed in the images of the longitudinal hole sections.

(a) Atmospheric pressure (1,000 mbar)   (b) Medium vacuum (10^{-2} mbar)
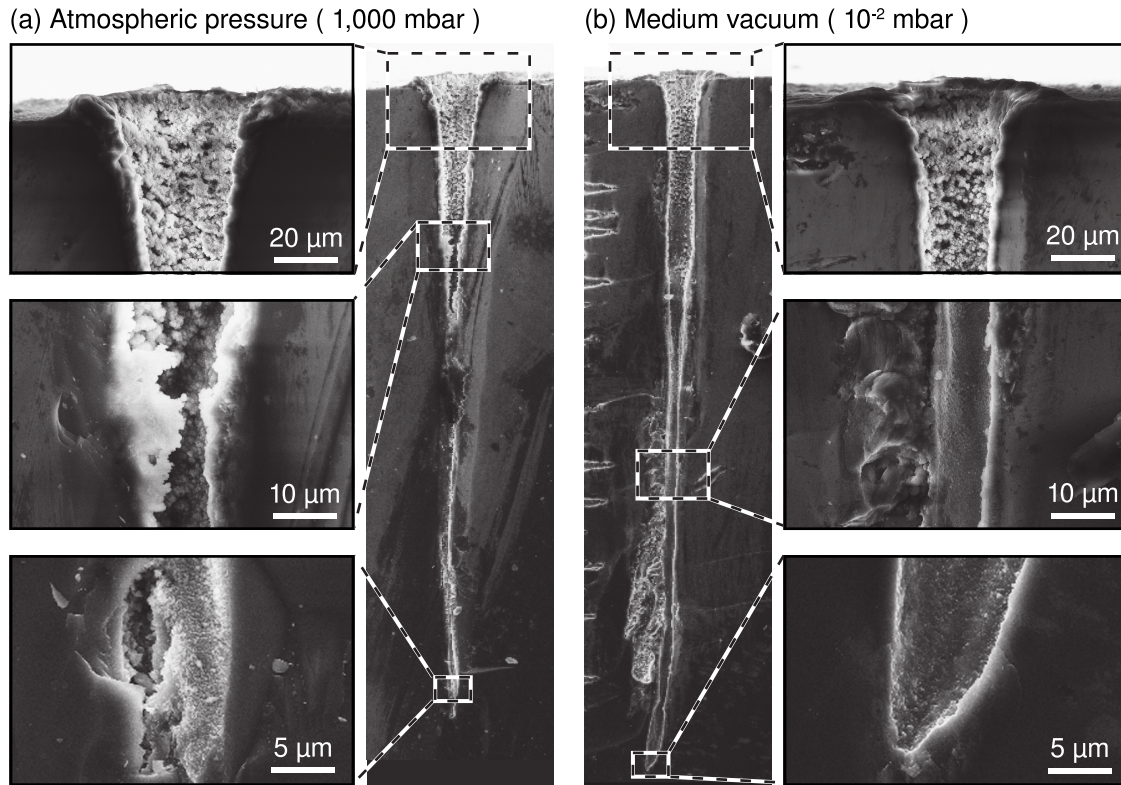
Fig. 5.5: SEM images of cleaved hole sections for a pulse energy of 125 µJ after 10,000 pulses at 1,000 mbar (a) and 10^{-2} mbar (b).

For a pressure of 1,000 mbar, see fig. 5.5 (a), the hole entrance is covered by a thick layer of agglomerated particles forming a cloud or cotton like structure. This layer is also present deeper inside the hole and covers the middle section with similar thickness, density and structure. Still at the hole tip, smaller particles and agglomerations are visible at the sidewalls. The presence of a thick debris-layer in the major part of the hole implies that this debris is stable against irradiation by subsequent pulses. On the one hand, pulses propagating through the hole capillary may only lead to low removal of those particles which can be attributed to the large surface area and the roughness of the structures. On the other hand, the ablated debris could be leveled out again by deposition of other ablation particles from the hole bottom.

At an ambient pressure of 10^{-2} mbar, see fig. 5.5 (b), a thick debris layer is present at the hole entrance similar to the situation at higher pressure. In contrast to a pressure of 1,000 mbar, the deposition of ablation particles is significantly reduced deeper inside the hole. In the middle section almost no debris is observable resulting in a clean hole channel down to the hole bottom. Despite the difference of debris in the middle and lower part of the hole for drilling at atmospheric pressure compared to vacuum, the general cross-section of the hole is similar in both cases, especially the bulging and bending towards the hole tip. Therefore, it has to be deduced that the particle deposition has no major influence on the formation of the specific hole shape features.

On the other hand, the drilling process duration and final hole depth is reduced in case of particle agglomerations inside the hole at atmospheric pressure. The thick debris effectively reduces the open hole diameter available for pulse propagation inside the hole channel and leads to strong scattering, which decreases the fluence available for ablation at the hole tip. In addition, covering the sidewalls with a scattering layer also reduces further ablation of the sidewalls and the accompanied reshaping of the hole which is necessary for a continuation of forward drilling, see section 4.1. At reduced ambient pressure, the clean sidewalls in the middle and lower part of the hole do not obstruct the pulse propagation and ablation along the walls. Therefore, more pulse energy is transmitted to the hole tip and reshaping of the hole, together with the formation of additional branches, can occur multiple times as observed by the in-situ imaging. Particle agglomerations in the upper part of the hole have only a limited effect on the pulse because they only occur in a part of the hole with a large overall diameter. Nevertheless, the occurrence of debris at the hole entrance after 10,000 pulses already indicates that deeper parts of the hole will be covered by debris after continued drilling. Eventually, this will lead to the same inhibition of forward drilling which already occurs after a few thousand pulses for higher ambient pressure.

In summary, particle depositions inside the hole capillary have a major influence on the duration of the drilling process and the achievable depth. This can be attributed to an obstruction of the hole channel by the debris. A reduced ambient pressure, can significantly diminish the particle deposition. In addition, a less dense atmosphere at low pressure also reduces the nonlinear interaction with the laser pulse. Hence, the funnel-shaped broadening of the hole entrance does not occur under vacuum conditions. However, this effect is limited to the hole entrance, close to the focus. The

typical features of the hole shape, the indentations and especially the hole bending and multiple branches, are present for all pressure conditions. Only a slightly reduced size of the indentations can be noticed at reduced ambient pressure. The expected major effect of the pressure reduction on the hole shape due to a lower influence from the particle-enhanced plasma, see also section 2.3.1, cannot be observed for the processing parameters in this experiment. Therefore, abrasion of the hole walls by the plasma as a second source of ablation only has a minor influence on the hole shape formation.

5.2 Interaction at High Repetition Rates

In the following, the effect of the pulse repetition rate on the hole shape evolution is investigated for percussion drilling of silicon at a wavelength of 1030 nm and a pulse duration of 8 ps (FWHM) using the standard in-situ imaging setup. In this experiment, the drilling laser is focused to the sample surface with a lens of 100 mm focal length. The repetition rate of the drilling laser system is controlled by an integrated electro-optic modulator. According to the repetition rate, the time interval between consecutive pulses is varied from 20 ms at 50 Hz to 2.5 µs at the maximum repetition rate of 400 kHz. In this case, a continuous observation of the hole shape evolution is impracticable due to the limited acquisition rate of the imaging system. Therefore, only snapshots after certain numbers of incident pulses can be provided. Fig. 5.6 shows the hole shape at different stages of the drilling process for drilling at a pulse energy of 60 µJ which corresponds to a fluence of ca. 20 J/cm^2. The quantitative development of the hole depth in dependence of the repetition rate is shown in fig. 5.8 for comparison, Each data point represents the average of five holes drilled under identical conditions. The error bars show the standard deviation.

After 100 pulses, the shape of the initial holes in fig. 5.6 (a) is similar for all repetition rates and all holes have a similar depth within the range of the typical variation. Hence, for the generation of this kind of holes, the processing time can be optimized by an increase of the repetition while maintaining the hole geometry[3].

---

[3]The surface quality and heat affected zone, however, may change with increasing repetition rate but they have not been under investigation here.

(a) 100 pulses

200 Hz 10 kHz 50 kHz 100 kHz 200 kHz 400 kHz

100 μm

(b) 1,000 pulses

200 Hz 10 kHz 50 kHz 100 kHz 200 kHz 400 kHz

100 μm

(c) 100,000 pulses

200 Hz 10 kHz 50 kHz 100 kHz 200 kHz 400 kHz

100 μm

(d) 1,000,000 pulses

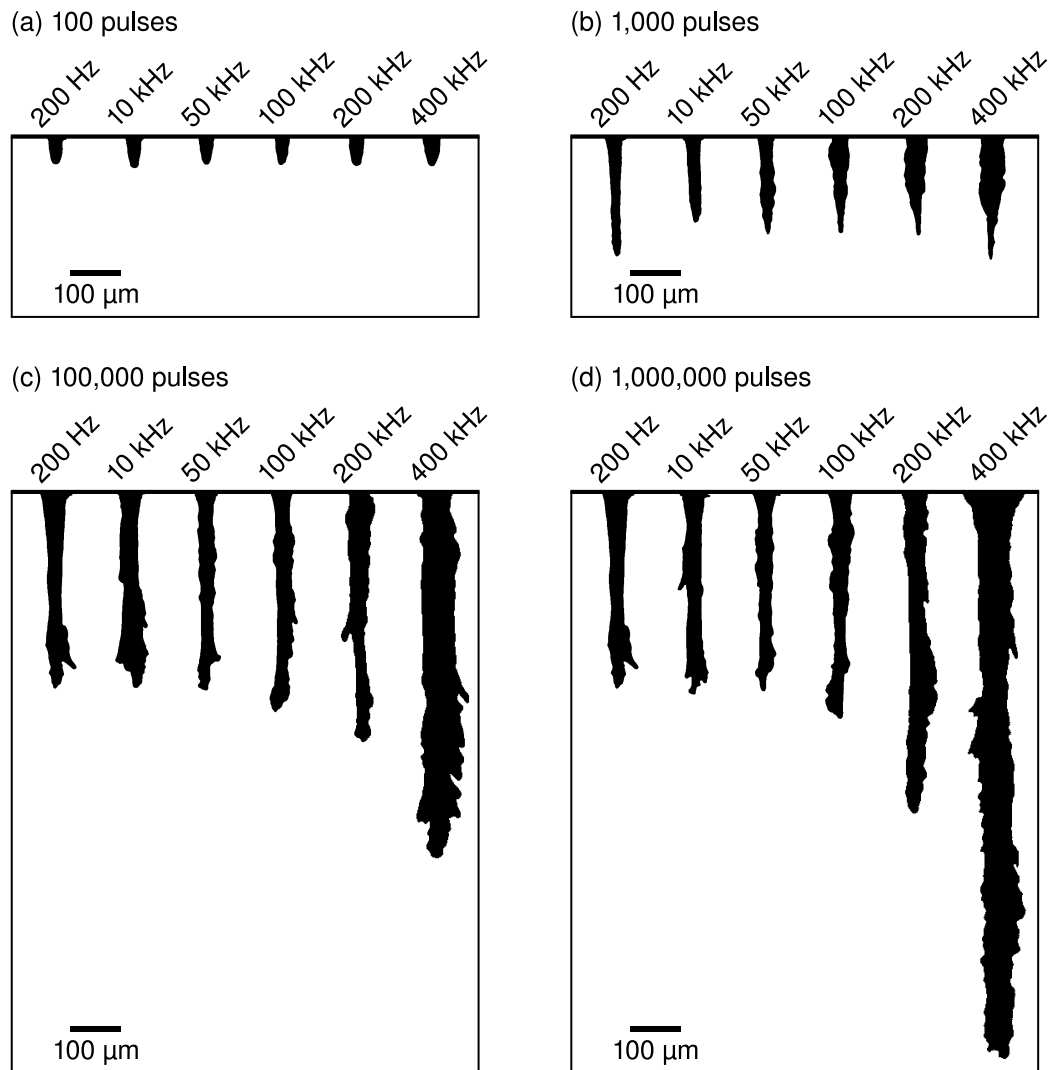200 Hz 10 kHz 50 kHz 100 kHz 200 kHz 400 kHz

100 μm

Fig. 5.6: Differences in the hole shape occur for different repetition rates and increase for an increasing number of pulses, as shown here for a pulse energy of 60 μJ.

After 1,000 pulses, repetition rates in the range of 10 kHz to 200 kHz show a reduced hole depth of ca. 20% to ca. 180 μm in comparison to ca. 230 μm at 200 Hz. This effect might be attributed to particle shielding [65, 88]. Although this effect is not obvious after the first 100 pulses, it possibly becomes more pronounced for a higher number of pulses due to the increasing confinement of the ablation particles within the deeper hole capillary. For a repetition rate of 50 kHz and higher, an increased formation of large bulges along the sidewalls in combination with a widening of the holes can be observed, especially in the upper part of the holes, see fig. 5.6 (b). The lower part of the hole shows a thinner tip compared to low repetition rates (≤ 10 kHz).

In addition, there is a significantly increased generation of melt at high repetition rates. A large amount of molten material can be found at the hole entrance after 1,000 pulses for drilling at 400 kHz in comparison to drilling at a low repetition rate of 200 Hz as shown in fig. 5.7. This pronounced melt formation indicates the occurrence of heat accumulation, similar to previous investigations of high repetition rate drilling in metals [88, 127].
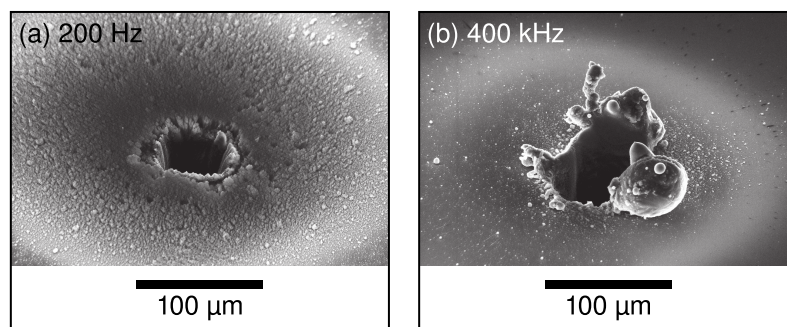
Fig. 5.7: Only low burr and particle debris is visible at the hole entrance for low repetition rates (a). Large burr of molten material and melt droplets can be observed at high repetition rates (b) as an indication of the heat accumulation effect, here after 1,000 pulses at a pulse energy of 60 μJ.

In the further drilling process, the hole shape evolution is similar for repetition rates up to 50 kHz and despite the particle shielding effect a similar depth is obtained, see fig. 5.8 for 10,000 pulses and above. At low repetition rates (≤ 50 kHz), forward drilling which usually ends after ca. 10,000 pulses. However, for higher repetition rates, forward drilling can continue for a longer time and result in a larger hole depth, see the hole shape after 100,000 pulses in fig. 5.6 (c) and the quantitative comparison in fig. 5.8. The holes at higher repetition rates (> 50 kHz) show a multitude of additional branches

Fig. 5.8: A quantitative comparison of hole depth after different numbers of pulses for a pulse energy of 60 µJ shows an enhanced achievable depth due to heat accumulation for repetition rates higher than ca. 50 kHz. The lines are a guide to the eye, only.
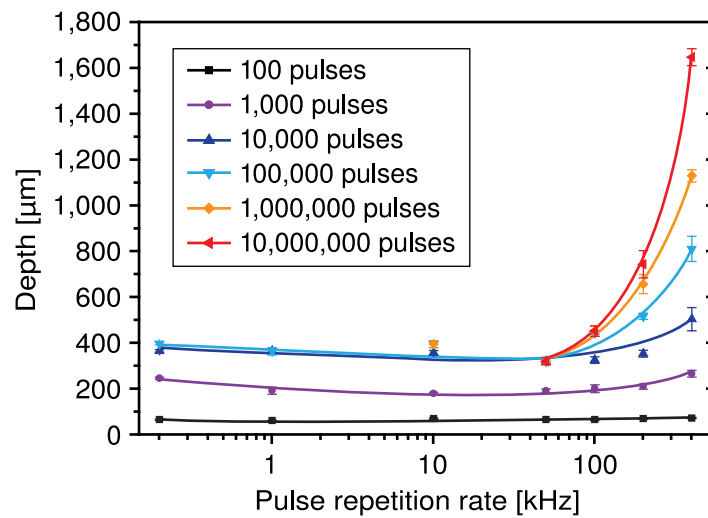
from top to bottom. These branches grow in close vicinity to each other. Possibly, they also combine and form larger cavities in some cases. This development leads to a considerably thicker hole, especially at 400 kHz, see fig. 5.6 (d). The final depth can exceed those of holes at lower repetition rates by far, e.g. by a factor of four from ca. 380 µm at 200 Hz to ca. 1,600 µm at 400 kHz after 10,000,000 pulses. At high repetition rates, especially 400 kHz, a branching of the hole can be observed over the complete depth. In addition, the entrance diameter grows further and forms a funnel shaped entrance. The average diameter of the final hole increases from ca. 35 µm at 200 Hz to ca. 70 µm at 400 kHz. This widening of the hole at high repetition rates is supposed to be responsible for the longer continuation of the drilling process and larger final depth due to an improved pulse propagation to the hole bottom within a broadened hole channel.

The substantial melt formation at high repetition rates indicates a significant influence of heat accumulation on the hole shape formation. Residual heat from the ablation process leads to an increase of the average bulk temperature in the vicinity of the ablation spot from pulse to pulse due to insufficient heat diffusion to the surrounding volume at short pulse intervals. In consequence, for subsequent pulses, less energy is required to heat the material to evaporation. In silicon, the increased average temperature also enhances the intrinsic absorption by the thermal excitation of free electrons. Therefore, the heat accumulation can facilitate ablation, which can be observed for example in

a lower ablation threshold as shown in previous investigations [150]. Eventually, the rise of the average temperature can even reach a critical temperature like the melting temperature and lead to significant melt formation, which is otherwise atypical for ablation with ultrashort pulses at low repetition rates.

A rough estimation of the temperature increase ΔT from a pulse with energy E_P at the time $t = 1/f_\mathrm{rep}$ when the subsequent pulse arrives at a repetition rate f_rep can be calculated from the analytic solution of the heat equation for a semi-infinite substrate [1, adapted from equation (7.5.5), p. 140]

$$\Delta T(t) = \frac{A E_\mathrm{P}}{4\sqrt{\pi}\,\kappa\, t\,\sqrt{Dt}}.\tag{5.1}$$

A is the fraction of the pulse energy that remains within the sample (residual heat). It accounts for reflection losses and energy taken away by the ablation products. The constant κ is the thermal conductivity and D is the thermal diffusivity. In the context of equation 5.1, a time t considerably after the end of the pulse with duration τ is assumed, which is consistent with the situation of ultrashort pulse irradiation ($\tau < 10^{-11}$ s) and pulse-to-pulse delay t in the microsecond regime for repetition rates < 1 MHz. Hence, the number of consecutive pulses to reach the melting temperature $T_\mathrm{melt} = 1687$ K [134] from an initial temperature of $T_0 = 295$ K is

$$N_\mathrm{melt} = \frac{T_\mathrm{melt} - T_0}{\Delta T\left(f_\mathrm{rep}^{-1}\right)} = \frac{(T_\mathrm{melt} - T_0)\,4\sqrt{\pi}\,\kappa\,\sqrt{D}}{A E_\mathrm{P}} \cdot f_\mathrm{rep}^{-3/2}.\tag{5.2}$$

The values calculated for a pulse energy of 60 μJ and parameters of $\kappa = 156$ W/m·K, $D = 8.6 \cdot 10^{-5}$ m^2/s [134] are given in tab. 5.2. Here, a fraction of 10% of the pulse energy is assumed to remain within the bulk material ($A = 0.1$). Even at 400 kHz several tens of pulses are required for a sufficient temperature increase. This circumstance can explain why virtually no effect of heat accumulation can be observed after 100 pulses. After a few hundred pulses, heat accumulation can be expected for repetition rates higher than 50 kHz, which agrees to the observations in fig. 5.6 (b). For low repetition rates, especially for 200 Hz, the estimated number of pulses N_melt is higher than the typical number of pulses till the hole reaches its final state. Accordingly, no influence can be observed in the experiments. The calculation presented here, however, is only a rough estimation, since the parameters of equation 5.2 are only roughly guessed and

also change with temperature. Nevertheless, it can be used as a first approximation to conceive an idea of this effect.

Tab. 5.2: Estimated number of pulses to reach the melting temperature at a pulse energy of 60 μJ due to heat accumulation according to equation 5.2.

f_{rep}	200 Hz	10 kHz	50 kHz	400 kHz
N_{melt}	$2.6 \cdot 10^6$	7500	670	30

The heat accumulation effect strongly depends on the total amount of energy deposited in the sample. Therefore, an intensified effect can be expected for higher pulse energies but a less pronounced effect effect for lower pulse energies. This is in agreement with the experimental observations. At a pulse energy of 120 μJ, a distinct increase of the hole depth can already be observed after 1,000 pulses for repetition rates > 50 kHz. A larger final hole depth is obtained for repetition rates > 10 kHz. In contrast, at a pulse energy of 30 μJ, a larger final depth is only achieved for repetition rates > 100 kHz.

In summary, high pulse repetition rates can be used to reduce the processing time if structuring requires only a low number of pulses, e.g. in the initial phase of the drilling process. In this case, the hole geometry is independent of the repetition rate. Nevertheless, for deep drilling, an increase of the pulse repetition rate has a significant influence on the hole shape formation in ultrashort pulse drilling. Particle shielding can reduce the drilling rate for repetition rates of several kHz and above. The main influence on the hole shape, however, can be attributed to heat accumulation, especially for repetition rates of several hundred kHz. The rise of the average temperature at the ablation spot from pulse to pulse, which is caused by residual heat, leads to increased generation of melt and enhanced ablation, especially at the hole walls. Therefore, a widening of the hole diameter and the development of a multitude of large indentations and branches along the entire hole depth can be observed. In comparison to low repetition rates (< 10 kHz) the duration of the drilling process is prolonged and a significantly larger final depth can be achieved. Nevertheless, this is connected with the drawback of a wider hole with rough, bumpy sidewalls and significantly increased burr at the surface due to the expulsion of molten material. The formation of melt layers inside the capillary and an extended heat affected zone has to be considered in this case as well.

5.3 Analysis of the Laser-generated Plasma

For an investigation of the laser-induced plasma, the plasma luminescence is imaged during the drilling process. Due to the scattering of the hole walls, only luminescence from above the sample surface can be received. An additional camera with integrated image intensifier (Stanford Computer Optics 4 Picos) is implemented in the imaging setup as shown in fig. 5.9. A dichroic mirror separates the light for trans-illumination at
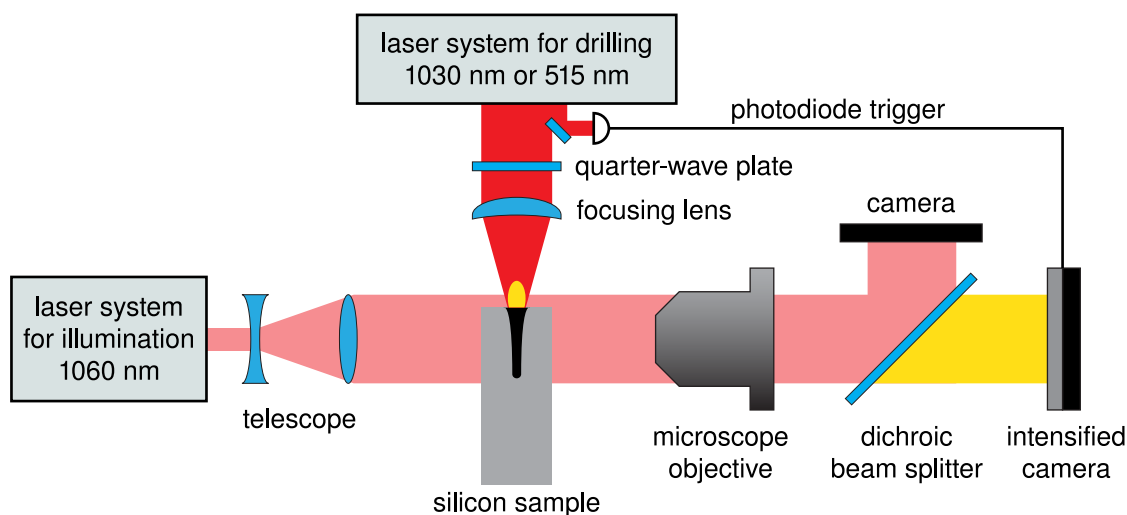

Fig. 5.9: Imaging setup for capturing the plasma luminescence during laser drilling with an additional intensified camera.

1060 nm from the broadband plasma luminescence. The image amplification enables a time-resolved detection of the plasma even at a low intensity. The minimal exposure time and according time resolution is 200 ps. The time of exposure is set by the internal delay generator of the camera and triggered to the incident pulse via a photodiode signal. The accuracy is approximately 1 ns due to the electronic jitter of the system. In this experiment, the drilling laser with a pulse duration of 8 ps (FWHM) is focused to the sample surface with a lens of 100 mm focal length. Laser wavelengths of 1030 nm and 515 nm are under investigation. Due to the low acquisition rate of the camera, a new irradiation for every time step of the plasma evolution is required which therefore does not allow for in-situ imaging. The experiments are carried out at atmospheric pressure and a pulse repetition rate of 50 Hz. First, the temporal evolution of the plasma is studied using the shortest exposure time of 200 ps. In a second study, the complete expansion of the plasma is captured in one image with a long exposure time of ca. 5 µs.

5.3.1 Temporal Evolution of the Plasma Expansion

The temporal evolution of the plasma above the surface, its movement and expansion, shows a characteristic behavior for both wavelengths, 1030 nm and 515 nm, and hole depths up to 100 μm, i.e. in the initial phase of the drilling process. Fig. 5.10 displays a typical example of the plasma evolution for a hole with a depth of 50 μm drilled with a pulse energy of 125 μJ at 1030 nm. The intensity of the luminescence is normalized for each image and plotted in a logarithmic scale. Already directly after the laser pulse, at a time of 1 ns, plasma luminescence can be observed at the surface. This plasma originates from the first step of the ablation process with thermionic emission of electrons and fast sublimation [17, 63–66], see also section 1.2. The plasma then moves upwards, separates from the surface and also increases in size. After approximately 100 ns, the plasma area is significantly enlarged and again begins at the sample surface. This can be attributed to a second phase of material removal by the delayed processes of spallation or phase explosion [65, 66], which is then superimposed with the existing plasma.
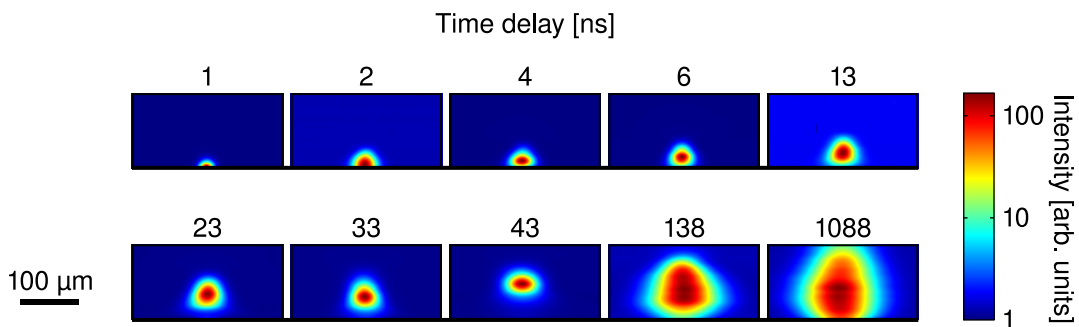
Fig. 5.10: Evolution of the plasma above the surface for a hole with 50 μm depth. Drilling is performed with a pulse energy of 125 μJ (fluence of 40 J/cm^2) at a wavelength of 1030 nm. The luminescence intensity is normalized for each image and plotted in a logarithmic scale.

Fig. 5.11 shows a corresponding quantitative analysis of the movement of the luminescence center. In this example, the drilling laser has a pulse energy of 60 μJ at a wavelength of 515 nm and the hole depth is ca. 35 μm. In the first 10 ns, the plasma shows a linear increase of the distance z_{plasma} to the surface with a constant vertical velocity v_{plasma} according to

$$z_{plasma} = v_{plasma} \cdot t. \tag{5.3}$$

This undisturbed expansion can be attributed to the high pressure of the material vapor in comparison to the ambient atmosphere [1, 65].

Fig. 5.11: Movement of the center of the plasma luminescence during plasma plume expansion for drilling at 515 nm with a pulse energy of ca. 60 μJ (fluence of ca. 40 J/cm²). The hole depth in this example is ca. 35 μm. During the first 10 ns a linear movement is observed according to equation 5.3 and afterwards a nonlinear increase of the distance according to equation 5.4.

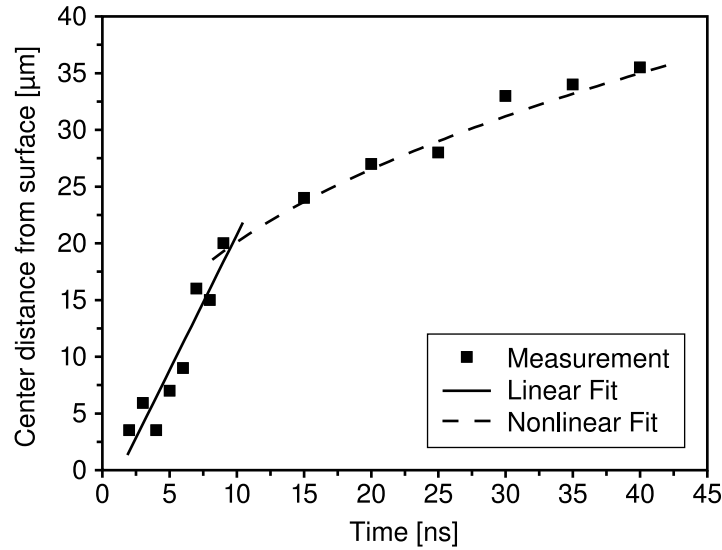After approximately 10 ns the pressure of the vapor decreases due to the expansion of the plasma plume. Hence, the velocity decreases. The vertical movement of the center of the plasma plume in this phase can be described by

$$z_{\mathrm{plasma}} \propto t^{2/5}, \tag{5.4}$$

similar to Sedov's theory for the expansion of the laser-induced shock-wave [1, 2, 65].

The velocity derived from the linear part of the plasma movement depends on the actual hole depth and is in the range of 7 km/s to 14 km/s at 1030 nm and 1 km/s to 3 km/s at 515 nm for a fluence of 40 J/cm² in both cases. These values are in agreement with velocities of the expanding shock-wave obtained for surface ablation of silicon [64] as well as metals [65, 147, 151]. With increasing depth of the hole, an increase of the plasma velocity is observed. The maximum velocity is found for a hole depth of ca. 40 μm. For larger depths, the velocity decreases again in combination with a decreasing time span of the linear expansion phase. This can be attributed to the longer propagation length

from the hole bottom to the surface. Eventually, only the nonlinear expansion can be observed above the surface for hole depths larger than ca. 100 μm.

5.3.2 Depth-dependence of the Plasma Expansion

The integrated plasma radiation above the surface is shown in fig. 5.12 in correlation with the simultaneously acquired hole shape for different numbers of applied pulses. Each of the images shows the complete plasma luminescence of one pulse with an integration time of 5 μs. The intensity of the luminescence is normalized with respect to the first image. Again, a similar behavior can be observed for drilling at 1030 nm and 515 nm. The example in fig. 5.12 illustrates the drilling process at 515 nm with a pulse energy of 60 μJ.
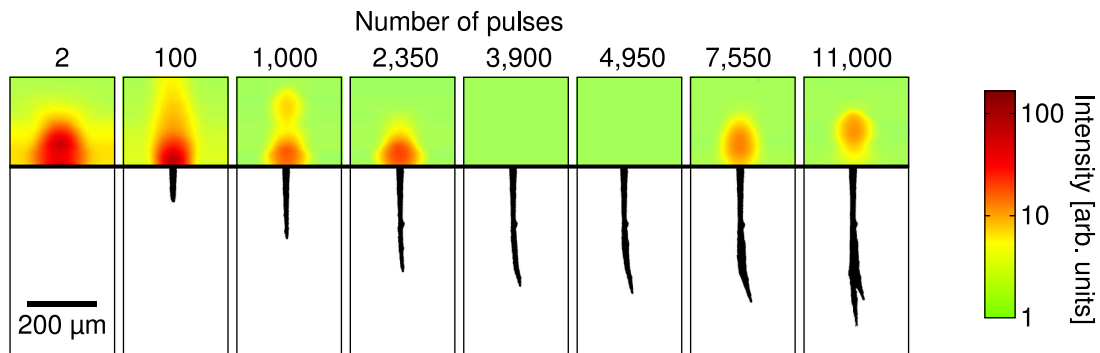
Fig. 5.12: Hole shape evolution and corresponding plasma luminescence for drilling with a pulse energy of 60 μJ (fluence of 40 J/cm^2) at a wavelength of 515 nm. The luminescence is plotted in a logarithmic scale.

At the beginning of the drilling process when ablation occurs close to the surface without lateral confinement by the sidewalls of the hole, the plasma luminescence shows a large lateral expansion. In the example here, this is ca. 150 μm for the first pulses although the entrance diameter of the hole is ca. 22 μm and therefore comparably smaller. After 100 pulses the lateral expansion of the plasma is significantly reduced compared to the beginning of the process but still larger than the hole diameter. Instead, the plasma extends further in the vertical direction. This can be attributed to the formation of the initial hole, which confines the plasma in lateral direction and acts like a nozzle on the flow of the material vapor. This nozzle effect can also explain the increased vertical velocity of the plasma movement, see section 5.3.1 above. A similar influence of

the hole capillary on the plasma expansion has also been observed for the drilling of diamond with pulses of 300 ps duration [2]. With a further increase of the hole depth, the intensity of the plasma luminescence decreases due to the lower material removal with decreasing ablation rate and due to the energy loss of the plasma by recombination and cooling during the propagation to the hole entrance. Furthermore, the plasma intensity is subject to fluctuations in the second phase of the drilling process, which do not occur during the initial process phase. These fluctuations can be attributed to predominant ablation in transverse direction, especially during the formation of an indentation or a hole bending. In some cases, the plasma plume at the surface completely disappears, see for example the period between 3,900 and 4,950 pulses in fig. 5.12. Here, the curved shape of the hole may prevent a direct ascent of the plasma from the hole bottom to the surface. Consequently, the energy of the plasma can be reabsorbed within the hole capillary and may contribute to the reshaping of the hole, e.g. partially changing the shape of the bend until subsequent pulses are no longer deflected in direction of the hole tip. After resume of drilling in forward direction, the plasma can propagate without obstruction and reappears at the surface, see the period from 7,550 to 11,000 pulses.

In summary, the plasma expansion for a shallow hole depth can be described similar to the expansion of the laser-induced shock-wave. The formation of the initial hole laterally confines the plasma plume but simultaneously increases the vertical expansion and velocity of the plasma movement. An analysis of the plasma expansion might therefore be suitable to determine the hole depth in the initial drilling phase. Such a method has also been demonstrated for drilling with ns-pulses [103]. The characteristics in the second phase of the drilling process, especially the formation of indentations and bendings, cause strong fluctuations of the plasma luminescence. Therefore, the observation of the plasma expansion above the sample surface also provides information about the current state of the hole shape formation.

5.4 Light Propagation inside a Laser-drilled Hole

The influence of the hole channel on the pulse propagation and intensity distribution inside the capillary is studied here by a numerical simulation. Different approaches exist for this task, from basic ray-optics to rigorous solutions of Maxwell's equations. Ray-tracing is a standard method for the evaluation of the light propagation through an

optical system [152, 153]. It can be applied to the problem here by assuming reflection of the light rays on the inner surface of the hole walls [40, 154]. However, this approach is very sensitive to the actual shape of the wall, since the wall curvature directly affects the deflection of each ray. In contrast, the Finite Difference Time Domain method (FDTD) is the most general approach enabling a direct integration of Maxwell's equations [155]. However, sampling with sub-wavelength resolution in the spatial domain in combination with appropriate temporal resolution is required. For the typical hole size with a depth of a few hundred microns, this results in an extensive amount of data points and considerable computing time. An alternative to the previously mentioned approaches is the Beam Propagation Method (BPM) [153, 156]. It relies on the slowly varying envelope approximation and therefore a low refractive index contrast and limited angle of propagation. Nevertheless, this method can be applied for the comparably high refractive index difference between silicon and air by implementing a gradual transition of the refractive index at the hole boundary. A comparison of the FDTD and the BPM simulation of the light propagation in a typical laser-drilled hole shows a good qualitative agreement, see appendix C, p. 109. Accordingly, BPM simulations allow a meaningful interpretation of the light propagation inside a laser-drilled hole.

In general, all these methods provide suitable simulations of a monochromatic, continuous wave light field. Ultrashort laser pulses, on the other hand, have a certain temporal width and corresponding broad spectral bandwidth. Nevertheless, pulses with a duration $\tau_{\mathrm{FWHM}} \approx 8\,\mathrm{ps}$ have a narrow spectral bandwidth of ca. 0.2 nm at a wavelength of 1030 nm. The spatial pulse length is $c \cdot \tau_{\mathrm{FWHM}} \approx 2.4\,\mathrm{mm}$, where c is the speed of light, which is much larger than the typical hole depth. Therefore, the simulations can still be used as a first, qualitative approximation of the light propagation inside a microhole.

In the following, the light propagation and resulting intensity distribution is evaluated by BPM simulations. The simulations here are performed in the two-dimensional image plane corresponding to the section of the hole as observed by the in-situ imaging. The propagation direction is denoted as z and the transverse direction as x. The hole boundary is derived from the hole silhouette captured with the in-situ imaging setup. The initial electric field E at the surface ($z = 0$) has a Gaussian distribution and flat spatial phase with the maximum value normalized to 1. At a wavelength of 1030 nm, the refractive index of silicon is $n_{\mathrm{Si}} = 3.58$ with an extinction coefficient $k_{\mathrm{Si}} \approx 2 \cdot 10^{-4}$ [129]. In this case, the extinction coefficient only accounts for the linear absorption at this

wavelength and nonlinear absorption is neglected. This results in a comparably large absorption length of a few hundred micrometers, which enables an interpretation of the light propagation into the silicon with respect to the direction of ablation at the hole boundary. Inside the hole, a refractive index $n_{\text{hole}} = 1$ and negligible absorption ($k_{\text{hole}} = 0$) is assumed. The results of the simulations always show $|E|^2$ that is directly proportional to the intensity [157].

In a first step, the light propagation is simulated within the initial hole at the end of the first drilling phase with a depth of 100 µm. The hole boundary in the simulation is approximated from a real hole silhouette with respect to the typical dimension, curvature and taper. The example here represents a hole drilled at a fluence of 10 J/cm^2 after ca. 200 pulses with a diameter of 52 µm at the hole entrance and 16 µm at the hole bottom. The corresponding focal spot diameter of the laser beam at $z = 0$ µm is 30 µm. The images in figs. 5.13 (a)–(c) (upper row) display the complete intensity distribution within the hole and the figs. 5.13 (d)–(f) (lower row) show detailed cross-sections at the hole entrance ($z = 0$ µm) and at the hole bottom ($z = 100$ µm) for the respective images (a)–(c). The hole in fig. 5.13 (a) is perfectly symmetric without any deviation from the ideal shape. To investigate the effect of small defects in the symmetry of the sidewalls, the hole in fig. 5.13 (b) features a small, elliptical bulge on the left side of the hole wall at a depth of 50 µm, marked by a white arrow in fig. 5.13 (b). This bulge extends 0.75 µm into the capillary at a length of 6 µm. The effect is then compared to an indentation on the surface of the capillary at the same position and with similar size in fig. 5.13 (c).

In general, the hole acts like a hollow waveguide. The light is confined within the hole capillary, which leads to an increase of the intensity due the reduction of the hole diameter from the entrance to the hole bottom. The intensity distribution is also affected by a strong modulation from the interference of the central beam part with the reflected outer part of the beam. For the hole in fig. 5.13 (a), interference patterns occur for $z \approx 20$ µm with the transition of the funnel-shaped entrance to a hole channel with steeper sidewalls. Despite this modulation, the intensity profile at the hole bottom is still symmetrical, see also fig. 5.13 (d).

In fig. 5.13 (b), the bulge on the left sidewall leads to a redistribution of intensity from the left part of the hole channel to the right and an asymmetric interference pattern. This shift increases with the propagation distance. At a depth of 100 µm, the highest local intensity can be found at the right side of the hole opposite to the bulge, see fig. 5.13 (e).
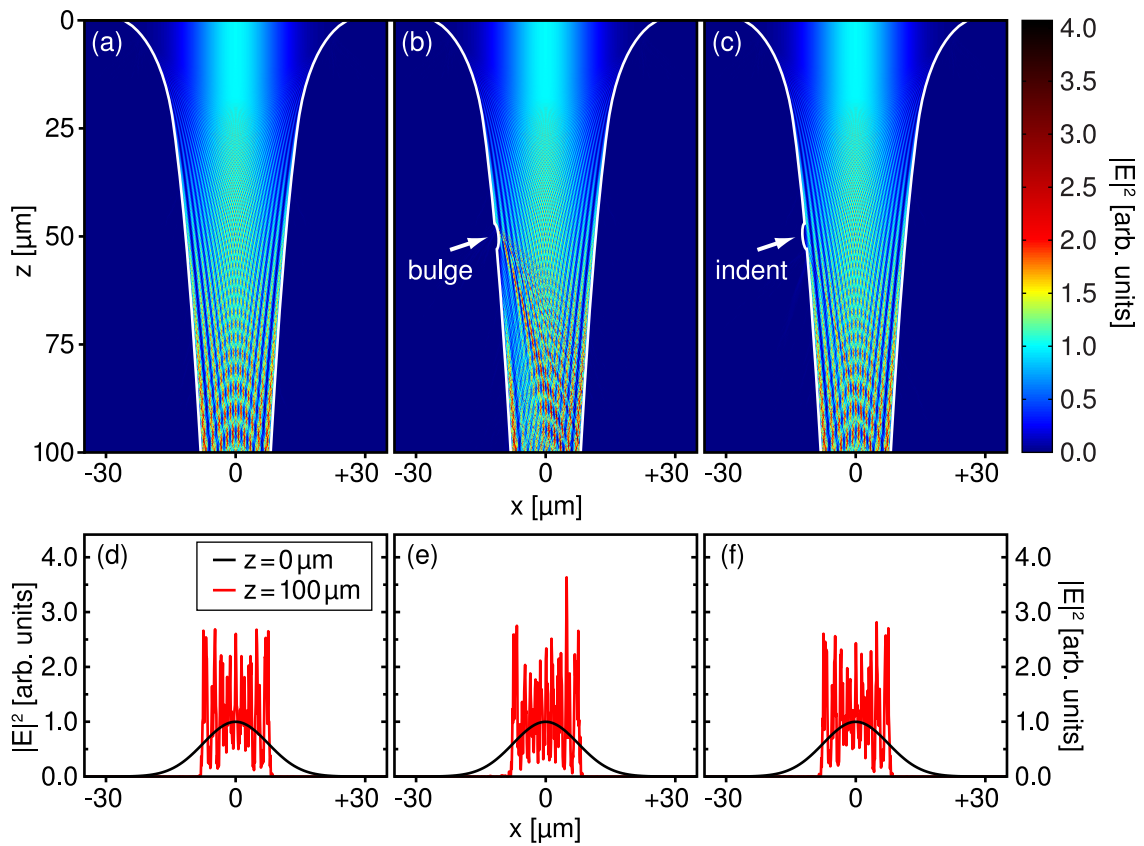
Fig. 5.13: BPM simulation of the light propagation inside a hole capillary with different types of perturbations along the sidewalls. The images in the upper row (a)-(c) show the complete distribution of $|E|^2$ with the outline of the hole in white. The graphs in the the lower row (d)-(f) depict the intensity profile at the hole surface $z = 0\,\mu m$ (black line) and at the hole bottom in a depth of $z = 100\,\mu m$ (red line).

The intensity under the bulge at the left side of the hole is reduced. Consequently, ablation at the right side of the hole would be enhanced. Although this is only a weak effect for a single pulse, an accumulation of several consecutive pulses may lead to a hole bending or the formation of a large cavity at the hole wall.

In comparison, an indentation on the sidewall of the hole as in fig. 5.13 (c) has only a marginal effect on the light propagation and resulting intensity distribution since it does not protrude into the direct beam path. Nevertheless, the lower edge of the indentation can affect the beam due to the inclination of the wall and cause a minor asymmetry of the intensity distribution, see fig. 5.13 (f).

Altogether, small perturbations on the hole walls with sub-micron extension into the hole capillary can lead to a change of the intensity distribution and an asymmetric ablation at the hole bottom. A surface imperfection may not necessarily cause a direct effect on the ablation in the vicinity of the structure. The effect may occur after further propagation, e.g. when the beam reaches the opposite hole wall. Therefore, the light propagation only influences the shape formation of deep holes. The initial hole in the first process phase is not affected by deformations due to its low depth. Hence, it has a reproducible shape which is determined by the incident intensity profile of the beam. However, imperfections on the walls of the initial hole can affect the further shape formation. Such imperfections, similar to the ones assumed in the simulations, can indeed be observed on the hole walls.
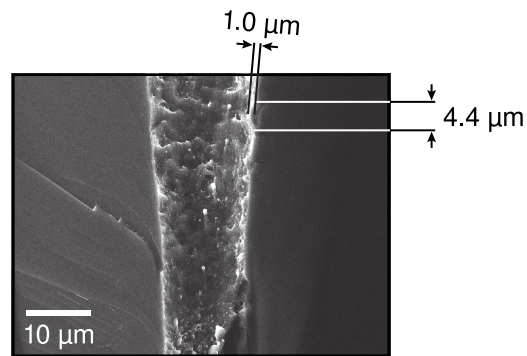
Fig. 5.14: Inner surface of a laser-drilled hole in silicon at a pulse energy of 125 μJ. The hole walls are covered with small bulges, humps and melt droplets.

Fig. 5.14 shows the interior of a typical drilling in silicon with bulges and droplets on the hole walls. Similar structures on the hole walls are observed in metals [89, 90]. The flow of the melt film can result in the shingle-type surface structure. The asymmetry can be attributed to an inherently nonuniform material removal by spallation or phase explosion. In addition, a slightly asymmetric intensity distribution of the laser can also cause a nonuniform ablation. A direct observation of these structures is not possible with the in-situ imaging technique, which only captures the outline of the hole silhouette.

In the following, the light propagation inside a deep hole (second process phase) is studied with special regard to bending and branching. In this case, the BPM simulations are based on a realistic hole geometry obtained from the silhouette for drilling at $10\,\mathrm{J/cm^2}$ with a focal spot diameter of ca. 26 μm (100 mm lens). The shape evolution of this particular example has been discussed in fig. 4.6 (c) of section 4.1.2. The simulations have been performed for the complete hole channel but only the lower part is shown here, see appendix C, p. 109, for an example of an entire hole.

Fig. 5.15: Detailed view of the light propagation inside a hole capillary during the formation of a hole bending. The outline of the hole is shown in white.
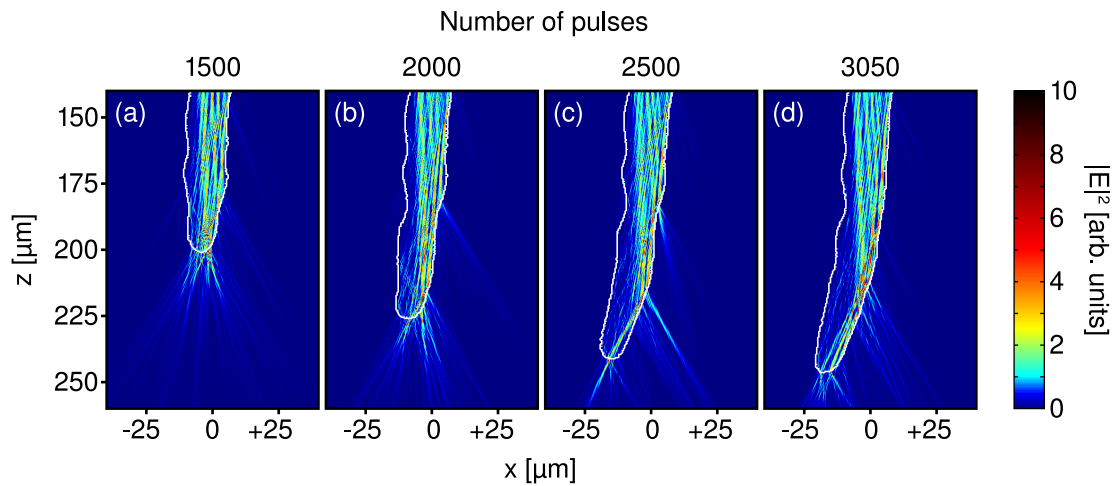
Different states of the hole bending with increasing curvature are shown in fig. 5.15. In this example, the laser beam is deflected from the right sidewall towards the hole bottom. The deflection increases with the evolution of the hole bending, see especially the direction of light propagation inside the silicon material in figs. 5.15 (b) and (c). The interaction of light propagation and shape formation leads to a self-amplifying process which gradually increases the hole bending. Even for the highest curvature in fig. 5.15 (d) a guiding of the light to the hole tip can be observed. However, with increasing bending, the light is distributed over a larger area along the curvature of the hole, especially on the lower right sidewall. This leads to a decrease of the effective fluence at the hole bottom, resulting in a lower ablation rate and potential stop of forward drilling. Energy coupling to the curved hole wall is enhanced compared to the otherwise steep walls of the hole channel, see also the light propagation into the silicon at right sidewall in figs. 5.15 (c) and (d). This can cause an enhanced ablation of curved hole walls and therefore a change of the hole geometry.

The effect of reshaping during a period without forward drilling is shown in fig. 5.16. The hole wall on the right side is ablated, see fig. 5.16 (a) to (c). The smooth bending becomes a sharp bend with a steep wall and flat base. Thus, the deflection of light towards the hole tip is diminished while the coupling of light to the silicon increases in the flattened region, see the increasing light propagation inside the silicon in fig. 5.16 (b) and (c). Again, this effect is also self-amplifying. A flatter hole ground leads to better

energy coupling to the material and enhanced ablation towards a steeper sidewall and even flatter hole ground. Eventually, absorption occurs mainly in the flat region of the hole, see fig. 5.16 (c). Starting from here, a new branch of the hole is formed. The shape of the hole has changed in such a way that light is only directed to this new branch while there is almost no deflection to the old branch. This is in good agreement with the observed hole formation, which shows no further expansion of an old branch once a new one starts to form.
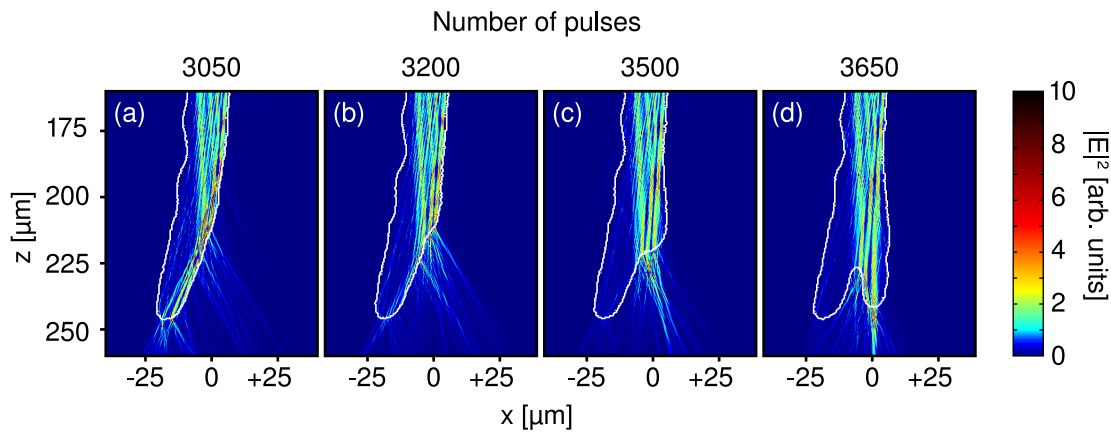
Fig. 5.16: Detailed view of the light propagation inside a hole capillary during the reshaping of the hole bending. The outline of the hole is shown in white.

Finally, it should be pointed out that beside the limitations of the simulation method as described above there are further restrictions which have to be considered in the interpretation of the results. This is for example the evaluation in only two dimensions, which does not account for the complete three-dimensional hole volume. In addition, the simulations here are based on the observed outline of the hole geometry, especially in fig. 5.15 and fig. 5.16. This does not represent the real inner surface of the hole which interacts with the beam since this cannot be acquired by the in-situ imaging technique. Therefore, interaction with hole walls may not be treated correctly and may lead to an underestimation of the beam deflection in some cases, see e.g. the intensity distribution in fig. 5.15 (a) which would be expected to have a larger shift to the left side of the hole bottom in direction of the future hole bending. Furthermore, the hole geometry is smoothed for the simulation which neglects small surface features. Nevertheless, the hole geometry used here represents the principal confinement for the light propagation inside the hole capillary.

In summary, the simulations show a serious influence of the hole geometry on the light propagation. This effect can cause an asymmetric ablation without relying on additional processes, e.g. plasma deflection [25, 37]. Furthermore, the simulated light propagation is in good agreement with the observed, self-amplifying formation of a hole bending as well as the reshaping process.

5.5 Conclusion

Previous investigations assumed the laser-induced plasma, which can cause ablation of the hole walls, to have the most significant effect on the formation of the hole shape in deep drilling [2, 19, 24, 34, 35, 91], see also the Hirschegg-model in section 2.2. This plasma effect can be prevented by a reduction of the ambient pressure [34, 124]. In this study, it has been shown that indentations on the hole walls still occur at a pressure reduction down to 10^{-2} mbar, even though smaller in size. Bending and branching of the hole occurs in the same manner as for atmospheric pressure (10^3 mbar). Therefore, ablation by the plasma cannot be the main cause of this hole shape formation. On the other hand, the plasma expansion is significantly influenced by the hole shape. In case of a hole bending, for example, the plasma may not even reach the sample surface. Although scattering of the incident pulse on ablation particles may affect the hole formation at high repetition rates (> 100 kHz), it is superimposed by heat accumulation that causes substantial melting and influences the hole shape, especially the hole diameter, due to enhanced ablation from the melt as well as melt expulsion.

Simulations of the light propagation inside the hole capillary show that already small bulges at the hole walls can interfere with the pulse propagation and cause an asymmetric intensity distribution at the hole bottom. The evolution over multiple pulses can then result in the formation of large indentations or hole bendings. The light guiding effect within the hole capillary can also explain the self-amplifying formation of a hole bending with continuously increasing curvature. The assumed change of the light propagation during a reshaping phase, which is essential for the resume of forward drilling, is also supported by the simulations. Therefore, the light propagation represents the principal reason for the hole shape formation. Particle depositions inside the hole capillary can restrain the pulse propagation. This effect is mainly responsible for the final stop of the drilling process.

Summary and Outlook

A direct visualization of ultrashort pulse laser drilling has been realized in an opaque material for the first time. Here, crystalline silicon was used as sample material for the in-situ imaging of the hole shape evolution during percussion drilling. Due to the similar ablation properties of semiconductors and metals in the ultrashort pulse regime, the results and conclusions of the present work are valid for both material classes. The in-situ observation allowed to trace the formation of individual and statistically occurring hole shape features, especially indentations on the sidewalls and the bending of the hole. Therefore, the complete formation of an ultrashort pulse laser-drilled hole in an opaque material has been observed and systematically analyzed for the first time. Apart from parameter-specific effects and dependencies, the drilling process is characterized by three process phases:

1. The initial hole is excavated during the first few hundred pulses. This phase shows the highest ablation rate and the shape of the hole is determined by the incident intensity profile.

2. In the further process, the drilling rate decreases during the formation of a deep hole. The growth of the hole depth is subject to fluctuations, including intermediate periods of significantly reduced or even completely halted forward drilling. These periods occur more often and with longer duration for an increasing number of applied pulses. In the second process phase, ablation increasingly occurs in transverse direction, forming indentations, larger cavities and additional hole branches. In addition, bending of the hole channel can be observed. During periods with constant or only marginally changing hole depth, ablation can reshape the hole until drilling may resume in forward direction. All these processes occur statistically, resulting in a substantial variation of the final hole shape.

3. In the final third phase, no further increase of the hole depth takes place. The hole volume may still increase due to widening of the hole diameter and the formation of additional branches, indentations or similar changes of the hole shape.

The actual hole depth and hole shape affects the expansion of the laser-generated plasma. An observation of the plasma luminescence above the surface of opaque materials could therefore enable a direct process monitoring.

The pulse energy has been identified as the fundamental process parameter for deep drilling, determining the maximum achievable hole depth largely independent of the focusing conditions and the actual fluence. It has been shown, that the deposition of ablation particles inside the hole has a significant influence on the duration of the drilling process and the achievable depth. This debris can obstruct the hole capillary and restrain the pulse propagation to the hole bottom. It has been demonstrated, that the particle debris in the hole channel can be diminished by a reduction of the ambient pressure. The hole shape formation at high repetition rates of several hundred kHz is mainly influenced by heat accumulation. This effect leads to enhanced ablation and a prolonged process duration with a larger final depth compared to low repetition rates. However, this is accompanied by an enlarged hole diameter and extensive melt production, which accordingly reduce the achievable precision.

The light propagation inside the hole channel has been identified as the main influence on the hole shape formation in this work. Deviations from the ideal geometry like bending and indent formation are induced by beam deflections on hole wall imperfections, especially small bulges. These initial imperfections may originate from asymmetric ablation due to variations of the intensity profile from pulse to pulse as well as an asymmetric melt flow or expulsion. Based on the interpretation of the light propagation, self-amplifying effects like hole bending with a continuously increasing deflection can be explained due to the guiding of the laser beam inside the hole channel. Furthermore, the influence of the focus position on the hole shape has been demonstrated. An optimized focus position below the sample surface can achieve a significantly larger hole depth. Again, this can be successfully explained by the light propagation inside the tapered hole. Moreover, this study shows, that the reshaping of the hole geometry during intermediate periods of constant hole depth is essential for the further continuation of forward drilling. The change of the hole shape modifies the light propagation inside the hole capillary and improves the conditions for ablation at the hole bottom.

With the first complete observation of the ultrashort pulse drilling process in an opaque material, as realized in this work, the essential mechanisms and parameters for the hole shape formation have been identified. The results of this work show that a fundamental improvement of quality and precision in ultrashort pulse drilling requires a control of the light propagation inside the hole. This can be achieved, for example, with advanced drilling techniques that move the focus position during drilling, e.g. trepanning or helical drilling, which proved capable of realizing high quality microholes [38, 44]. In this case, the hole diameter is larger than the focal spot size, which reduces the effect of the hole channel on the pulse propagation. However, the fabrication of holes with small diameters, especially below $50\,\mu m$, using these techniques is challenging and requires further improvement. Alternatively, the drilling parameters could be adapted dynamically during the process to remove or compensate asymmetries already in existence, e.g. by a variation of the pulse energy with increasing depth. Since the hole shape deviations usually evolve over several pulses, they can possibly be suppressed by actively or passively changing the conditions for the pulse propagation and for ablation during drilling. This might be realized by a continuous, highly frequent movement of the focus position or by a modulation of the pulse repetition rate (pulse bursts). Furthermore, the beam deflection could be compensated by an on-line control of the pulse propagation, e.g. by adaptive beam shaping in combination with on-line process monitoring.

Further investigations for an enhanced quality of the drilling process should involve the formation of the initial imperfections, which then influence the pulse propagation inside the hole. Therefore, it might be necessary to concentrate on the laser ablation process itself with special regard to the crater shape of a single pulse. An experimental study could be complemented by molecular dynamic simulations with an appropriate number of atoms to reproduce real-world conditions. These simulations became available in recent years due to the rapid increase in computational power [72, 158]. In addition, the actual influence of the initial imperfections on the hole shape needs to be further understood. The necessary systematic investigations might be enhanced by extending the current in-situ imaging setup towards a tomographic hole shape visualization. Alternatively, a three-dimensional shape reconstruction could be realized with the advancing technology of x-ray microtomography [159] that is also capable of visualizing the interior of the hole.

The results of this work are crucial for the realization of high quality micro-drillings in numerous applications. For example, via holes in silicon wafers could enable a three-dimensional integration of microelectronics by stacking of functional layers, which are connected through these holes [160]. In addition, high quality micro-drillings are required for injection nozzles in combustion engines and ink-jet printing [8] as well as high harmonics generation [161] but also as miniature vent holes for injection molding [162]. Beyond drilling itself, the shape formation mechanisms that were under investigation in this work are relevant for every ultrashort pulse laser micro-structuring process with high aspect ratio.

Appendix

A Simulation of Ultrashort Pulse Absorption in Copper

To illustrate the evolution of the electron temperature T_{el} and lattice temperature T_{lat} for ultrashort pulse irradiation of a metal, fig. 1.1 on p. 7 shows a numerical simulation based on the Two-Temperature-Model according to equation 1.1. In this example, copper is chosen as the sample material. Temperature dependent parameters of the electron heat capacity C_{el} and electron thermal conductivity κ_{el} are included in the model. Since the heat conduction is mainly mediated by the electrons, the thermal conductivity of the lattice subsystem is neglected [4]. A constant heat capacity of the lattice is assumed.

The simulation is realized as a one-dimensional calculation. The coordinate z denotes the depth perpendicular to the surface. Here, a homogeneous illumination is assumed. This is a good approximation of the typical irradiation conditions in laser micromachining with a low absorption depth (few nanometers for a metal) in comparison to the diameter of the laser spot (several micrometers). At the sample surface negligible heat losses are assumed. This is represented by the Neumann boundary condition at $z = 0$ with

$$\left.\frac{\partial T_{el}}{\partial z}\right|_{z=0} = \left.\frac{\partial T_{lat}}{\partial z}\right|_{z=0} = 0. \tag{A.1}$$

For a sample thickness significantly larger than the heat affected zone, a constant temperature at $z = z_{max}$ can be assumed, which is represented by the Dirichlet boundary condition

$$T_{el}(z_{max}) = T_{lat}(z_{max}) = T_0, \tag{A.2}$$

where $T_0 = 295\,\text{K}$ is the initial temperature. The heat source Q for a laser pulse with

Gaussian temporal intensity profile with a duration τ and a fluence F is given by

$$Q(z, t) = \alpha \left(1 - R\right) \sqrt{\frac{2}{\pi}} \frac{F}{\tau} \cdot \exp\left[-2\frac{t^2}{\tau^2}\right] \cdot \exp\left[-\alpha z\right] \qquad \text{(A.3)}$$

in which α is the absorption coefficient and R the reflectivity of the sample surface. The effectively absorbed fluence is therefore given by $(1 - R) \cdot F$.

The numerical calculation is implemented as an explicit finite difference method [163] solved on a grid with $z_{\text{max}} = 400\,\text{nm}$ and 0.5 nm resolution. A summary of the parameter descriptions used in the Two-Temperature-Model simulation together with the specific values for copper can be found in table A.1.

Tab. A.1: Parameters of the Two-Temperature-Model simulation in copper.

specific heat capacity of the electrons [164, 165]
$$C_{\text{el}} = C_{\text{el},0} \cdot T_{\text{el}}$$
$$\text{with } C_{\text{el},0} = 96.6\,\frac{\text{J}}{\text{m}^3\,\text{K}^2}$$

thermal conductivity of the electrons [68, 166]
$$\kappa_{\text{el}} = \kappa_{\text{el},0} \cdot \frac{\xi_B\,T_{\text{el}}}{\xi_A\,T_{\text{el}}^2 + \xi_B\,T_{\text{lat}}}$$
$$\text{with } \kappa_{\text{el},0} = 400\,\frac{\text{W}}{\text{m}\,\text{K}}$$
$$\xi_A = 1.75 \cdot 10^7\,\text{K}^{-2}\,\text{s}^{-1}$$
$$\xi_B = 1.98 \cdot 10^{11}\,\text{K}^{-1}\,\text{s}^{-1}$$

specific heat capacity of the lattice [165]
$$C_{\text{lat}} = 3.5 \cdot 10^6\,\frac{\text{J}}{\text{m}^3\,\text{K}}$$

thermal conductivity of the lattice [4]
$$\kappa_{\text{lat}} \approx 0\,\frac{\text{W}}{\text{m}\,\text{K}}$$

electron-phonon coupling coefficient [167, approximation from fig. 3]
$$G = \begin{cases} 0.55 \cdot 10^{17}\,\frac{\text{W}}{\text{m}^3\,\text{K}} & \text{for } T_{\text{el}} < 3{,}000\,\text{K}, \\ 4.54 \cdot 10^{13}\,\frac{\text{W}}{\text{m}^3\,\text{K}^2} \cdot T_{\text{el}} - 0.81 \cdot 10^{17}\,\frac{\text{W}}{\text{m}^3\,\text{K}} & \text{for } 3{,}000\,\text{K} \leq T_{\text{el}} \leq 15{,}000\,\text{K}, \\ 6.00 \cdot 10^{17}\,\frac{\text{W}}{\text{m}^3\,\text{K}} & \text{for } T_{\text{el}} > 15{,}000\,\text{K} \end{cases}$$

absorption coefficient [168]
$$\alpha = 8 \cdot 10^7\,\text{m}^{-1}$$

B Simulation of Ultrashort Laser Pulse Absorption in Silicon

To evaluate the energy deposition and temperature increase caused by an ultrashort laser pulse inside a silicon sample, the electron and lattice temperature evolution is simulated using the Two-Temperature-Model (TTM), see section 1.1. In addition, the development of the free electron density during the irradiation that influences the optical and thermal properties is taken into account. The simulation is performed in one dimension with the coordinate z denoting the depth perpendicular to the sample surface. Therefore, a homogeneous irradiation is assumed.

The basic equations of the TTM for the electron temperature $T_{\mathrm{el}}(t, z)$ and lattice temperature $T_{\mathrm{lat}}(t, z)$ are

$$C_{\mathrm{el}} \frac{\partial T_{\mathrm{el}}}{\partial t} = \frac{\partial}{\partial z} \left(\kappa_{\mathrm{el}} \cdot \frac{\partial}{\partial z} T_{\mathrm{el}} \right) - G \cdot \left(T_{\mathrm{el}} - T_{\mathrm{lat}} \right) + Q \tag{B.1}$$

$$C_{\mathrm{lat}} \frac{\partial T_{\mathrm{lat}}}{\partial t} = \frac{\partial}{\partial z} \left(\kappa_{\mathrm{lat}} \cdot \frac{\partial}{\partial z} T_{\mathrm{el}} \right) + G \cdot \left(T_{\mathrm{el}} - T_{\mathrm{lat}} \right) \tag{B.2}$$

with the electron and lattice heat capacity C_{el} and C_{lat} respectively. κ_{el}, κ_{lat} denote the thermal conductivity and G is the electron-phonon coupling coefficient. Neumann boundary conditions are used at the surface $z = 0$ and Dirichlet boundary conditions at $z = z_{\mathrm{max}}$:

$$\left. \frac{\partial T_{\mathrm{el}}}{\partial z} \right|_{z=0} = \left. \frac{\partial T_{\mathrm{lat}}}{\partial z} \right|_{z=0} = 0 \, \mathrm{K} \tag{B.3}$$

$$T_{\mathrm{el}}(z_{\mathrm{max}}) = T_{\mathrm{lat}}(z_{\mathrm{max}}) = T_0 = 295 \, \mathrm{K}. \tag{B.4}$$

The heat source Q accounts for linear and free carrier absorption as well as the nonlinear

contribution by two photon absorption according to [52]

$$Q = (1 - R)\alpha I + (1 - R)\Theta n_{\mathrm{el}} I + (1 - R)^2 \sigma_2 I^2. \tag{B.5}$$

R denotes the reflectivity at the surface. α is the coefficient for linear absorption. Θ represents the free carrier absorption coefficient and σ_2 is the two photon absorption coefficient. The free carrier density is denoted as n_{el}. The distribution of the laser intensity I within the sample is determined by

$$\frac{\partial I}{\partial z} = -\alpha I - \Theta n_{\mathrm{el}} I - \sigma_2 I^2 \tag{B.6}$$

with the initial condition $I(z = 0) = I_{\mathrm{pulse}}$ [64]. In this example, a Gaussian pulse with a duration τ and a fluence F is assumed according to

$$I_{\mathrm{pulse}}(t) = \sqrt{\frac{2}{\pi}} \frac{F}{\tau} \cdot \exp\left[-2\frac{t^2}{\tau^2}\right]. \tag{B.7}$$

The ionization process due to the laser irradiation is described by a rate equation for the free electron density including the linear and two photon absorption as well as impact ionization and Auger recombination

$$\frac{\partial n_{\mathrm{el}}}{\partial t} = \frac{(1 - R)\alpha I}{\hbar\omega} + \frac{(1 - R)^2 \sigma_2 I^2}{2\hbar\omega} + \delta \cdot n_{\mathrm{el}} - \gamma_{\mathrm{Auger}} \cdot n_{\mathrm{el}}^3 \tag{B.8}$$

for a laser field with angular frequency ω [59]. The coefficient δ represents the impact ionization and γ_{Auger} describes the Auger recombination of the free carriers. $\hbar$ denotes the reduced Planck constant. The initial free carrier density is calculated from

$$n_{\mathrm{el},0} = \frac{(2\pi m_e k_B T_0)^{\frac{3}{2}}}{4\pi^3 \hbar^3} \cdot \exp\left[\frac{E_{\mathrm{gap}}}{2 k_B T_0}\right] \tag{B.9}$$

with the Boltzmann constant k_B, the electron mass m_e and the band gap energy E_{gap} [59]. The free electron density then defines the optical parameters, especially the reflectivity R and the absorption coefficient α. Here, the dielectric function of silicon ϵ_{Si}

is described as

$$\text{Re}(\epsilon_{\text{Si}}) = 1 + \left(\text{Re}(\epsilon_{\text{Si},0}) - 1\right)\left[1 - \frac{n_{\text{el}}}{n_{\text{val}}}\right] - \frac{n_{\text{el}}}{n_{\text{crit}}}\left[1 + \left(\frac{\Gamma}{\omega}\right)^2\right]^{-1} \tag{B.10}$$

$$\text{Im}(\epsilon_{\text{Si}}) = \text{Im}(\epsilon_{\text{Si},0})\left[1 - \frac{n_{\text{el}}}{n_{\text{val}}}\right] + \frac{n_{\text{el}}}{n_{\text{crit}}}\frac{\Gamma}{\omega}\left[1 + \left(\frac{\Gamma}{\omega}\right)^2\right]^{-1} \tag{B.11}$$

which accounts for the effect of state and band filling as well as interaction with free electrons according to the Drude model [130, 169]. $\epsilon_{\text{Si},0}$ represents the initial dielectric function of unexcited silicon. n_{val} denotes the valence band electron density and $n_{\text{crit}} = m_e\epsilon_0\omega^2/e^2$ is the critical electron density for optical breakdown, where ϵ_0 is the dielectric constant and e the elementary charge. Γ is the damping parameter in the Drude model. In an intermediate step, the refractive index n_{Si} and the extinction coefficient k_{Si} is calculated from the dielectric function ϵ_{Si} by

$$n_{\text{Si}}^2 = \frac{1}{2}\left[\sqrt{\text{Re}(\epsilon_{\text{Si}})^2 + \text{Im}(\epsilon_{\text{Si}})^2} + \text{Re}(\epsilon_{\text{Si}})\right] \tag{B.12}$$

$$k_{\text{Si}}^2 = \frac{1}{2}\left[\sqrt{\text{Re}(\epsilon_{\text{Si}})^2 + \text{Im}(\epsilon_{\text{Si}})^2} - \text{Re}(\epsilon_{\text{Si}})\right] \tag{B.13}$$

Afterwards, the reflectivity R at perpendicular incidence and the absorption coefficient α can be obtained from

$$R = \frac{\left(n_{\text{Si}} - 1\right)^2 + k_{\text{Si}}^2}{\left(n_{\text{Si}} + 1\right)^2 + k_{\text{Si}}^2} \tag{B.14}$$

$$\alpha = 2\frac{\omega}{c}k_{\text{Si}} \tag{B.15}$$

with the constant c denoting the speed of light.

The parameters and specific constants to simulate the temperature evolution in silicon are summarized with respective references in tables B.1, B.2, and B.3.

Tab. B.1: Material parameters of silicon for the TTM simulation.

specific heat capacity of the electrons [52]

$$C_{\text{el}} = \tfrac{3}{2} k_B \, n_{\text{el}}$$

thermal conductivity of the electrons [52]

$$\kappa_{\text{el}} = \frac{2 k_B^2 \, \mu_{\text{el}} \, n_{\text{el}} \, T_{\text{el}}}{e}$$
$$\text{with } \mu_{\text{el}} = 0.015 \tfrac{\text{m}^2}{\text{V s}}$$

specific heat capacity of the lattice [52, 170]

$$C_{\text{lat}} = 1.978 \cdot 10^6 \tfrac{\text{J}}{\text{m}^3 \text{K}} + 3.54 \cdot 10^2 \tfrac{\text{J}}{\text{m}^3 \text{K}^2} \cdot T_{\text{lat}} - 3.68 \cdot 10^6 \tfrac{\text{JK}}{\text{m}^3} \cdot T_{\text{lat}}^{-2}$$

thermal conductivity of the lattice [52, 171]

$$\kappa_{\text{lat}} = 1.585 \cdot 10^5 \tfrac{\text{WK}^{0.23}}{\text{m}} \cdot T_{\text{lat}}^{-1.23}$$

electron-phonon coupling coefficient

$$G = \frac{C_{\text{el}}}{\tau_{\text{el}}}$$

electron cooling time [172, 173]

$$\tau_{\text{el}} = \tau_{\text{el},0} \left[1 + \left(\frac{n_{\text{el}}}{n_{\text{crit}}} \right)^2 \right]$$

electron cooling time coefficient [173]

$$\tau_{\text{el},0} = 240 \, \text{fs}$$

Tab. B.2: Optical and absorption parameters of silicon at a wavelength of 1030 nm.

wavelength

$$\lambda = 1030\,\text{nm}$$

electric field angular frequency

$$\omega = 2\pi \frac{c}{\lambda}$$

initial refractive index [129]

$$n_{\text{Si},0} = 3.57809$$

initial extinction coefficient [129]

$$k_{\text{Si},0} = 1.9765 \cdot 10^{-4}$$

initial dielectric function

$$\text{Re}(\epsilon_{\text{Si},0}) = n_{\text{Si},0}^2 - k_{\text{Si},0}^2$$
$$\text{Im}(\epsilon_{\text{Si},0}) = 2 n_{\text{Si},0}\, k_{\text{Si},0}$$

free carrier absorption coefficient [174]

$$\Theta = 5 \cdot 10^{-22}\,\text{m}^2$$

two photon absorption coefficient [52]

$$\sigma_2 = 2 \cdot 10^{-11}\,\tfrac{\text{m}}{\text{W}}$$

impact ionization coefficient [52]

$$\delta = 3.6 \cdot 10^{10}\,\text{s}^{-1} \cdot \exp\left[-\tfrac{3}{2} \cdot \frac{E_{\text{gap}}}{k_B\, T_{\text{el}}} \right]$$

energy of the band gap [41]

$$E_{\text{gap}} = 1.87 \cdot 10^{-19}\,\text{J}$$

coefficient of Auger recombination [175]

$$\gamma_{\text{Auger}} = 2.8 \cdot 10^{-43}\,\tfrac{\text{m}^3}{\text{s}}$$

valence band electron density [53]

$$n_{\text{val}} = 5 \cdot 10^{28}\,\text{m}^{-3}$$

Drude model damping parameter [130]

$$\Gamma = 1 \cdot 10^{15}\,\text{s}^{-1}$$

pulse duration (FWHM)

$$\tau_{\text{FWHM}} = \sqrt{2\ln 2}\,\tau = 8\,\text{ps}$$

incident fluence

$$F = 1\,\text{J/cm}^2$$

Tab. B.3: Optical and absorption parameters of silicon at a wavelength of 515 nm.

wavelength
$$\lambda = 515\,\text{nm}$$

electric field angular frequency
$$\omega = 2\pi\tfrac{c}{\lambda}$$

initial refractive index [129]
$$n_{\text{Si},0} = 4.22244$$

initial extinction coefficient [129]
$$k_{\text{Si},0} = 6 \cdot 10^{-2}$$

initial dielectric function
$$\text{Re}(\epsilon_{\text{Si},0}) = n_{\text{Si},0}^2 - k_{\text{Si},0}^2$$
$$\text{Im}(\epsilon_{\text{Si},0}) = 2 n_{\text{Si},0}\, k_{\text{Si},0}$$

free carrier absorption coefficient [174]
$$\Theta = 5 \cdot 10^{-22}\,\text{m}^2$$

two photon absorption coefficient [176]
$$\sigma_2 = 3.46 \cdot 10^{-10}\,\tfrac{\text{m}}{\text{W}}$$

impact ionization coefficient [52]
$$\delta = 3.6 \cdot 10^{10}\,\text{s}^{-1} \cdot \exp\left[-\tfrac{3}{2} \cdot \tfrac{E_{\text{gap}}}{k_B\, T_{\text{el}}}\right]$$

energy of the band gap [41]
$$E_{\text{gap}} = 1.87 \cdot 10^{-19}\,\text{J}$$

coefficient of Auger recombination [175]
$$\gamma_{\text{Auger}} = 2.8 \cdot 10^{-43}\,\tfrac{\text{m}^3}{\text{s}}$$

valence band electron density [53]
$$n_{\text{val}} = 5 \cdot 10^{28}\,\text{m}^{-3}$$

Drude model damping parameter [130]
$$\Gamma = 1 \cdot 10^{15}\,\text{s}^{-1}$$

pulse duration (FWHM)
$$\tau_{\text{FWHM}} = \sqrt{2\ln 2}\,\tau = 8\,\text{ps}$$

incident fluence
$$F = 1\,\text{J/cm}^2$$

C Comparison of BPM and FDTD Simulation

For the investigation of the pulse propagation on the hole shape evolution in section 5.4 on page 87ff., the Beam Propagation Method (BPM) is applied for a numerical simulation of the light propagation. This method relies on the slowly varying envelope approximation and is therefore limited to low propagation angles and a low refractive index contrast. In this study, the BPM is adapted to the refractive index contrast between air and silicon by implementing a gradual transition at the hole boundary. Still, a meaningful interpretation can only be given for holes with limited amount of bending. In particular, this excludes ablation in upwards direction as shown in the example of fig. 4.6 (d) or (e) on page 40. On the other hand, there are methods which allow a rigorous solution of Maxwell's equations and are not limited to these restrictions, e.g. the Finite Difference Time Domain (FDTD) method. However, this requires significantly higher computing time compared to the BPM which restricts the usage to few examples.

To evaluate the quality of a BPM simulation with respect to an FDTD simulation, a direct comparison of both methods is shown in fig. C.1. In this example, the hole geometry is derived from a real hole silhouette after approximately 1,700 pulses for drilling with a fluence of $10\,\mathrm{J/cm^2}$ respectively a pulse energy of $30\,\mu\mathrm{J}$. At this state, the hole already features several bulges and in the lower part also a bending. The focal spot diameter at the surface is ca. $25\,\mu\mathrm{m}$ for the wavelength of $1030\,\mathrm{nm}$. In case of the FDTD method, the electric field E is calculated for a polarization perpendicular to the image plane (TE-polarization) and shown at a specific time. Fig. C.1 shows $|E|^2$ which is directly proportional to the intensity. At the surface ($z = 0\,\mu\mathrm{m}$), the maximum of the Gaussian electric field distribution is normalized to 1.
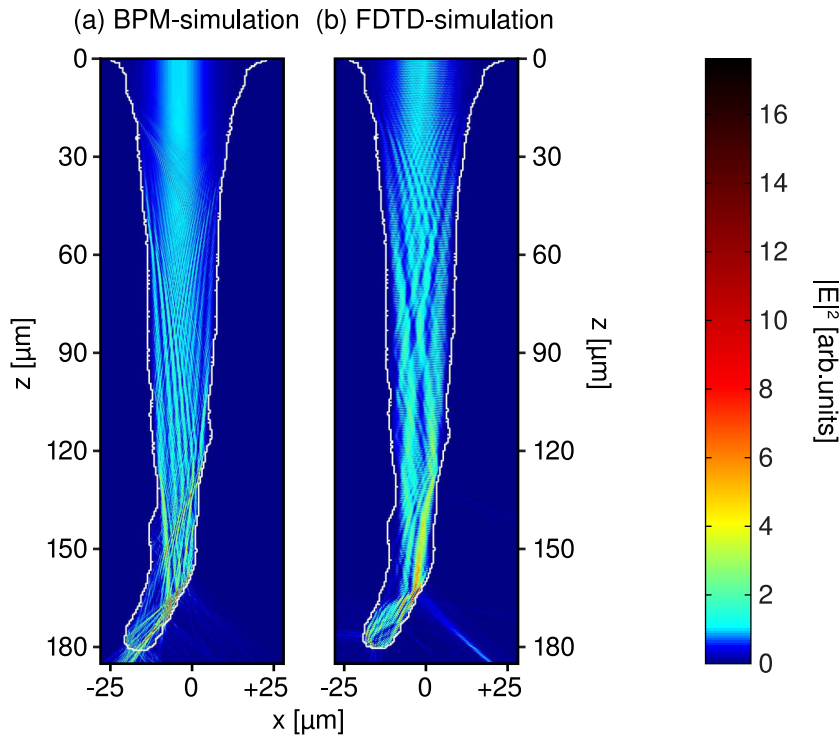
Fig. C.1: Comparison of the light propagation simulation inside a laser drilled hole by BPM (a) and FDTD method (b). The hole geometry is shown as a white outline. Both methods show a good qualitative agreement.

In general, both methods show a good qualitative agreement of the intensity distribution inside the hole. In both cases, there is the formation of an interference pattern due to diffraction on the sidewalls beginning at a depth of approximately 20 μm. The strongest interference can be observed in the lower part of the hole in the middle of the bending with a maximum value of ca. 17.6 for $|E|^2$ in case of the BPM simulation and ca. 16.5 in case of the FDTD simulation. This means there is also an acceptable quantitative agreement. A deflection of the beam can be observed in both simulations, especially in the bending of the hole. In both cases, there is a light guiding effect to the tip of the hole.

Nevertheless, there are also differences between both methods. Naturally, the FDTD simulation also shows the fast amplitude variation of the field which is not available from the BPM. There is also a difference in the actual interference pattern, but this does not affect the general features of the light propagation, especially the light guiding to the tip of the hole. Moreover, the FDTD also accounts for back reflections, especially at the hole bottom, which is not included in the BPM simulation.

In conclusion, this example illustrates that the BPM is capable of reproducing the fundamental features of the light propagation comparable to the more accurate but also more complex and extensive FDTD method. Anyway, the evaluation in a two-dimensional section does not account for the complete three-dimensional hole volume. In addition, the simulations here are based on the outline of the hole as observed by in-situ imaging. That means, the hole boundary does not represent the real inner surface of the hole and interaction with hole walls may not be treated correctly, which may lead to an underestimation of the beam deflection. The hole geometry is also smoothed for the simulation which neglects any small surface features. Due to these limitations, BPM simulations are an adequate method for a general, qualitative interpretation of the light propagation within the scope of this study.

References

[1] D. Bäuerle, *Laser Processing and Chemistry*, 4th edn., Springer-Verlag, Heidelberg, 2011.

[2] H. Hügel and T. Graf, *Laser in der Fertigung*, 2nd edn., Vieweg+Teubner, Wiesbaden, 2009.

[3] R. Poprawe, *Lasertechnik für die Fertigung*, Springer-Verlag, Berlin, 2005.

[4] B. N. Chichkov, C. Momma, S. Nolte, F. von Alvensleben and A. Tünnermann, "Femtosecond, picosecond and nanosecond laser ablation of solids," Applied Physics A 63, 109–115 (1996).

[5] C. Momma, B. N. Chichkov, S. Nolte, F. von Alvensleben, A. Tünnermann, H. Welling and B. Wellegehausen, "Short-pulse laser ablation of solid targets," Optics Communications 129, 134–142 (1996).

[6] S. Nolte, C. Momma, B. N. Chichkov and H. Welling, "Mikrostrukturierung mit ultrakurzen Laserpulsen," Physikalische Blätter 55, 1–5 (1999).

[7] M. D. Perry, B. C. Stuart, P. S. Banks, M. D. Feit, V. Yanovsky and A. M. Rubenchik, "Ultrashort-pulse laser machining of dielectric materials," Journal of Applied Physics 85, 6803–6810 (1999).

[8] S. Weiler, "High-power pico- and femtosecond lasers enable new applications," Laser Focus World 47, 55–61 (2011).

[9] J. König and T. Bauer, "Fundamentals and industrial applications of ultrashort pulsed lasers at Bosch," A. Heisterkamp, J. Neev and S. Nolte (Eds.), *Frontiers in Ultrafast Optics: Biomedical, Scientific, and Industrial Applications XI*, vol. 7925 of *Proc. of SPIE*, 792510, San Francisco, USA (2011).

[10] H. Booth, "Recent applications of pulsed lasers in advanced materials processing," Thin Solid Films 453-454, 450–457 (2004).

[11] H. Booth, "Laser Processing in Industrial Solar Module Manufacturing," Journal of Laser Micro/Nanoengineering 5, 183–191 (2010).

[12] B. C. Stuart, M. D. Feit, A. M. Rubenchik, B. W. Shore and M. D. Perry, "Laser-induced damage in dielectrics with nanosecond to subpicosecond pulses," Physical Review Letters 74, 2248–2251 (1995).

[13] I. V. Hertel, R. Stoian, D. Ashkenasi, A. Rosenfeld and E. E. B. Campbell, "On the physics of material processing with femtosecond lasers," RIKEN Review 32, 23–30 (2001).

[14] B. Rethfeld, K. Sokolowski-Tinten, D. von der Linde and S. I. Anisimov, "Timescales in the response of materials to femtosecond laser excitation," Applied Physics A 79, 767–769 (2004).

[15] F. Dausinger, F. Lichtner and H. Lubatschowski (Eds.), *Femtosecond Technology for Technical and Medical Applications*, Springer-Verlag, Berlin (2004).

[16] S. K. Sundaram and E. Mazur, "Inducing and probing non-thermal transitions in semiconductors using femtosecond laser pulses," nature materials 1, 217–224 (2002).

[17] L. Cerami, E. Mazur, S. Nolte and C. B. Schaffer, "Femtosecond Laser Micromachining," R. Thomson, C. Leburn and D. Reid (Eds.), *Ultrafast Nonlinear Optics*, 287–322, Springer-Verlag, Heidelberg, 2013.

[18] J. Cheng, C.-S. Liu, S. Shang, D. Liu, W. Perrie, G. Dearden and K. Watkins, "A review of ultrafast laser materials micromachining," Optics & Laser Technology 46, 88–102 (2013).

[19] T. Abeln, J. Radtke and F. Dausinger, "High Precision Drilling with Short-Pulsed Solid-State Lasers," *ICALEO*, San Diego, 1999.

[20] A. E. Wynne and B. C. Stuart, "Rate dependence of short-pulse laser ablation of metals in air and vacuum," Applied Physics A 76, 373–378 (2003).

[21] T. V. Kononenko, V. I. Konov, S. V. Garnov, S. M. Klimentov and F. Dausinger, "Dynamics of Deep Short Pulse Laser Drilling: Ablative Stages and Light Propagation," Laser Physics 11, 343–351 (2001).

[22] T. Matsumura, T. Nakatani and T. Yagi, "Deep drilling on a silicon plate with a femtosecond laser: experiment and model analysis," Applied Physics A 86, 107–114 (2007).

[23] S. Lazare, J. Lopez and F. Weisbuch, "High-aspect-ratio microdrilling in polymeric materials with intense KrF laser radiation," Applied Physics A 69 [Suppl.], S1–S6 (1999).

[24] J. Radtke, *Herstellung von Präzisionsdurchbrüchen in keramischen Werkstoffen mittels repetierender Laserbearbeitung*, Herbert Utz Verlag, München, 2003.

[25] S. Bruneau, J. Hermann, G. Dumitru, M. Sentis and E. Axente, "Ultra-fast laser ablation applied to deep-drilling of metals," Applied Surface Science 248, 299–303 (2005).

[26] M. Willert, *Strukturierung von metallischen Werkstoffen mit Laserstrahlung unter Vermeidung von Gefügeveränderungen*, Dissertation, Friedrich-Schiller-Universität Jena (2003).

[27] S. Nolte, C. Momma, G. Kamlage, A. Ostendorf, C. Fallnich, F. von Alvensleben and H. Welling, "Polarization effects in ultrashort-pulse laser drilling," Applied Physics A 68, 563–567 (1999).

[28] H. Varel, D. Ashkenasi, A. Rosenfeld, M. Wähmer and E. Campbell, "Micromachining of quartz with ultrashort laser pulses," Applied Physics A 373, 367–373 (1997).

[29] L. Shah, J. Tawney, M. Richardson and K. Richardson, "Femtosecond laser deep hole drilling of silicate glasses in air," Applied Surface Science 183, 151–164 (2001).

[30] A. Ruf, D. Breitling, C. Föhl, J. Radtke, F. Dausinger, H. Hügel, T. V. Kononenko, S. M. Klimentov, S. V. Garnov, V. I. Konov and J. Suzuki, "Modeling and experimental analysis of hole formation in laser deep drilling with short and ultra-short pulses," Wissenschaftliche Gesellschaft Lasertechnik (WLT) e.V. (Ed.), *Proc. First Intl. WLT-Conference on Lasers in Manufacturing*, 214–226, München (2001).

[31] T. V. Kononenko, S. M. Klimentov, S. V. Garnov, V. I. Konov, D. Breitling, C. Föhl, A. Ruf, J. Radtke and F. Dausinger, "Hole formation process in laser deep drilling with short and ultrashort pulses," I. Miyamoto, Y. F. Lu, S. Koji and J. Dubowski (Eds.), *Second International Symposium on Laser Precision Microfabrication*, vol. 4426 of *Proc. of SPIE*, 108–112 (2002).

[32] P. J. L. Webster, M. S. Muller and J. M. Fraser, "High speed in situ depth profiling of ultrafast micromachining," Optics Express 15, 14967–14972 (2007).

[33] F. P. Mezzapesa, A. Ancona, T. Sibillano, F. De Lucia, M. Dabbicco, P. M. Lugarà and G. Scamarcio, "High-resolution monitoring of the hole depth during ultrafast laser ablation drilling by diode laser self-mixing interferometry," Optics Letters 36, 822–824 (2011).

[34] S. M. Klimentov, T. V. Kononenko, P. A. Pivovarov, S. V. Garnov, V. I. Konov, A. M. Prokhorov, D. Breitling and F. Dausinger, "The role of plasma in ablation of materials by ultrashort laser pulses," Quantum Electronics 31, 378–382 (2001).

[35] D. Breitling, A. Ruf and F. Dausinger, "Fundamental aspects in machining of metals with short and ultrashort laser pulses," P. R. Herman, J. Fieret, A. Piqué, T. Okada, F. G. Bachmann, W. Hoving, K. Washio, X. Xu, J. J. Dubowski, D. B. Geohegan and F. Träger (Eds.), *Photon Processing in Microelectronics and Photonics III*, vol. 5339 of *Proc. of SPIE*, 49–63, Bellingham, WA (2004).

[36] S. M. Klimentov, S. V. Garnov, V. I. Konov, T. V. Kononenko, P. A. Pivovarov, O. G. Tsarkova, D. Breitling and F. Dausinger, "Effect of low-threshold air breakdown on material ablation by short laser pulses," Physics of Wave Phenomena 15, 1–11 (2007).

[37] L. Shah, J. Tawney, M. Richardson and K. Richardson, "Self-Focusing During Femtosecond Micromachining of Silicate Glasses," IEEE Journal of Quantum Electronics 40, 57–68 (2004).

[38] C. Föhl, D. Breitling and F. Dausinger, "Precise Drilling of Steel with Ultrashort Pulsed Solid-State Lasers," *LAT-Conference*, Moscow, 2002.

[39] A. Ruf, P. W. Berger, F. Dausinger and H. Hügel, "Analytical investigations on geometrical influences on laser drilling," Journal of Physics D: Applied Physics 34, 2918–2925 (2001).

[40] A. Michalowski, D. Walter, F. Dausinger and T. Graf, "Melt Dynamics and Hole Formation during Drilling with Ultrashort Pulses," Journal of Laser Micro/Nanoengineering 3, 211–215 (2008).

[41] C. Kittel, *Introduction to Solid State Physics*, 8th edn., John Wiley & Sons Inc., 2005.

[42] J. Bonse, S. Baudach, J. Krüger, W. Kautek and M. Lenzner, "Femtosecond laser ablation of silicon – modification thresholds and morphology," Applied Physics A 74, 19–25 (2002).

[43] E. Coyne, J. Magee, P. T. Mannion and G. M. O'Connor, "A Study of Femtosecond Laser Interaction with Wafer Grade Silicon," W. J. Blau, J. F. Donegan, A. F. Duke, B. D. MacCraith, J. A. McLaughlin, N. D. McMillan, G. M. O'Connar, E. O'Mongain and V. Toal (Eds.), *Opto-Ireland 2002: Optics and Photonics Technologies and Applications*, vol. 4876 of *Proc. of SPIE*, 487–499 (2003).

[44] F. Dausinger, "Präzisionsbohren mit kurzen und ultrakurzen Laserpulsen," Laser Technik Journal 1, 40–44 (2004).

[45] J. G. Fujimoto, J. M. Liu, E. P. Ippen and N. Bloembergen, "Femtosecond Laser Interaction with Metallic Tungsten and Nonequilibrium Electron and Lattice Temperatures," Physical Review Letters 53, 1837–1840 (1984).

[46] W. S. Fann, R. Storz, H. W. K. Tom and J. Bokor, "Electron thermalization in gold," Physical Review B 46, 13592–13595 (1992).

[47] S. I. Anisimov, B. L. Kapeliovich and T. L. Perel'man, "Electron emission from metal surfaces exposed to ultrashort laser pulses," Soviet Physics JETP 39, 375–377 (1974).

[48] M. I. Kaganov, I. M. Lifshitz and L. V. Tanatarov, "Relaxation between Electrons and Crystalline Lattice," Soviet Physics JETP 4, 173–178 (1957).

[49] H. E. Elsayed-Ali, T. B. Norris, M. A. Pessot and G. Mourou, "Time-Resolved Observation of Electron-Phonon Relaxation in Copper," Physical Review Letters 58, 1212–1215 (1987).

[50] S. I. Anisimov and B. Rethfeld, "On the Theory of Ultrashort Laser Pulse Interaction with a Metal," V. I. Konov and M. N. Libenson (Eds.), *Nonresonant Laser-Matter Interaction*, vol. 3093 of *Proc. of SPIE*, 192–203, Sankt Peterburg, Russia (1997).

[51] S. Preuss, A. Demchuk and M. Stuke, "Sub-picosecond UV laser ablation of metals," Applied Physics A 61, 33–37 (1995).

[52] H. M. van Driel, "Kinetics of high-density plasmas generated in Si by 1.06- and 0.53-µm picosecond laser pulses," Physical Review B 35, 8166–8176 (1987).

[53] N. M. Bulgakova, R. Stoian, A. Rosenfeld, I. Hertel, W. Marine and E. Campbell, "A general continuum approach to describe fast electronic transport in pulsed laser irradiated materials: The problem of Coulomb explosion," Applied Physics A 81, 345–356 (2005).

[54] R. Le Harzic, D. Breitling, M. Weikert, S. Sommer, C. Föhl, S. Valette, C. Donnet, E. Audouard and F. Dausinger, "Pulse width and energy influence on laser micromachining of metals in a range of 100fs to 5ps," Applied Surface Science 249, 322–331 (2005).

[55] S. Nolte, C. Momma, H. Jacobs, A. Tünnermann, B. N. Chichkov, B. Wellegehausen and H. Welling, "Ablation of metals by ultrashort laser pulses," Journal of the Optical Society of America B 14, 2716–2722 (1997).

[56] P. P. Pronko, S. K. Dutta, D. Du and R. K. Singh, "Thermophysical effects in laser processing of materials with picosecond and femtosecond pulses," Journal of Applied Physics 78, 6233–6240 (1995).

[57] B. Wu and Y. C. Shin, "A simple model for high fluence ultra-short pulsed laser metal ablation," Applied Surface Science 253, 4079–4084 (2007).

[58] R. Fang, D. Zhang, H. Wei, Z. Li, F. Yang and Y. Gao, "Improved two-temperature model and its application in femtosecond laser ablation of metal target," Laser and Particle Beams 28, 157–164 (2010).

[59] T. J. Derrien, T. Sarnet, M. Sentis and T. E. Itina, "Application of a two-temperature model for the investigation of the periodic structure formation on Si surface in femtosecond laser interactions," Journal of Optoelectronics and Advanced Materials 12, 610–615 (2010).

[60] J. Byskov-Nielsen, J.-M. Savolainen, M. S. Christensen and P. Balling, "Ultra-short pulse laser ablation of copper, silver and tungsten: experimental data and two-temperature model simulations," Applied Physics A 103, 447–453 (2011).

[61] K. Wædegaard, M. Frislev and P. Balling, "Femtosecond laser excitation of dielectric materials: experiments and modeling of optical properties and ablation depths," Applied Physics A 110, 601–605 (2012).

[62] J. Sotrop, M. Domke, A. Kersch and H. Huber, "Simulation of the melting volume in thin molybdenum films as a function of the laser pulse duration," Physics Procedia 41, 520–523 (2013).

[63] R. E. Russo, X. Mao, H. Liu, J. Yoo and S. S. Mao, "Time-resolved plasma diagnostics and mass removal during single-pulse laser ablation," Applied Physics A 69 [Suppl.], S887–S894 (1999).

[64] T. Y. Choi and C. P. Grigoropoulos, "Plasma and ablation dynamics in ultrafast laser processing of crystalline silicon," Journal of Applied Physics 92, 4918–4925 (2002).

[65] J. König, S. Nolte and A. Tünnermann, "Plasma evolution during metal ablation with ultrashort laser pulses," Optics Express 13, 10597–10607 (2005).

[66] S. S. Mao, X. Mao, R. Greif and R. E. Russo, "Initiation of an early-stage plasma during picosecond laser ablation of solids," Applied Physics Letters 77, 2464 (2000).

[67] L. V. Zhigilei and B. J. Garrison, "Mechanisms of laser ablation from molecular dynamics simulations: dependence on the initial temperature and pulse duration," Applied Physics A 69 [Suppl.], S75–S80 (1999).

[68] C. Schäfer, H. M. Urbassek and L. V. Zhigilei, "Metal ablation by picosecond laser pulses: A hybrid simulation," Physical Review B 66, 115404 (2002).

[69] K. Sokolowski-Tinten, J. Bialkowski, A. Cavalleri, M. Boing, H. Schüler and D. von der Linde, "Dynamics of femtosecond laser induced ablation from solid surfaces," *SPIE Conference on High-Power Laser Ablation*, vol. 3343 of *Proc. of SPIE*, 46–57, Santa Fe, NM (1998).

[70] P. Lorazo, L. Lewis and M. Meunier, "Thermodynamic pathways to melting, ablation, and solidification in absorbing solids under pulsed laser irradiation," Physical Review B 73, 134108 (2006).

[71] A. Upadhyay, N. Inogamov, B. Rethfeld and H. Urbassek, "Ablation by ultrashort laser pulses: Atomistic and thermodynamic analysis of the processes at the ablation threshold," Physical Review B 78, 045437 (2008).

[72] C. Wu and L. V. Zhigilei, "Microscopic mechanisms of laser spallation and ablation of metal targets from large-scale molecular dynamics simulations," Applied Physics A 114, 11–32 (2014).

[73] S. Amoruso, C. Altucci, R. Bruzzese, C. de Lisio, N. Spinelli, R. Velotta, M. Vitiello and X. Wang, "Study of the plasma plume generated during near IR femtosecond laser irradiation of silicon targets," Applied Physics A 79, 1377–1380 (2004).

[74] A. V. Bulgakov, I. Ozerov and W. Marine, "Cluster emission under femtosecond laser ablation of silicon," Thin Solid Films 453-454, 557–561 (2004).

[75] S. Amoruso, G. Ausanio, A. C. Barone, R. Bruzzese, L. Gragnaniello, M. Vitiello and X. Wang, "Ultrashort laser ablation of solid matter in vacuum: a comparison between the picosecond and femtosecond regimes," Journal of Physics B: Atomic, Molecular and Optical Physics 38, L329–L338 (2005).

[76] S. Amoruso, R. Bruzzese, N. Spinelli, R. Velotta, M. Vitiello, X. Wang, G. Ausanio, V. Iannotti and L. Lanotte, "Generation of silicon nanoparticles via femtosecond laser ablation in vacuum," Applied Physics Letters 84, 4502–4504 (2004).

[77] S. Amoruso, G. Ausanio, R. Bruzzese, L. Gragnaniello, L. Lanotte, M. Vitiello and X. Wang, "Characterization of laser ablation of solid targets with near-infrared laser pulses of 100fs and 1ps duration," Applied Surface Science 252, 4863–4870 (2006).

[78] N. N. Nedialkov, S. E. Imamova and P. A. Atanasov, "Ablation of metals by ultrashort laser pulses," Journal of Physics D: Applied Physics 37, 638–643 (2004).

[79] M. Agranat, S. I. Anisimov, S. I. Ashitkov, V. Zhakhovskii, N. A. Inogamov, K. Nishihara, Y. V. Petrov, V. E. Fortov and V. A. Khokhlov, "Dynamics of plume and crater formation after action of femtosecond laser pulse," Applied Surface Science 253, 6276–6282 (2007).

[80] M. Prasad, P. F. Conforti and B. J. Garrison, "Influence of photoexcitation pathways on the initiation of ablation in poly (methyl methacrylate)," Applied Physics A 92, 877–881 (2008).

[81] V. V. Zhakhovskii, N. A. Inogamov, Y. V. Petrov, S. I. Ashitkov and K. Nishihara, "Molecular dynamics simulation of femtosecond ablation and spallation with different interatomic potentials," Applied Surface Science 255, 9592–9596 (2009).

[82] N. M. Bulgakova and A. V. Bulgakov, "Pulsed laser ablation of solids: transition from normal vaporization to phase explosion," Applied Physics A 73, 199–208 (2001).

[83] V. Craciun, N. Bassim, R. Singh, D. Craciun, J. Hermann and C. Boulmer-Leborgne, "Laser-induced explosive boiling during nanosecond laser ablation of silicon," Applied Surface Science 186, 288–292 (2002).

[84] D. Breitling, K.-P. Muller, A. Ruf, P. Berger and F. Dausinger, "Material-vapor dynamics during ablation with ultrashort pulses," *Fourth International Symposium on Laser Precision Microfabrication*, vol. 5063 of *Proc. of SPIE*, 81–86, Bellingham, WA (2003).

[85] N. M. Bulgakova, A. B. Evtushenko, Y. G. Shukhov, S. I. Kudryashov and A. V. Bulgakov, "Role of laser-induced plasma in ultradeep drilling of materials by nanosecond laser pulses," Applied Surface Science 257, 10876–10882 (2011).

[86] P. S. Banks, M. D. Feit, A. M. Rubenchik, B. C. Stuart and M. D. Perry, "Material effects in ultra-short pulse laser drilling of metals," Applied Physics A 69 [Suppl.], S377–S380 (1999).

[87] G. Dumitru, V. Romano, H. Weber, M. Sentis, J. Hermann, S. Bruneau, W. Marine, H. Haefke and Y. Gerbig, "Metallographical analysis of steel and hard metal substrates after deep-drilling with femtosecond laser pulses," Applied Surface Science 208-209, 181–188 (2003).

[88] A. Ancona, F. Röser, K. Rademaker, J. Limpert, S. Nolte and A. Tünnermann, "High speed laser drilling of metals using a high repetition rate, high average power ultrafast fiber CPA system," Optics Express 16, 8958–8968 (2008).

[89] A. Weck, T. Crawford, D. S. Wilkinson, H. K. Haugen and J. S. Preston, "Laser drilling of high aspect ratio holes in copper with femtosecond, picosecond and nanosecond pulses," Applied Physics A 90, 537–543 (2008).

[90] A. Luft, U. Franz, A. Emsermann and J. Kaspar, "A study of thermal and mechanical effects on materials induced by pulsed laser drilling," Applied Physics A 63, 93–101 (1996).

[91] T. V. Kononenko, S. M. Klimentov, V. I. Konov, P. A. Pivovarov, S. V. Garnov, F. Dausinger and D. Breitling, "Propagation of short-pulsed laser radiation and stages of ablative deep channel formation," Malcolm C. Gower, H. Helvajian, K. Sugioka and J. J. Dubowski (Eds.), *Laser Applications in Microelectronic and Optoelectronic Manufacturing VI*, vol. 4274 of *Proc. of SPIE*, 248–257 (2001).

[92] F. Dausinger, "Femtosecond technology for precision manufacturing: Fundamental and technical aspects," RIKEN Review 50, 77–82 (2003).

[93] A. Weck, T. Crawford, D. S. Wilkinson, H. K. Haugen and J. S. Preston, "Ripple formation during deep hole drilling in copper with ultrashort laser pulses," Applied Physics A 89, 1001–1003 (2007).

[94] F. Siegel, U. Klug and R. Kling, "Extensive Micro-Structuring of Metals using Picosecond Pulses – Ablation Behavior and Industrial Relevance," Journal of Laser Micro/Nanoengineering 4, 2–8 (2009).

[95] B. Neuenschwander, B. Jaeggi, M. Schmid, A. Dommann, A. Neels, T. Bandi and G. Hennig, "Factors controlling the incubation in the application of ps laser pulses on copper and iron surfaces," X. Xu, G. Hennig, Y. Nakata and S. W. Roth (Eds.), *Laser Applications in Microelectronic and Optoelectronic Manufacturing (LAMOM) XVIII*, vol. 8607 of *Proc. of SPIE*, 86070D, San Francisco, USA (2013).

[96] R. Torres, T. Kämpfe, M. Delaigue, O. Parriaux, C. Hönninger, J. Lopez, R. Kling and E. Mottay, "Influence of Laser Beam Polarization on Laser Micro-Machining of Molybdenum," Journal of Laser Micro/Nanoengineering 8, 188–191 (2013).

[97] C.-H. Lin, R. A. Powell, L. Jiang, H. Xiao, S.-J. Chen and H.-L. Tsai, "Real-time depth measurement for micro-holes drilled by lasers," Measurement Science and Technology 21, 025307 (2010).

[98] R. Lausten and P. Balling, "On-the-fly depth profiling during ablation with ultrashort laser pulses: A tool for accurate micromachining and laser surgery," Applied Physics Letters 79, 884–886 (2001).

[99]   C. Stauter, J. Fontaine and T. Engel, "Real-time determination of the amount of removed material during short pulse laser micromachining," Applied Surface Science 96-98, 522–527 (1996).

[100] S. Strgar and J. Mozina, "An optodynamic determination of the depth of laser-drilled holes by the simultaneous detection of ultrasonic waves in the air and in the workpiece," Ultrasonics 40, 791–795 (2002).

[101] D. Walter, A. Michalowski, R. Gauch and F. Dausinger, "Monitoring of the micro-drilling process by means of laser-induced shock waves," *Proc. Fourth Intl. WLT-Conference on Lasers in Manufacturing*, Munich, Germany, 2007.

[102] D. Walter, *Online-Qualitätssicherung beim Bohren mittels ultrakurz gepulster Laserstrahlung*, Herbert Utz Verlag, München, 2010.

[103] C.-C. Ho, J.-J. He and T.-Y. Liao, "On-line estimation of laser-drilled hole depth using a machine vision method," Sensors 12, 10148–10162 (2012).

[104] P. J. L. Webster, J. X. Z. Yu, B. Y. C. Leung, M. D. Anderson, V. X. D. Yang and J. M. Fraser, "In situ 24 kHz coherent imaging of morphology change in laser percussion drilling," Optics Letters 35, 646–648 (2010).

[105] F. P. Mezzapesa, V. Spagnolo, A. Ancona and G. Scamarcio, "Detection of ultrafast laser ablation using quantum cascade laser-based sensing," Applied Physics Letters 101, 171107 (2012).

[106] D. Meschede, *Gerthsen Physik*, 21st edn., Springer-Verlag, Berlin, 2002.

[107] M. Schneider, L. Berthe, M. Muller and R. Fabbro, "A fast method for morphological analysis of laser drilling holes," Journal of Laser Applications 22, 127–131 (2010).

[108] A. Heider, J. Sollinger, F. Abt, M. Boley, R. Weber and T. Graf, "High-Speed X-Ray Analysis of Spatter Formation in Laser Welding of Copper," Physics Procedia 41, 112–118 (2013).

[109] S. Preuss, E. Matthias and M. Stuke, "Sub-picosecond UV-laser ablation of Ni-films," Applied Physics A 59, 79–82 (1994).

[110] P. T. Mannion, J. Magee, E. Coyne, G. M. O'Connor and T. J. Glynn, "The effect of damage accumulation behaviour on ablation thresholds and damage morphology in ultrafast laser micro-machining of common metals in air," Applied Surface Science 233, 275–287 (2004).

[111] E. G. Gamaly, A. V. Rode, B. Luther-Davies and V. T. Tikhonchuk, "Ablation of solids by femtosecond lasers: ablation mechanism and ablation thresholds for metals and dielectrics," Physics of Plasmas 9, 949–957 (2002).

[112] M. Brajdic, M. Hermans, A. Horn and I. Kelbassa, "In situ measurement of plasma and shock wave properties inside laser-drilled metal holes," Measurement Science and Technology 19, 105703 (2008).

[113] M. Honer, *Prozesssicherungsmaßnahmen beim Bohren metallischer Werkstoffe mittels Laserstrahlung*, Herbert Utz Verlag, München, 2004.

[114] A. Ruf, *Modellierung des Perkussionsbohrens von Metallen mit kurz- und ultrakurzgepulsten Lasern*, Herbert Utz Verlag, München, 2004.

[115] D. Breitling, *Gasphaseneinflüsse beim Abtragen und Bohren mit ultrakurz gepulster Laserstrahlung*, Herbert Utz Verlag, München (2009).

[116] C. S. Nielsen and P. Balling, "Deep drilling of metals with ultrashort laser pulses: A two-stage process," Journal of Applied Physics 99, 093101 (2006).

[117] C. Föhl and F. Dausinger, "High precision laser drilling with ultra short pulses - fundamental aspects and technical applications," *2nd Pacific International Conference on Application of Lasers and Optics (PICALO)*, 2006.

[118] C. Föhl, D. Breitling and F. Dausinger, "Precise Drilling of Steel with Ultrashort Pulsed Solid-State Lasers," F. Dausinger, V. I. Konov, V. Y. Baranov and V. Y. Panchenko (Eds.), *Laser Processing of Advanced Materials and Laser Microtechnologies*, vol. 5121 of *Proc. of SPIE*, 271–279 (2003).

[119] K. Tönshoff, C. Momma, A. Ostendorf, S. Nolte and G. Kamlage, "Microdrilling of metals with ultrashort laser pulses," Journal of Laser Applications 12, 23–27 (2000).

[120] S. Tao, B. Wu and S. Lei, "Study of laser beam propagation in microholes and the effect on femtosecond laser micromachining," Journal of Applied Physics 109, 123506 (2011).

[121] D. Breitling, A. Ruf, P. W. Berger, F. Dausinger, S. M. Klimentov, P. A. Pivovarov, T. V. Kononenko and V. I. Konov, "Plasma effects during ablation and drilling using pulsed solid-state lasers," F. H. Dausinger, V. I. Konov, V. Y. Baranov and V. Y. Panchenko (Eds.), *Laser Processing of Advanced Materials and Laser Microtechnologies*, vol. 5121 of *Proc. of SPIE*, 24–33 (2003).

[122] P. Bourgeois, *Laserinduzierte Durchbrüche in aerosolbehafteter Luft*, Dissertation, Universität Fridericiana Karlsruhe (1997).

[123] W. Schulz, U. Eppelt and R. Poprawe, "Review on laser drilling I. Fundamentals, modeling, and simulation," Journal of Laser Applications 25, 012006 (2013).

[124] C. Föhl and F. Dausinger, "High precision deep drilling with ultrashort pulses," I. Miyamoto, A. Ostendorf, K. Sugioka and H. Helvajian (Eds.), *Fourth International Symposium on Laser Precision Microfabrication*, vol. 5063 of *Proc. of SPIE*, 346–351, Bellingham, WA (2003).

[125] F. P. Mezzapesa, L. Columbo, M. Brambilla, M. Dabbicco, A. Ancona, T. Sibillano and G. Scamarcio, "Laser ablation dynamics in metals : The thermal regime," Applied Physics Letters 101, 011103 (2012).

[126] S. M. Klimentov, P. A. Pivovarov, V. I. Konov, D. Breitling and F. Dausinger, "Laser microprocessing in a gas environment at a high repetition rate of ablative pulses," Quantum Electronics 34, 537–540 (2004).

[127] A. Ancona, S. Döring, C. Jauregui, F. Röser, J. Limpert, S. Nolte and A. Tünnermann, "Femtosecond and picosecond laser drilling of metals at high repetition rates and average powers," Optics Letters 34, 3304–3306 (2009).

[128] S. Döring, A. Ancona, S. Hädrich, J. Limpert, S. Nolte and A. Tünnermann, "Microdrilling of metals using femtosecond laser pulses and high average powers at 515 nm and 1030 nm," Applied Physics A 100, 53–56 (2010).

[129] E. D. Palik (Ed.), *Handbook of Optical Constants of Solids*, Academic Press, Boston, 1985.

[130] K. Sokolowski-Tinten and D. von der Linde, "Generation of dense electron-hole plasmas in silicon," Physical Review B 61, 2643–2650 (2000).

[131] T. Wagner, *Abtragen von Silizium mit ultrakurzen Laserpulsen*, Dissertation, Universität Hannover (2001).

[132] B. C. Stuart, M. D. Feit, S. Herman, A. M. Rubenchik, B. W. Shore and M. D. Perry, "Nanosecond-to-femtosecond laser-induced breakdown in dielectrics," Physical Review B 53, 1749–1761 (1996).

[133] J. M. Liu, "Simple technique for measurements of pulsed Gaussian-beam spot sizes." Optics Letters 7, 196–198 (1982).

[134] R. Hull (Ed.), *Properties of Crystalline Silicon*, The Institution of Electrical Engineers (INSPEC), London, 1999.

[135] P. A. Tipler, *Physik*, 1st edn., Spektrum Akademischer Verlag, Heidelberg, 1994.

[136] T. Matsumura, A. Kazama and T. Yagi, "Generation of debris in the femtosecond laser machining of a silicon substrate," Applied Physics A 81, 1393–1398 (2005).

[137] D. E. Aspnes and A. A. Studna, "Dielectric functions and optical parameters of Si, Ge, GaP, GaAs, GaSb, InP, InAs, and InSb from 1.5 to 6.0 eV," Physical Review B 27, 985–1009 (1983).

[138] "Standard Practice for Conversion Between Resistivity and Dopant Density for Boron-Doped, Phosphorus-Doped, and Arsenic-Doped Silicon," *Annual Book of ASTM Standards, ASTM Designation: F 723-99*, American Society for Testing and Materials, West Conshohocken, PA (2000).

[139] F. P. Mezzapesa, T. Sibillano, F. Di Niso, A. Ancona, P. M. Lugarà, M. Dabbicco and G. Scamarcio, "Real time ablation rate measurement during high aspect-ratio hole drilling with a 120-ps fiber laser," Optics Express 20, 663–671 (2012).

[140] J. Byskov-Nielsen, J.-M. Savolainen, M. S. Christensen and P. Balling, "Ultra-short pulse laser ablation of metals: threshold fluence, incubation coefficient and ablation rates," Applied Physics A 101, 97–101 (2010).

[141] G. Chang and Y. Tu, "An effective focusing setting in femtosecond laser multiple pulse ablation," Optics & Laser Technology 54, 30–34 (2013).

[142] D. Strickland and G. Mourou, "Compression of amplified chirped optical pulses," Optics Communications 55, 447–449 (1985).

[143] C. Rullière (Ed.), *Femtosecond Laser Pulses*, 2nd edn., Springer-Verlag, New York, 2005.

[144] F. Hansen and W. W. Duley, "Attenuation of laser radiation by particles during laser materials processing," Journal of Laser Applications 6, 137–143 (1994).

[145] S. Amoruso, B. Toftmann, J. Schou, R. Velotta and X. Wang, "Diagnostics of laser ablated plasma plumes," Thin Solid Films 453-454, 562–572 (2004).

[146] S. Besner, J.-Y. Degorce, A. Kabashin and M. Meunier, "Influence of ambient medium on femtosecond laser processing of silicon," Applied Surface Science 247, 163–168 (2005).

[147] S. Amoruso, R. Bruzzese, X. Wang and J. Xia, "Propagation of a femtosecond pulsed laser ablation plume into a background atmosphere," Applied Physics Letters 92, 041503 (2008).

[148] A. Di Bernardo, C. Courtois, B. Cros, G. Matthieussent, D. Batani, T. Desai, F. Strati and G. Lucchini, "High-intensity ultrashort laser-induced ablation of stainless steel foil targets in the presence of ambient gas," Laser and Particle Beams 21, 59–64 (2003).

[149] Z. Wu, X. Zhu and N. Zhang, "Time-resolved shadowgraphic study of femtosecond laser ablation of aluminum under different ambient air pressures," Journal of Applied Physics 109, 053113 (2011).

[150] J. Thorstensen and S. E. Foss, "Temperature dependent ablation threshold in silicon using ultrashort laser pulses," Journal of Applied Physics 112, 103514 (2012).

[151] B. Sallé, O. Gobert, P. Meynadier, M. Perdrix, G. Petite and A. Semerok, "Femtosecond and picosecond laser microablation: ablation efficiency and laser microplasma expansion," Applied Physics A 69 [Suppl.], S381–S383 (1999).

[152] M. J. Kidger, *Fundamental Optical Design*, SPIE Press, Bellingham, 2002.

[153] H. Gross, *Handbook of Optical Systems*, Wiley-VCH, Weinheim, 2005.

[154] M. Brajdic, K. Walther and U. Eppelt, "Analysis of laser drilled deep holes in stainless steel by superposed pulsed Nd:YAG laser radiation," Optics and Lasers in Engineering 46, 648–655 (2008).

[155] A. Taflove and S. C. Hagness, *Computational Electrodynamics: The Finite-Difference Time-Domain Method*, 2nd edn., Artech House, Boston, 2000.

[156] T.-C. Poon and T. Kim, *Engineering Optics with MATLAB*, World Scientific Publishing, Singapore, 2006.

[157] B. E. A. Saleh and M. C. Teich, *Fundamentals of Photonics*, 2nd edn., John Wiley & Sons Inc., Hoboken, 2007.

[158] D. S. Ivanov, A. I. Kuznetsov, V. P. Lipp, B. Rethfeld, B. N. Chichkov, M. E. Garcia and W. Schulz, "Short laser pulse nanostructuring of metals: direct comparison of molecular dynamics modeling and experiment," Applied Physics A 111, 675–687 (2013).

[159] E. N. Landis and D. T. Keane, "X-ray microtomography," Materials Characterization 61, 1305–1316 (2010).

[160] E. Jung, A. Ostmann, P. Ramm, J. Wolf, M. Toepper and M. Wiemer, "Through Silicon Vias as Enablers for 3D Systems," *Symposium on Design, Test, Integration and Packaging of MEMS/MOEMS*, 119–122, Nice, France, 2008.

[161] S. Hädrich, M. Krebs, J. Rothhardt, H. Carstens, S. Demmler and A. Tünnermann, "Generation of µW level plateau harmonics at high repetition rate," Optics Express 19, 19374–19383 (2011).

[162] K. Eimann and M. Drach, "Entlüftungshilfe für ein Spritzgusswerkzeug und Verfahren zu deren Herstellung,", European Patent EP1590156, Braun GmbH, Kronberg, Germany, 2005.

[163] Verein Deutscher Ingenieure VDI-Gesellschaft Verfahrenstechnik und Chemieingenieurwesen (GVC), *VDI-Wärmeatlas*, 10th edn., Springer-Verlag, Berlin, 2006.

[164] N. W. Ashcroft and D. N. Mermin, *Solid State Physics*, international edn., Saunders College, Philadelphia, 1976.

[165] G. L. Eesley, "Generation of nonequilibrium electron and lattice temperatures in copper by picosecond laser pulses," Physical Review B 33, 2144–2151 (1986).

[166] X. Y. Wang, D. M. Riffe, Y.-S. Lee and M. C. Downer, "Time-resolved electron-temperature measurement in a highly excited gold target using femtosecond thermionic emission," Physical Review B 50, 8016–8019 (1994).

[167] Z. Lin, L. Zhigilei and V. Celli, "Electron-phonon coupling and electron heat capacity of metals under conditions of strong electron-phonon nonequilibrium," Physical Review B 77, 075133 (2008).

[168] P. B. Johnson and R. W. Christy, "Optical Constants of the Noble Metals," Physical Review B 6, 4370–4379 (1972).

[169] R. Biswas and V. Ambegaokar, "Phonon spectrum of a model of electronically excited silicon," Physical Review B 26, 1980–1988 (1982).

[170] R. F. Wood and G. E. Giles, "Macroscopic theory of pulsed-laser annealing. I. Thermal transport and melting," Physical Review B 23, 2923–2942 (1981).

[171] C. J. Glassbrenner and G. A. Slack, "Thermal Conductivity of Silicon and Germanium from 3°K to the Melting Point," Physical Review 134, A1058–A1069 (1964).

[172] E. J. Yoffa, "Screening of hot-carrier relaxation in highly photoexcited semiconductors," Physical Review B 23, 1909–1919 (1981).

[173] T. Sjodin, H. Petek and H.-L. Dai, "Ultrafast Carrier Dynamics in Silicon: A Two-Color Transient Reflection Grating Study on a (111) Surface," Physical Review Letters 81, 5664–5667 (1998).

[174] K. G. Svantesson, "Determination of the interband and the free carrier absorption constants in silicon at high-level photoinjection," Journal of Physics D: Applied Physics 12, 425–436 (1979).

[175] J. Dziewior and W. Schmid, "Auger coefficients for highly doped and highly excited silicon," Applied Physics Letters 31, 346–348 (1977).

[176] D. H. Reitze, T. R. Zhang, W. M. Wood and M. C. Downer, "Two-photon spectroscopy of silicon using femtosecond pulses at above-gap frequencies," Journal of the Optical Society of America B 7, 84–89 (1990).

Publications in Peer-reviewed Journals

[P1] A. Ancona, S. Döring, C. Jauregui, F. Röser, J. Limpert, S. Nolte and A. Tünnermann, "Femtosecond and picosecond laser drilling of metals at high repetition rates and average powers," Optics Letters 34, 3304–3306 (2009).

[P2] S. Döring, A. Ancona, S. Hädrich, J. Limpert, S. Nolte and A. Tünnermann, "Microdrilling of metals using femtosecond laser pulses and high average powers at 515 nm and 1030 nm," Applied Physics A 100, 53–56 (2010).

[P3] S. Döring, S. Richter, S. Nolte and A. Tünnermann, "In situ imaging of hole shape evolution in ultrashort pulse laser drilling," Optics Express 18, 20395–20400 (2010).

[P4] S. Döring, S. Richter, A. Tünnermann and S. Nolte, "Evolution of hole depth and shape in ultrashort pulse deep drilling in silicon," Applied Physics A 105, 69–74 (2011).

[P5] S. Richter, S. Döring, A. Tünnermann and S. Nolte, "Bonding of glass with femtosecond laser pulses at high repetition rates," Applied Physics A 103, 257–261 (2011).

[P6] S. Richter, M. Heinrich, S. Döring, A. Tünnermann and S. Nolte, "Formation of femtosecond laser-induced nanogratings at high repetition rates," Applied Physics A 104, 503–507 (2011).

[P7] S. Döring, J. Szilagyi, S. Richter, F. Zimmermann, M. Richardson, A. Tünnermann and S. Nolte, "Evolution of hole shape and size during short and ultrashort pulse laser deep drilling," Optics Express 20, 27147–27154 (2012).

[P8] S. Richter, M. Heinrich, S. Döring, A. Tünnermann and S. Nolte, "Nanogratings in fused silica: Formation, control, and applications," Journal of Laser Applications 24, 042008 (2012).

[P9] S. Richter, F. Jia, M. Heinrich, S. Döring, U. Peschel, A. Tünnermann and S. Nolte, "The role of self-trapped excitons and defects in the formation of nanogratings in fused silica." Optics Letters 37, 482–484 (2012).

[P10] S. Richter, A. Plech, M. Steinert, M. Heinrich, S. Döring, F. Zimmermann, U. Peschel, E. B. Kley, A. Tünnermann and S. Nolte, "On the fundamental structure of femtosecond laser-induced nanogratings," Laser & Photonics Reviews 1-6, 787–792 (2012).

[P11] S. Döring, S. Richter, F. Heisler, T. Ullsperger, A. Tünnermann and S. Nolte, "Influence of ambient pressure on the hole formation in laser deep drilling," Applied Physics A 112, 623–629 (2013).

[P12] S. Richter, S. Döring, F. Burmeister, F. Zimmermann, A. Tünnermann and S. Nolte, "Formation of periodic disruptions induced by heat accumulation of femtosecond laser pulses," Optics Express 21, 15452–15463 (2013).

[P13] S. Richter, F. Zimmermann, S. Döring, A. Tünnermann and S. Nolte, "Ultrashort high repetition rate exposure of dielectric materials: laser bonding of glasses analyzed by micro-Raman spectroscopy," Applied Physics A 110, 9–15 (2013).

[P14] F. Zimmermann, S. Richter, S. Döring, A. Tünnermann and S. Nolte, "Ultrastable bonding of glass with femtosecond laser bursts," Applied Optics 52, 1149–1154 (2013).

[P15] F. Zimmermann, A. Plech, S. Richter, S. Döring, A. Tünnermann and S. Nolte, "Structural evolution of nanopores and cracks as fundamental constituents of ultrashort pulse-induced nanogratings," Applied Physics A 114, 75–79 (2014).

[P16] A. Brahm, S. Döring, A. Wilms, G. Notni, S. Nolte and A. Tünnermann, "Laser-generated broadband antireflection structures for freeform silicon lenses at terahertz frequencies," Applied Optics 53, 2886–2891 (2014).

[P17] J. Gonzalez–Julian, O. Cedillos–Barraza, S. Döring, S. Nolte, O. Guillon and W. E. Lee. "Enhanced oxidation resistance of ZrB_2/SiC composite through in situ reaction of gadolinium oxide in patterned surface cavities," Journal of the European Ceramic Society 34, 4157–4166 (2014).

Conference Contributions

[C1] A. Ancona, C. Jauregui, S. Döring, F. Röser, J. Limpert, S. Nolte and A. Tünnermann, "Ultrashort pulse laser drilling of metals using a high repetition rate, high average power fiber CPA system," J. Neev, S. Nolte, A. Heisterkamp and R. P. Trebino (Eds.), *Commercial and Biomedical Applications of Ultrafast Lasers IX*, vol. 7203 of *Proc. of SPIE*, 720311, San Jose, CA, USA (2009).

[C2] S. Döring, A. Ancona, S. Hädrich, J. Limpert, S. Nolte and A. Tünnermann, "Microdrilling of metals using high repetition rate ultrashort laser pulses at 1030 nm and 515 nm," *Fifth Intl. WLT-Conference on Lasers in Manufacturing*, Munich, Germany (2009).

[C3] A. Ancona, S. Döring, S. Hädrich, J. Limpert, S. Nolte and A. Tünnermann, "Critical Performance Aspects of Ultrashort Pulse Laser Materials Processing at High Repetition Rates and Average Powers," *29th International Congress on Applications of Lasers & Electro-Optics (ICALEO)*, Anaheim, CA, USA (2010).

[C4] S. Döring, S. Richter, S. Nolte and A. Tünnermann, "In-situ imaging of the deep drilling of silicon with ultrashort laser pulses," *SUSSP66 International Summer School in Ultrafast Nonlinear Optics*, Edinburgh, Great Britain (2010).

[C5] S. Richter, S. Döring, G. Kalkowski, R. Eberhardt, S. Nolte and A. Tünnermann, "Bonding of glass with femtosecond laser pulses at high repetition rates," *Frontiers in Ultrafast Optics: Biomedical, Scientific, and Industrial Applications X*, San Francisco, CA, USA (2010).

[C6] S. Richter, S. Döring, S. Nolte and A. Tünnermann, "Bonding of glass with femtosecond laser pulses at high repetition rates," *SUSSP66 International Summer School in Ultrafast Nonlinear Optics*, Edinburgh, Great Britain (2010).

[C7] S. Richter, S. Döring, S. Nolte and A. Tünnermann, "Lokales Schweißen transparenter Werkstoffe mit ultrakurzen Pulsen," *7. Jenaer Lasertagung*, Jena, Germany (2010).

[C8] S. Döring, S. Richter, S. Nolte and A. Tünnermann, "In-situ observation of the hole formation during deep drilling with ultrashort laser pulses," A. Heisterkamp, J. Neev and S. Nolte (Eds.), *Frontiers in Ultrafast Optics: Biomedical, Scientific, and Industrial Applications XI*, vol. 7925 of *Proc. of SPIE*, 792517, San Francisco, CA, USA (2011).

[C9] S. Döring, S. Richter, A. Tünnermann and S. Nolte, "In-situ observation of ultrashort pulse deep drilling in silicon at 1030 nm and 515 nm," *Conference on Lasers and Electro-Optics Europe and 12th European Quantum Electronics Conference 2011 (CLEO EUROPE/EQEC)*, Munich, Germany (2011).

[C10] S. Nolte, S. Döring, A. Ancona and A. Tünnermann, "High Repetition Rate Ultrashort Pulse Micromachining with Fiber Lasers," *Fiber Lasers and Applications (FILAS)*, Istanbul, Turkey (2011).

[C11] S. Richter, S. Döring, T. Peschel, R. Eberhardt, S. Nolte and A. Tünnermann, "Breaking stress of glass welded with femtosecond laser pulses at high repetition rates," A. Heisterkamp, J. Neev and S. Nolte (Eds.), *Frontiers in Ultrafast Optics: Biomedical, Scientific, and Industrial Applications XI*, vol. 7925 of *Proc. of SPIE*, 79250P, San Francisco, CA, USA (2011).

[C12] S. Richter, S. Döring, A. Tünnermann and S. Nolte, "Formation Process of Femtosecond Laser-induced Nanogratings in Fused Silica at High Repetition Rates," *2nd International Workshop on Nonlinear Nanostructures for Ultrashort Laser Applications*, Berlin, Germany (2011).

[C13] S. Richter, S. Döring, F. Zimmermann, S. Nolte and A. Tünnermann, "Welding of glass with femtosecond laser pulses at high repetition rates," *DokDok*, Naumburg, Germany (2011).

[C14] S. Richter, M. Heinrich, S. Döring, A. Tünnermann and S. Nolte, "Formation process of Femtosecond Laser-induced Nanogratings at High Repetition Rates," *Conference on Lasers and Electro-Optics Europe and 12th European Quantum Electronics Conference 2011 (CLEO EUROPE/EQEC)*, Munich, Germany (2011).

[C15] S. Döring, S. Richter, A. Tünnermann and S. Nolte, "Influence of pulse duration on the hole formation during short and ultrashort pulse laser deep drilling," A. Heisterkamp, M. Meunier and S. Nolte (Eds.), *Frontiers in Ultrafast Optics: Biomedical, Scientific, and Industrial Applications XII*, vol. 8247 of *Proc. of SPIE*, 824717, San Francisco, CA, USA (2012).

[C16] S. Döring, T. Ullsperger, S. Richter, A. Tünnermann and S. Nolte, "Analysis of the hole formation in ultrashort pulse laser deep drilling," *DokDok*, Oppurg, Germany (2012).

[C17] S. Nolte, S. Döring and A. Tünnermann, "In-situ Characterization of Ultrashort Pulse Laser Deep Drilling," *SLT '12 - Stuttgart Laser Technology Forum*, Stuttgart, Germany (2012).

[C18] S. Richter, S. Döring, F. Zimmermann, L. Lescieux, R. Eberhardt, S. Nolte and A. Tünnermann, "Welding of transparent materials with ultrashort laser pulses," F. G. Bachmann, W. Pfleging, K. Washio, J. Amako, W. Hoving and Y. Lu (Eds.), *Laser-based Micro- and Nanopackaging and Assembly VI*, vol. 8244 of *Proc. of SPIE*, 824402, San Francisco, CA, USA (2012).

[C19] S. Richter, F. Jia, M. Heinrich, S. Döring, S. Nolte and A. Tünnermann, "Enhanced formation of nanogratings inside fused silica due to the generation of self-trapped excitons induced by femtosecond laser pulses," A. Heisterkamp, M. Meunier and S. Nolte (Eds.), *Frontiers in Ultrafast Optics: Biomedical, Scientific, and Industrial Applications XII*, vol. 8247 of *Proc. of SPIE*, 82470N, San Francisco, CA, USA (2012).

[C20] S. Döring, S. Richter, T. Ullsperger, A. Tünnermann and S. Nolte, "Influence of ambient pressure on the hole formation process in ultrashort pulse laser deep drilling," A. Heisterkamp, P. R. Herman, M. Meunier and S. Nolte (Eds.), *Frontiers in Ultrafast Optics: Biomedical, Scientific, and Industrial Applications XIII*, vol. 8611 of *Proc. of SPIE*, 86111D, San Francisco, CA, USA (2013).

[C21] S. Döring, T. Ullsperger, F. Heisler, S. Richter, A. Tünnermann and S. Nolte, "Hole Formation Process in Ultrashort Pulse Laser Percussion Drilling," *Lasers in Manufacturing (LiM 2013)*, Munich, Germany (2013).

[C22] S. Döring, T. Ullsperger, S. Richter, A. Tünnermann and S. Nolte, "Analysis of the hole formation in ultrashort pulse laser deep drilling," *DPG-Frühjahrstagung*, Jena, Germany (2013).

[C23] S. Richter, F. Burmeister, F. Zimmermann, S. Döring, A. Tünnermann and S. Nolte, "Formation of disruptions in molten fused silica induced by heat accumulation of ultrashort laser pulses at high repetition rates," *Conference on Lasers and Electro-Optics and International Quantum Electronics Conference 2013 (CLEO EUROPE/IQEC)*, Munich, Germany (2013).

[C24] S. Richter, F. Zimmermann, S. Döring, A. Tünnermann and S. Nolte, "Ultrashort high repetition rate exposure of dielectric materials: laser bonding of glass," *DPG-Frühjahrstagung*, Jena, Germany (2013).

[C25] S. Richter, F. Zimmermann, S. Döring, A. Tünnermann and S. Nolte, "Ultrastable bonding of glass with femtosecond laser bursts," A. Heisterkamp, P. R. Herman, M. Meunier and S. Nolte (Eds.), *Frontiers in Ultrafast Optics: Biomedical, Scientific, and Industrial Applications XIII*, vol. 8611 of *Proc. of SPIE*, 86111C, San Francisco, CA, USA (2013).

[C26] F. Zimmermann, S. Richter, A. Plech, S. Döring, M. Heinrich, M. Steinert, U. Peschel, E.-B. Kley, A. Tünnermann and S. Nolte, "The underlying structure of ultrashort pulse laser-induced nanogratings," A. Heisterkamp, P. R. Herman, M. Meunier and S. Nolte (Eds.), *Frontiers in Ultrafast Optics: Biomedical, Scientific, and Industrial Applications XIII*, vol. 8611 of *Proc. of SPIE*, 86110Y, San Francisco, CA, USA (2013).

[C27] F. Zimmermann, S. Richter, C. Vetter, S. Döring and A. Tünnermann, "Ultrashort pulse-induced nanogratings: temperature stable optically active phase elements," *Conference on Lasers and Electro-Optics and International Quantum Electronics Conference 2013 (CLEO EUROPE/IQEC)*, Munich, Germany (2013).

[C28] S. Döring, S. Richter, S. Nolte and A. Tünnermann, "Lokales Fügen transparenter Werkstoffe mit ultrakurzen Laserpulsen," *2. Innovationsforum MikroLas*, Rostock, Germany (2014).

[C29] S. Hauber, S. Döring, D. Harries, S. Nolte and F. Langenhorst, "Laser shock experiments on olivine," *92nd Annual Meeting Deutsche Mineralogische Gesellschaft*, Jena, Germany (2014).

Acknowledgments

This work would not have been possible without the generous support by a number of people. I want to take the opportunity to express my sincere gratitude to all of them.

First and foremost I would like to thank my supervisor *Prof. Dr. Stefan Nolte*, head of the Ultrafast Optics group at the Institute of Applied Physics. He introduced me to the field of ultrashort pulse laser micromachining and I really appreciated his gentle guidance and professional advice throughout the realization of this work. I want to thank *Prof. Dr. Andreas Tünnermann*, head of the Institute of Applied Physics and the Fraunhofer Institute for Applied Optics and Precision Engineering, for his motivation and encouragement.

Special thanks go to *Dr. Antonio Ancona* from CNR-IFN, U.O.S. Bari, for the close collaboration in the investigation of ultrashort pulse laser drilling at high repetition rates. He generously shared his scientific knowledge with me, in particular his practical experience. *Dr. Sören Richter* and I share a professional partnership with great benefit for both of us as well as a personal friendship. I am very thankful for the time we spent together, especially the profound discussions on our scientific work, which offered many new ideas and sometimes enabled a completely different view on the subject. My dear friend and former colleague *Dr. Matthias Heinrich* is a master of writing scientific papers and presenting his work. I am deeply grateful to have learned and benefited from his knowledge and experience.

Mr. Tobias Ullsperger realized the experiments to capture the plasma luminescence of the laser ablation process during his diploma thesis. His excellent work deserves my sincere thanks. I also owe thanks to my colleague *Mr. Felix Zimmermann* for showing me the basics of computational physics and supporting my early attempts of numerical simulation. I am deeply grateful for the valuable advice of *Prof. Dr. Herbert Gross* on the specifics of BPM simulation.

Zusammenfassung

Ultrakurze Laserpulse mit einer Pulsdauer im Piko- und Subpikosekundenbereich, besitzen großes Potential zur Erzeugung präziser und qualitativ hochwertiger Mikrostrukturen [6–9, 15, 17]. Die Wechselwirkungsprozesse beim Lasermaterialabtrag sind aufgrund umfangreicher experimenteller und theoretischer Untersuchungen bereits weitgehend verstanden [1–3, 15, 17]. Die Erzeugung von Strukturen mit hohem Aspektverhältnis ($\geq 5 : 1$) bei Strukturbreiten im Bereich weniger Mikrometer (typischerweise $< 100\,\mu m$) ist jedoch eine große Herausforderung. Dies betrifft insbesondere Mikrobohrungen. Der Abtragsvorgang am Bohrungsgrund wird hierbei von der bereits vorhandenen Bohrungskapillare beeinflusst. Dies führt zu einer Verringerung der Abtragsrate mit zunehmender Tiefe [19–22]. Darüber hinaus verändert sich auch die Form der Bohrung, beispielsweise durch Ausbeulungen und Vertiefungen an den Lochwänden [24, 87]. Zudem können Bohrungen bei großer Tiefe abknicken und Verästelungen aufweisen [21, 25]. Die Vorteile des Oberflächenabtrags mit ultrakurzen Pulsen sind somit nicht direkt auf tiefe Bohrungen übertragbar. Für ein grundlegendes Verständnis des Bohrprozesses sind tiefergehende Untersuchungen erforderlich.

Eine systematische Untersuchung des Bohrvorgangs und der beteiligten Prozesse in opaken Materialien, insbesondere Metallen, ist jedoch anspruchsvoll. Die üblicherweise nach dem Bohren erstellten Schnitte zeigen den Zustand der Bohrung nur für einen bestimmten Zeitpunkt [25, 40, 87, 90–92]. Da die Ausbildung der Bohrungsform jedoch starken statistischen Schwankungen unterliegt, erlauben diese Untersuchungen keine detaillierte Nachverfolgung der individuellen Bohrlochentwicklung. Eine direkte Beobachtung des Bohrvorgangs wurde bisher in transparenten Materialien, beispielsweise speziellen Keramiken, Diamant, Glas oder Kunststoffen, realisiert [19, 21, 23, 24, 28, 29, 31]. Die Materialeigenschaften als auch der Abtragsprozess unterscheiden sich allerdings stark von opaken Materialien wie Metallen.

Zur Erklärung der Veränderungenen in der Bohrformentwicklung mit zunehmender Tiefe existieren bisher mehrere, unterschiedliche Modelle. Diese umfassen Material-inhomogenitäten [21], Abtrag durch das Plasma [19, 24], nichtlineare Wechselwirkung mit der Atmosphäre [34–36] und den Einfluss des Bohrloches als auch des Plasmas auf die Pulspropagation [22, 25, 27, 37, 39, 40]. Der spezifische Anteil dieser möglichen Ursachen an der Lochentwicklung ist jedoch nicht vollständig untersucht.

Daher ist ein neuer Ansatz für eine detaillierte Analyse des Bohrprozesses notwendig. In dieser Arbeit wird erstmals eine in-situ Beobachtung des Bohrvorgangs in einem opaken Material realisiert. Das Prinzip beruht darauf, kristallines Silizium als Probenma-terial zu verwenden. Dieses Material ist transparent im Wellenlängenbereich oberhalb der Bandkante von ca. 1100 nm [41] und absorbiert Laserwellenlängen unterhalb der Bandkante, d.h. insbesondere die typische Ultrakurzpulslaserstrahlung zur Material-bearbeitung bei 1030 nm, 800 nm und 515 nm. Das Abtragsverhalten mit ultrakurzen Laserpulsen ist zudem vergleichbar mit Metallen [15, 42, 43] und die gewonnenen Er-kenntnisse sind damit sowohl auf Halbleiter als auch Metalle anwendbar. Während des Bohrvorgangs wird die Probe von einem zweiten Laser durchleuchtet und die Silhouette der Bohrung direkt abgebildet. Bei dem hier untersuchten Perkussionsbohren wird die Position des Laserfokus während des gesamten Bohrvorgangs ortsfest gehalten, typischerweise auf der Probenoberfläche. Der Druchmesser der Bohrung wird daher direkt von der Größe des Laserfokus bestimmt und es ist ein besonders starker Einfluss auf die Bohrungsentwicklung zu erwarten.

Abgesehen von parameterspezifischen Effekten und Abhängigkeiten gliedert sich der Bohrprozess in drei charakteristische Phasen.

1. Zu Beginn des Prozesses bildet sich während weniger hundert Pulse mit hoher Abtragsrate die Bohrungskapillare aus.

2. In der zweiten Prozessphase sinkt die Abtragsrate stark ab. Zudem zeigen sich starke Fluktuationen in der Tiefenentwicklung, die mit der Bildung von Ausbeu-lungen und Verzweigungen verknüpft sind. Außerdem kann die Vortriebsrichtung gegenüber dem einfallenden Strahl abknicken. Es können sogar längere Perioden ohne Bohrungsvortrieb beobachtet werden. Währenddessen erfolgt weiterhin ein Abtrag, der die Lochgeometrie umformt. Daraufhin kann es auch zu einem weiteren Bohrvortrieb kommen. Die konkrete Entwicklung ist allerdings für jedes Bohrloch unterschiedlich und unterliegt starken statistischen Schwankungen.

3. In der finalen dritten Phase findet kein weiteres Tiefenwachstum statt. Es kann aber immer noch zu einer Aufweitung der Bohrung und zur Bildung weiterer Verzweigungen kommen.

Die Form und Tiefe der Bohrung hat ebenfalls einen direkten Einfluss auf die Ausdehnung des beim Laserabtrag generierten Plasma. Durch die Beobachtung der Plasmaentwicklung oberhalb der Bohrungsöffnung ließe sich daher eine Prozessüberwachung für opake Materialien realisieren.

Es konnte gezeigt werden, dass die Pulsenergie ein wesentlicher Prozessparameter ist, welcher die erreichbare Tiefe der Bohrung nahezu unabhängig von der tatsächlichen Fokussierung und aufgebrachten Fluenz bestimmt.

Bei hohen Pulswiederholraten im Bereich mehrerer hundert kHz kommt es zu einem länger andauernden Bohrprozess, verbunden mit einer größeren Lochtiefe und einer Aufweitung der Bohrungskapillare, im Vergleich zu niedrigeren Pulswiederholraten, z. B. wenige hundert Hz. Dies ist im Wesentlichen auf Wärmeakkumulation bei kurzen Pulsfolgeabständen zurückzuführen und geht daher mit beträchtlicher Schmelzbildung und somit reduzierter Bohrungsqualität einher.

Es konnte weiterhin gezeigt werden, dass Ablagerungen von Ablationsprodukten einen wesentlichen Einfluss auf die Dauer des Bohrvorgangs und die erreichbare Tiefe haben, da sie die Bohrungskapillare zusetzen und die Lichtausbreitung zum Bohrungsgrund stark einschränken können. Bei reduziertem Umgebungsdruck lassen sich solche Ablagerungen deutlich verringern und treten erst bei größerer Tiefe auf.

Als entscheidender Einflussfaktor auf die Bohrlochentwicklung wurde die Lichtausbreitung innerhalb des Bohrlochs identifiziert. Eine von der einfallenden Intensitätsverteilung und Strahlrichtung abweichende Bohrungsgeometrie wird von einer Ablenkung des Laserstrahls an Unebenheiten der Lochwand hervorgerufen. Anhand des Einflusses der Bohrungsgeometrie auf die Pulspropagation lassen sich selbstverstärkende Effekte wie das Abknicken der Bohrung, bei dem sich die Abweichung von der Strahlrichtung zunehmend erhöht, erklären. Eine optimale Fokusposition unterhalb der Probenoberfläche kann die erreichbare Tiefe der Bohrung maßgeblich beeinflussen. Dies kann in Übereinstimmung mit der Deutung der Lichtausbreitung im Bohrloch erklärt werden. Darüber hinaus konnte gezeigt werden, dass die Umformung der Bohrungsgeometrie während einer Periode konstanter Tiefe wesentlich ist für die Veränderung der Lichtausbreitung nach einem Bohrstopp und damit für die Fortführung des Bohrvorgangs.

Damit konnte im Rahmen dieser Arbeit erstmal eine vollständige Beobachtung und Analyse des Bohrvorgangs beim Ultrakurzpulslaserbohren in einem opaken Material realisiert werden. Somit ist es gelungen die wesentlichen Prozesse und Einflussgrößen der Bohrlochentwicklung zu identifizieren und eine Modellvorstellung des Bohrprozesses für tiefe Bohrungen zu entwickeln.

Im Ergebnis ist für eine Verbesserung der Präzision und Qualität einer Mikrobohrung eine Verringerung der Beeinflussung der Strahlpropagation innerhalb der Bohrungskapillare wesentlich. Hierfür können innovative Bohrverfahren genutzt werden, bei denen der Laserfokus während des Bohrvorgangs bewegt wird, beispielsweise Trepanieren oder Wendelbohren [38, 44]. Mit einer Verkippung des Strahl gegenüber der Lochachse können hierbei senkrechte oder sogar überhängende Lochwände erzeugt und somit der Einfluss der Lochwandung weiter reduziert werden. Allerdings ist bei diesen Verfahren der Bohrungsdurchmesser größer als der Laserfokus und die Realisierung kleiner Bohrungen (Durchmesser $< 50\,\mu m$) sehr anspruchsvoll. Alternativ ist eine dynamische Anpassung der Prozessparameter wie der Pulsenergie an den Bohrvorgang und die Lochtiefe möglich, um entstandene Asymmetrien abzutragen oder auszugleichen. Weiterhin könnten die Bedingungen für den Abtrag und die Strahlpropagation kontinuierlich oder zufällig moduliert werden, um eine einseitige Akkumulation der Bohrungsdeformation über mehrere Pulse zu vermeiden, beispielsweise durch eine ständige, schnelle Lageänderung des Fokus oder eine zeitliche Modulation der Pulswiederholrate. Daneben könnte auch eine gezielte, adaptive Strahlformung verbunden mit einer direkten Prozessüberwachung mögliche Ablenkungen in der Pulsausbreitung kompensieren.

Weitergehende Untersuchungen zur Verbesserung der Präzision und Qualität für tiefe Strukturen sollten unter anderem die Entstehung von Asymmetrien während der Ablation umfassen, die dann zu Aufwürfen und Unebenheiten an den Wänden führen. Zudem ist eine tiefergehende Untersuchung der Auswirkungen dieser Strukturen auf die Strahlpropagation sinnvoll. Dazu kann das Verfahren zur in-situ Beobachtung zu einer vollständigen dreidimensionalen Visualisierung der Lochform, beipielsweise per Tomographie, erweitert werden. Eine Alternative bietet das zur Auflösung von Mikrostrukturen weiterentwickelte Verfahren der Röntgentomographie, mit dem auch das Innere der Bohrung abgebildet werden könnte [159].

Die Ergebnisse dieser Arbeit sind grundlegend für die Erzeugung hochqualitativer Mikrobohrungen in Silizium und metallischen Werkstoffen. Eine direkte Anwendung sind beispielsweise Durchgangsbohrungen in Siliziumwafern zur dreidimensionalen Vernetzung in der Mikroelektronik [160]. Mikrobohrungen spielen darüber hinaus vom Automobilbau, z. B. für Einspritzdüsen, bis hin zum Kunststoffspritzguss, z. B. für Entlüftungsöffnungen, eine Rolle [8, 162]. Die hier untersuchten Prozesse und Zusammenhänge sind weiterführend nicht nur für Bohrungen sondern für alle Mikrostrukturierungsprozesse mit großer Tiefe und hohem Aspektverhältnis relevant.

Erklärung

Ich erkläre hiermit ehrenwörtlich, dass ich die vorliegende Arbeit selbstständig und ohne unzulässige Hilfe Dritter sowie ohne Benutzung anderer als der angegebenen Hilfsmittel und Literatur angefertigt habe. Aus anderen Quellen direkt oder indirekt übernommene Daten und Konzepte sind unter Angabe der Quellen gekennzeichnet.

Bei der Auswahl und Auswertung folgenden Materials haben mir die nachstehend aufgeführten Personen in der jeweils beschriebenen Weise unentgeltlich geholfen:

1. Herr Tobias Ullsperger hat im Rahmen seiner Diplomarbeit „Räumlich und zeitlich hochaufgelöste Untersuchung des ultrakurzpuls-induzierten Plasmas bei der Tiefenablation von Silizium und ionengefärbtem Glas" die Datenaufnahme und Auswertung der Plasmalumineszenz vorgenommen, welche hier in Abschnitt 5.3 ab Seite 83 dargestellt sind.

2. Die Simulation der Lichtausbreitung im Bohrloch anhand der FDTD Methode in Anhang C ab Seite 109 wurde von Herrn Matthias Zilk zur Verfügung gestellt.

Weitere Personen waren an der inhaltlich-materiellen Erstellung der vorliegenden Arbeit nicht beteiligt. Insbesondere habe ich hierfür nicht die entgeltliche Hilfe von Vermittlungs- bzw. Beratungsdiensten („Promotionsberatern" oder anderen Personen) in Anspruch genommen. Niemand hat von mir unmittelbar oder mittelbar geldwerte Leistungen für Arbeiten erhalten, die im Zusammenhang mit dem Inhalt der vorgelegten Dissertation stehen.

Die Arbeit wurde bisher weder im In- noch im Ausland in gleicher oder ähnlicher Form einer anderen Prüfungsbehörde vorgelegt.

Teile dieser Arbeit wurden aus Prioritätsgründen bereits veröffentlicht bzw. zur Veröffentlichung eingereicht.

Die geltende Promotionsordnung der Physikalisch-Astronomischen Fakultät ist mir bekannt.

Ich versichere ehrenwörtlich, dass ich nach bestem Wissen die reine Wahrheit gesagt und nichts verschwiegen habe.

Jena, 15. April 2014   Sven Döring